Physical, electrical and electrochemical characterizations of transition metal compounds for electrochemical energy storage

Qifan Yuan

Dissertation submitted to the Faculty of the Virginia Polytechnic Institute and State University in partial fulfillment of the requirements for the degree of

Doctor of Philosophy

in

Physics

Victoria Soghomonian, Chair

Jean J. Heremans

Camillo Mariani

Kyungwha Park

January 20, 2015

Blacksburg, VA

Keywords: Energy storage, transition metal compound, nanostructured material, electrochemistry, x-ray crystallography, electrical conductivity, impedance spectroscopy

Physical, electrical and electrochemical characterizations of transition metal compounds for electrochemical energy storage

Qifan Yuan

(ABSTRACT)

Electrochemical energy storage has been widely used in various areas, including new energy sources, auto industry, and information technology. However, the performance of current electrochemical energy storage devices does not meet the requirements of these areas that include both high energy and power density, fast recharge time, and long lifetime. One solution to meet consumer demands is to discover new materials that can substantially enhance the performance of electrochemical energy storage devices. In this dissertation we report four transition metal materials systems with potential applications in electrochemical energy storage.

Nanoscale and nanostructured materials are expected to play important roles in energy storage devices because of their enhanced and sometimes unique physical and chemical properties. Studied here is the comparative electrochemical cation insertion into a nanostructured vanadium oxide, a promising electrode material candidate, for the alkali metal ions Li^+, Na^+ and K^+ and the organic ammonium ion, in aqueous electrolyte solutions. Observed are the distinctive insertion processes of the different ions, which yield a correlation between physical degradation of the material and a reduction of the calculated specific charge. The results reveal the potential of this nanostructured vanadium oxide material for energy storage. Vanadium based electrochemical systems are of general interest, and as models for vanadium based solid-state electrochemical processes, the solution state and the solid-state electrochemical properties of two cryolite-type compounds, $(NH_4)_3V_xGa_{1-x}F_6$, and Na_3VF_6, are studied. The electrochemical behavior of $(NH_4)_3V_xGa_{1-x}F_6$ explored the possibility of using this material as an electrolyte for solid state energy storage systems.

Zeolite-like materials have large surface to volume ratios, with ions and neutral species located in the nanometer sized pores of the 3-dimensional framework, potentially yielding high energy density storage capabilities. Yet the insulating nature of known zeolite-like materials has limited

their use for electrical energy storage. Studied here are two vanadium based zeolite-like structures, the oxo-vanadium arsenate $[(As_6V_{15}O_{51})^{-9}]_\infty$, and the oxo-vanadium phosphate $[(P_6V_{15}O_{51})^{-9}]_\infty$, where the former shows electronic conduction in the 3-dimensional framework. Mixed electronic and ionic conductivity, from the framework and from the cations located within the framework, respectively, is measured in the oxo-vanadium arsenate, and allows the use of this material in electrochemical double-layer capacitor configuration for energy storage. By contrast, the oxo-vanadium phosphate shows ionic conduction only. Lastly, a new strontium manganese vanadate with a layered structure exhibiting mixed protonic and electronic conductivity is studied. The various transition metal compounds and materials systems experimentally studied in this thesis showcase the importance of novel materials in future energy storage schemes.

Dedication

To my parents, Rugui Yuan and Cuiping Zhou,

I cannot succeed without your guidance, love, patience, and support.

To my wife, Wei Li, and my son, Leonardo Muxiu Yuan,

thank you for your support and motivating me to never give up.

Acknowledgement

Throughout my seven years at Virginia Tech, I have met some incredible people, and I am thankful for the role each one has played in my success. I am also grateful for the opportunity to express my thanks in this acknowledgement. Without the help and support of these people, I could not have completed my PhD degree.

First, I would like to thank my adviser, Dr. Victoria Soghomonian. I was fortunate to be your student, and I value the level of intensity you have devoted to my success. I have taken the wisdom you have given me to heart and I believe I will carry it with me even after I leave campus. You have taught me not only science, but also how to pursue success in every area.

I also would like to thank my committee members, Dr. Jean Joseph Heremans, Dr. Jonathan Link, Dr. Camillo Mariani, and Dr. Kyungwha Park, for the thoughtful and comprehensive feedback and guidance. Your feedback provided meaning and relevance to my research. Dr. Jean Joseph Heremans, I especially thank you for helping me navigate through the physics research, carefully keeping me on my path and clarifying what needed to be done. You encouraged me throughout the process, and I greatly appreciate all the help and time we spent together.

I am thankful for Dr. Carla Slebodnick of the chemistry department. Thank you for the patience and countless pieces of advice and encouragement as I executed the x-ray crystallography study.

I also thank my lab colleagues, Dr. Raymond Kallaher, Dr. Robert Lillianfeld, Dr. Yao Zhang, Dr. Yong-Jae Kim, Dr. Martin Rudolph, Lingling Xu, Shaola Ren, and Yuntao Xie. I have truly enjoyed working with each of you. I thank you for your friendship and support.

Lastly, I would like to thank the followings for financial support throughout my doctoral studies:

the graduate school for the 2010 Ph.D. fellowship, and the National Science Foundation through the grants DMR 0943971 and DMR 1206338**.** Without these supports, I would not have been financially independent while pursing my Ph.D. research.

Contents

List of Figures

List of Tables

Chapter 1 Introduction

World energy consumption today mainly depends on fossil fuels that provide the energy for transportation, electricity, industry and many other areas. However, the combustion of fossil fuels is a major source of CO_2 emissions, influencing the global climate [1]. At the same time, the diminishing reserve of fossil fuels has brought increasing demand for new, cheap, efficient, clean, and renewable energy sources, such as solar, wind, and nuclear energy [2-4]. A common feature of all these new energy sources is that they are utilized to generate electricity, which is stored using electrical energy storage devices. Therefore, the efficiency of the storage devices of electrical energy is a key factor that controls the efficiency, competitiveness, and marketability of the new energy sources [3, 5]. The performance of current electrical energy storage systems, however, does not meet consumer demands. For example, the energy storage devices still have difficulty to efficiently handle solar and wind energies, which produce electricity in an intermittent and unsteady fashion [6].

Efficient energy storage devices are not only important for new energy sources; they are crucial for the auto industry, information technology, and almost every aspect of human activities. For example, the development of hybrid electric vehicles, plug-in hybrid electric vehicles and all-electric vehicles requires the replacement of the internal combustion engine with more efficient electrical energy storage devices such as batteries. However, the current power density, size, weight, and cost of batteries are still far from optimum, which limits the market share of these vehicles. Gordon E. Moore stated in 1965 that the number of transistors on a computer chip would increase exponentially in time, the so called Moore's law [7] which still drives the semiconductor industry. It has been successfully used to predict the improvement of computer performance over

the past several decades, and is regarded as a reliable method to forecast future development. However, the development of electrical energy storage systems is at a pace slower than the pace enjoyed by electrical devices as suggested by Moore's law, and is currently the main bottleneck that hinders progress in industries that rely and use an electrical energy storage component. In order for energy storage progress to maintain pace with the rest of the electronics world, grand transformations in electrical energy storage systems are much desired.

Electrochemical energy storage is a major approach for storing electrical energy. The two fundamental electrochemical energy storage devices are batteries and electrochemical capacitors [8], both of which are based on electrochemistry principles. The energy storage in batteries is in the form of the capability to generate charges by chemical reactants. Upon energy release, the chemical energy stored in batteries is converted into electrical energy. Batteries always have higher energy density than electrochemical capacitors but smaller power density, shorter lifetime and longer charging time. Electrochemical capacitors, also called supercapacitors or ultracapacitors, provide faster power delivery and longer lifetime than batteries, but currently do not have the same energy density as batteries [9]. Electrochemical capacitors store energy directly in the form of charges. They employ porous materials as energy storage media to achieve a high surface area. The energy density of supercapacitors is much higher than that of conventional capacitors because of the enormous surface area the porous materials provide, and the small charge separation (in the order of angstroms) at the interface between electrodes and electrolytes. The first supercapacitor was developed in 1957 based on a double-layer mechanism [10]. The supercapacitors fabricated with the double-layer mechanism use mesoporous carbon as electrodes and are called electric double-layer capacitors (EDLCs). They have high capacitance because the length scale of the charge separation in a double-layer is intrinsically at the molecular scale. The

energy in EDLCs is electrostatically stored in the form of charges. Another type of supercapacitor is the pseudocapacitor, which is developed with conducting polymers and transition metal oxides as electrode materials [11, 12]. It has high electrochemical pseudocapacitance, which is the capacitance with the charges electrochemically stored at the interface between the electrode and electrolyte with fast and reversible electrochemical reactions.

Ragone plots are typically used to compare and evaluate the energy delivery performance of various energy storage systems by plotting specific power as a function of specific energy [13, 14]. Specific energy represents how much total energy can be stored, while specific power refers to how fast energy can be delivered. The diagonal axis of a Ragone plot represents time scales that are the time constants obtained as the specific energy divided by the specific power. The time scale provides the time needed for completing the discharge of stored energy of a device performing at its maximum rate. The Ragone plot in Ref. [14] shows the specific power and energy properties of the most important electrochemical energy storage systems. In this and other Ragone plots, batteries have large specific energy, while conventional capacitors have large specific power. Electrochemical capacitors have larger specific power than batteries and larger specific energy than conventional capacitors. However, all three still cannot meet the energy and power density requirements of efficient electrical energy storage. Currently extensive efforts are being devoted to the development of innovative electrical energy storage systems.

The performance of electrochemical energy storage systems is mainly constrained by the materials used. Therefore, there is a great need of novel materials for electrochemical energy storage devices. Transition metal compounds have gained much attention as electrochemical energy storage materials due to their interesting structural, electrical and electrochemical properties. They provide multiple oxidation states for electron transfer reactions, e.g. redox reactions, and are broadly used

as electrode materials for both batteries and electrochemical capacitors. For example, transition metal compounds can be used as cathode materials for Li-ion and Li batteries [15, 16]. Li batteries use Li metal as the anode material and transition metal compounds as the intercalation material at the cathode. The intercalation occurs via the following reaction:

$$Li + MX_n \rightarrow LiMX_n \quad (1.1)$$

where M is a transition metal such as Ni, Mn, Co, V, Ti, etc. or their mixtures, and X could be O, S, or other cations like SO_4^{2-} or PO_4^{3-} [15]. In Li-ion batteries, both the cathode and anode are made of intercalation compounds, with alloys or transition metal compounds as the anode and transition metal oxides as the cathode. Li-ion batteries operate by transporting Li^+ ions between two electrodes. The Li-ion insertion process in the cathode materials occurs via the following reaction:

$$Li^+ + e^- + MO_n \rightleftharpoons LiMO_n \quad (1.2)$$

where MO_n is a transition metal oxide like MnO_2, CoO_2 and NiO_2 [17, 18]. Here, we assume that only one Li ion is inserted every transition metal site, and only the transition metal undergoes the oxidation-reduction step as shown in the reaction above. Besides transition metal oxides, other transition metal compounds, including $LiFePO_4$ and Li_2MnSiO_4, are also employed as cathode materials in Li-ion batteries [16]. Transition metal oxides such as RuO_2, MnO_2, Co_3O_4, Fe_3O_4 and NiO are excellent pseudo-capacitive active materials [19-22]. Pseudocapacitors with electrodes based on these transition metal oxides can produce higher capacitances than EDLCs based on porous carbon electrodes [14, 22, 23]. Although transition metal compounds have already been adopted as electrochemical energy storage materials, they still have limitations including high cost,

low specific surface area, low electrical conductivity and low temperature and chemical satiability. More research is thus needed to discover new transition metal compounds and to understand their electrochemical properties. In this thesis, we report the physical, electrical and electrochemical characterizations of four transition metal materials in light of their potential applications in the field of electrical energy storage. All characterization methods are discussed in Chapter 2.

In Chapters 3 and 6, we report a nanostructured vanadium oxide material and a cryolite-type compound, $(NH_4)_3V_xGa_{1-x}F_6$, focusing on their electrochemical properties. Electrochemistry studies the electrochemical reactions that occur at the interface of two phases. Electrochemical reactions bring about the transfer between electrical energy and chemical energy and play an important role in energy storage. Historically, electrochemistry has been involved in energy storage -from the Baghdad battery over two millennia ago [5] to the Li-ion batteries and electrochemical capacitors currently used. As shown in Fig. 1.1, the Baghdad battery has all the necessary components of an electrochemical cell, including two electronic conductors (a copper cylinder and an iron rod) as electrodes in contact with an ionic conductor as the electrolyte. Although the performance of electrochemical energy storage systems has been improved over years by the development of new batteries and electrochemical capacitors, our knowledge of the complex electrochemical processes occurring in these systems is still limited. A deep understanding of these electrochemical processes is significantly important not only for enhancing the efficiency of existing batteries and supercapacitors but also for developing new concepts for novel electrochemical energy storage systems. In Chapter 3, we investigate the electrochemical behavior of a nanostructured vanadium oxide material as electrodes in chloride solutions containing different cations. In Chapter 6, we study the solid state electrochemical processes of $(NH_4)_3V_xGa_{1-x}F_6$, as well as in $(NH_4)_3V_xGa_{1-x}F_6$ aqueous solutions functioning as electrolytes.

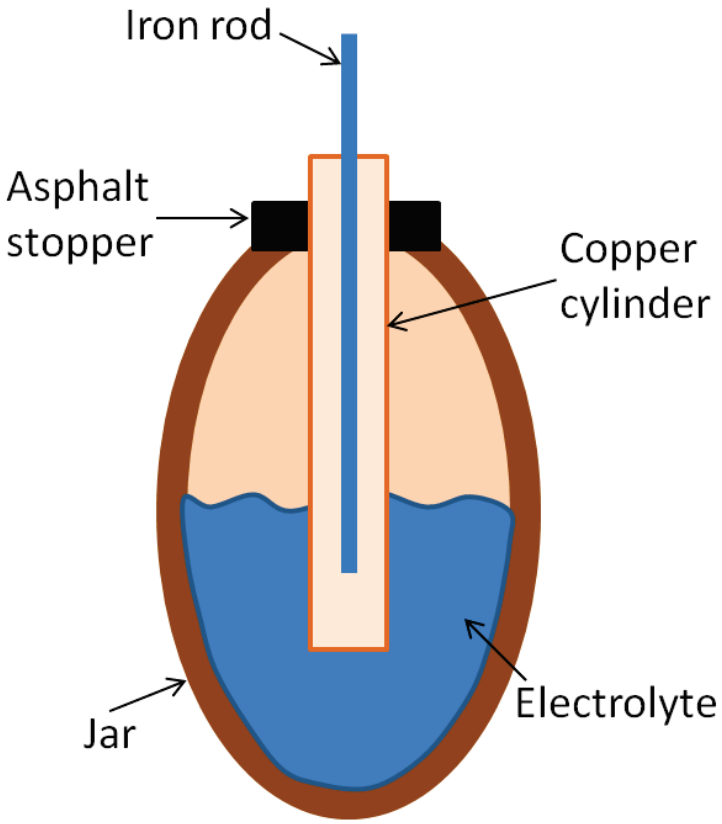

Figure 1.1: Sketch of the Baghdad battery, the first known electrochemical cell in the world used for electroplating over two millennia ago (modified from Ref. [5]).

A major challenge in the field of energy storage is to design a device with both high specific energy and high power density. One promising route to address this challenge is to utilize nanostructured materials. Recent developments have shown that nanostructuring of materials -either controlling a material's morphology at the nanoscale or controlling a material's structural at the nanoscale- have led to enhanced performance of electrochemical energy storage devices [24, 25]. The underlying physical principle is that compared to traditional materials, nanostructured materials have higher surface-to-volume ratios and shorter diffusion lengths [26]. As a consequence, more energy can be stored per unit volume, and energy can be released more rapidly due to enhanced rate of

electrochemical reactions, yielding both high energy and power density. However, a big challenge with nanostructured materials is their stability issue over rapid charge-discharge cycles. In fact, the stability of any electrode materials is a general concern in the field of energy storage. To address these issues, we study a nanostructured material composing vanadium oxide nanosheets in Chapter 3. We discuss both the electrochemical insertion process and the cyclic stability of this nanomaterial.

In Chapters 4 and 5, we report two zeolite-like materials (an oxo-vanadium arsenate $[(As_6V_{15}O_{51})^{-9}]_\infty$, and an oxo-vanadium phosphate $[(P_6V_{15}O_{51})^{-9}]_\infty$), and a strontium manganese vanadate framework, $SrMn_2(VO_4)_2(\mu_3\text{-}OH)(\mu_4\text{-}OH_2)$, respectively. All are transition metal oxide frameworks and are mixed electronic-ionic conductors. We investigate their electrical properties as a function of temperature. As discussed before, the EDLCs are supercapacitors based on the electric double-layers that are formed at the interface between the electrodes and electrolytes, with electrons in the electrode and mobile ions in the electrolyte. The capacitance of the EDLCs can be calculated by the equation:

$$C = \frac{\varepsilon_r \varepsilon_0 A}{d} \tag{1.3}$$

where C is the capacitance, A is the effective surface area, ε_r is the relative static permittivity (dielectric constant), ε_0 is the permittivity of free space, and d is the charge separation distance. The EDLCs attained large capacitance because of the short charge separation distance (on the order of angstroms) and the large effective surface area from the porous electrode material. Zeolite-like materials thus have the great potential to be used as electrodes for EDLC because of their porous structure formed by the crystal framework [27]. A schematic concept of an EDLC

using zeolite-like materials as electrodes is shown in Ref. [27]. The two electrodes are connected to an external voltage source with a potential difference V. An ion membrane separates the cell into two half-cells, with one electrode in each. The membrane is permeable to the electrolyte ions. The two electrodes are oppositely charged, and thus attract oppositely charged ions from the electrolyte solutions into the pores of the zeolite-like electrodes. The energy stored in an EDLC is expressed by the following equation:

$$U = \frac{1}{2} CV^2 \tag{1.4}$$

where U is the stored energy. With a high capacitance C per material volume obtained with the double-layer mechanism, a large specific energy is achieved. However, the application of porous structures based on zeolite-like materials to EDLCs is limited by the limited electronic conduction of these materials. In Chapter 4, we study the electronic and ionic conductivities of the oxo-vanadium arsenate and phosphate. Since manganese oxides are widely used because of their interesting structural and electrical properties [28-30], we study the protonic and electronic conductivities, as a function of temperature, in a new layered structure of the strontium manganese vanadate in Chapter 5.

In short, while we here present several new materials systems and concepts for electrical energy storage applications, the field is still wide open for new and transformative discoveries for this outstanding scientific, economic and societal topic.

Chapter 2 Materials and characterization

2.1 Materials

The materials under investigation in this work are synthesized hydrothermally. Hydrothermal synthesis is a closed-system physical and chemical process used in the preparation of various new materials, including porous materials [31-33], ionic conductors [34, 35], and complex oxides and fluorides [36, 37]. It is popular because of its high reactant reactivity, easy reaction control, low pollution and low energy consumption. Hydrothermal synthesis is defined as "any heterogeneous chemical reaction in the presence of a solvent (whether aqueous or nonaqueous) above room temperature and at pressure greater than 1 atm in a closed system" [38]. In this thesis, we report the physical and electrical properties of some hydrothermally synthesized nanostructured material (nanostructured vanadium oxide, in Chapter 3) and crystalline materials (oxo-vanadium arsenate and phosphate frameworks, strontium manganese vanadate and arsenate frameworks, and cryolite-type $(NH_4)_3V_xGa_{1-x}F_6$ and Na_3VF_6 crystals, in Chapters 4, 5 and 6, respectively).

2.2 Physical characterization

2.2.1 X-ray crystallography

We perform single crystal x-ray diffraction (XRD) analysis to obtain the structural information of our crystalline samples. The XRD experiment is performed on an Oxford Diffraction Gemini A Ultra diffractometer equipped with a Sapphire 3 CCD detector and operating with MoKα radiation as shown in Fig. 2.1. The crystal samples we use are selected under microscope and cleaned. We choose single crystals that are regularly shaped and have no obvious dislocations, and discard twinned crystals or crystals with cracks and dislocations. The single crystals are then placed in

Paratone oil. This oil is a highly viscous organic compound that serves to bind the crystal to the loop shape sample holder. The sample holder and single crystal are then mounted on a goniometer. The XRD experiments are performed at 295 K or 100 K. The program CrysAlisPro [39] is adopted for data collection, unit cell refinement, and data processing, from which we obtain the unit cell, space group and electron density map. The crystal structures are then solved and refined using SHELXL-97 [40] via OLEX2 [41].

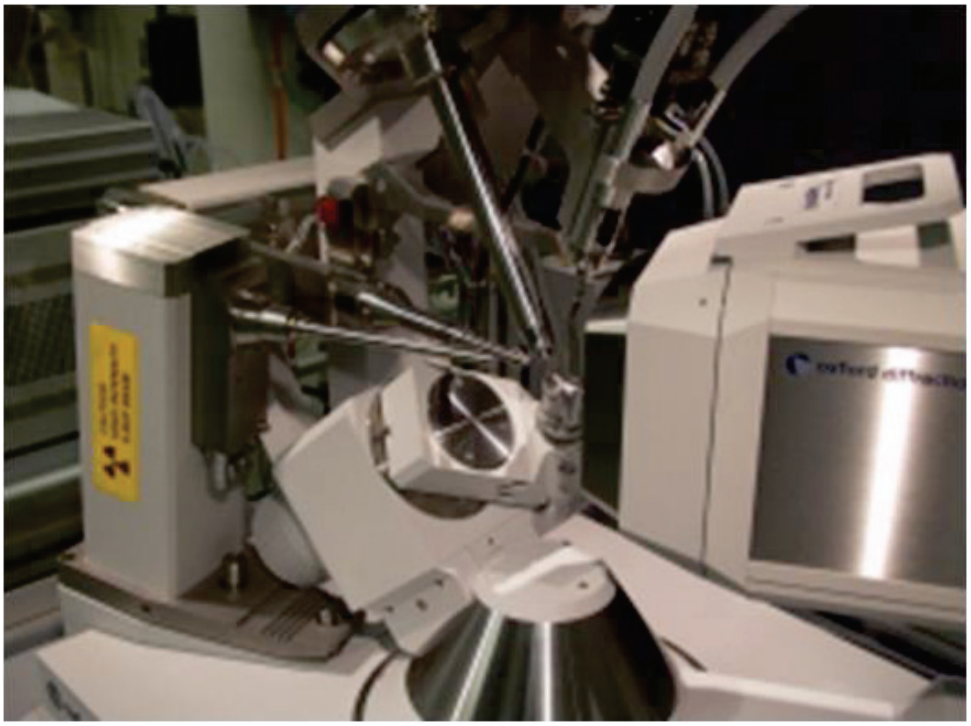

Figure 2.1: Picture of the Oxford Diffraction Gemini A Ultra diffractometer.

2.2.2 Thermogravimetric analysis

Thermogravimetric analysis (TGA) is used to analyze the thermal stability and composition of our samples. TGA is an analytical tool for monitoring the mass of a sample as a function of

temperature or time with a controlled temperature program under a controlled atmosphere [42]. We perform the TGA experiment with a Perkin Elmer TGA7 thermogravimetric analyzer in a nitrogen atmosphere. The thermogravimetric analyzer consists of a heating system that precisely controls and monitors temperature change and a sample pan supported by a precision balance. Crystals are picked out from the hydrothermal reaction product, cleaned and dried. They are then ground with a mortar and pestle to a uniform powder. Then the TGA experiment is performed at a certain temperature range and rate. The sample mass is monitored during the experiment. A TGA thermal curve is plotted with time or temperature as abscissa and weight or weight percent as ordinate. We analyze the compounds' changes during the TGA experiment by the percent of mass of starting material obtained in the final product.

2.2.3 UV-Vis adsorption edge spectrum

Ultraviolet-visible (UV-Vis) adsorption edge spectrum is used to determine the optical band gap. An Evolution 300 UV-Vis spectrophotometer (as shown in Fig. 2.2) is adopted to perform UV-Vis diffuse reflectance measurements on powder samples. It is equipped with a Praying Mantis diffuse reflectance accessory (DRA) specifically designed to measure diffuse reflectance. The powder samples are prepared following the same procedure as in the TGA experiment. The powder sample is placed in a stainless steel sample holder mounted horizontally into the chamber of the Praying Mantis DRA. Ultraviolet-visible light beams onto the powder sample. Diffusely reflected light is collected by the instrument detector through two hemispherical mirrors above the sample to give a diffuse reflectance spectrum. From the transition between the strong short-wavelength and the weak long-wavelength absorption in the spectrum, the absorption edge is obtained as the band gap energy, which is the energy separation between the valence and conduction bands of the material [43].

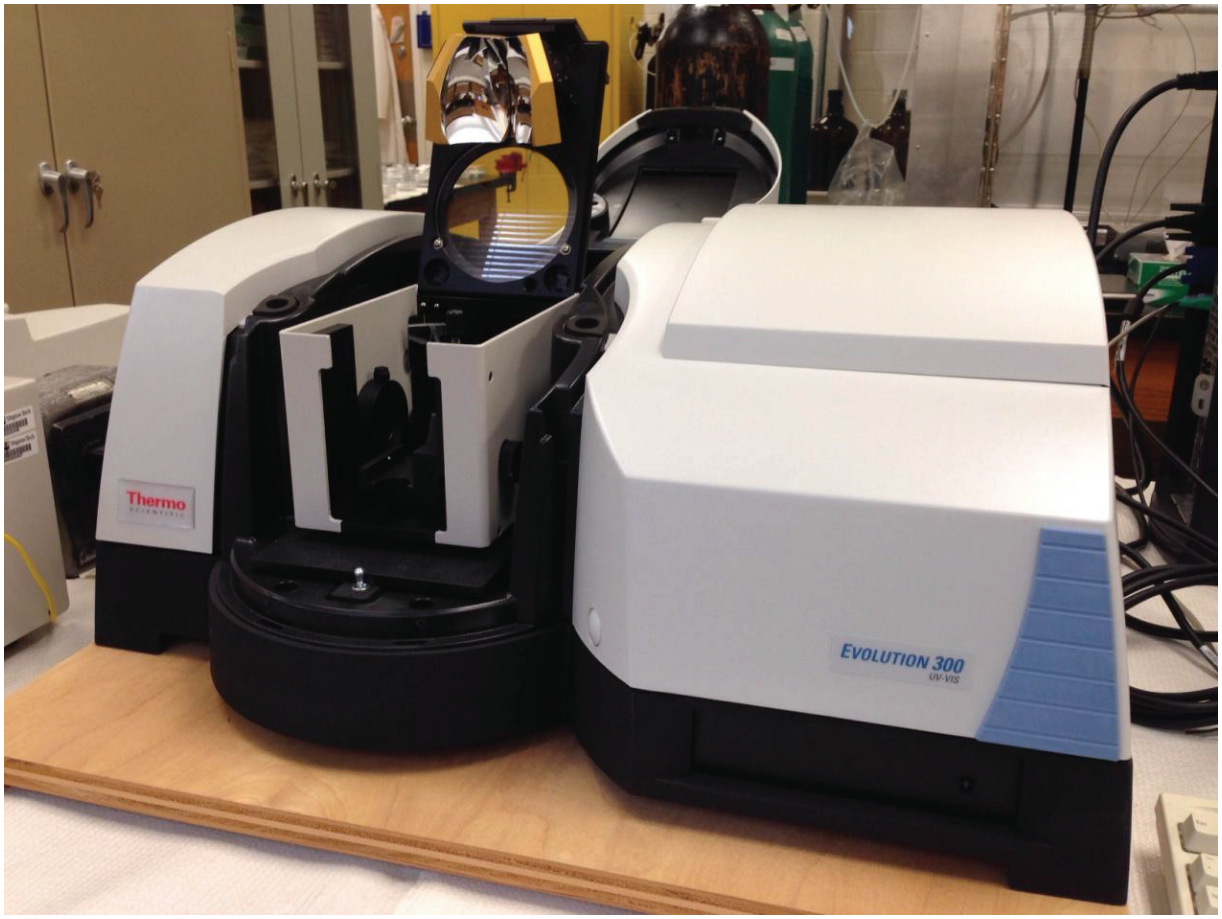

Figure 2.2: Picture of the Evolution 300 UV-Vis spectrophotometer equipped with a Praying Mantis diffuse reflectance accessory.

2.3 Electrical characterization

2.3.1 Electrode fabrication

Electrodes are fabricated on the hydrothermal synthesized materials for electrical characterization. Depending on the objective of the chosen characterization technique, a different contact type is fabricated. The details of each fabricated contact will be discussed in their respective chapters. In this section, only the common contact fabrication technique is introduced.

Before the contacts are fabricated, we first clean the samples. High-level cleaning is necessary for good contact between the electrodes and sample. The cleaning process is altered depending on the property of the sample. The workable cleaning methods include scratching with a wood stick, wiping with filter paper, and soaking or rinsing with deionized water (DI water), acetone (ACE) or isopropanol (IPA). A substrate is needed to hold the sample and electrode. At room temperature measurement, glass chips cut from Corning pre-cleaned 75 x 25 x 1 mm micro slides are used. At higher temperature, 5 x 5 x 0.5 mm, R plane Al_2O_3-sapphire wafers are chosen because of their excellent thermal conductivity and heat tolerance. The dimensions of the substrate can be modified but are limited to the size of the sample holder of the equipment. If the sample needs to be put on the 14-pin dip header, the dimensions will be limited to 19 mm by 7 mm. Figure 2.3 shows a picture of a dip header with contacted samples. If mounted to the ColdEdge open cycle CoolTran system (detailed description in subsection 2.3.4.1), the dimensions are limited to 25 mm by 7 mm. Different electrode materials are adopted. An EPO-TEK H20E silver conductive epoxy is used for measurement at temperatures lower than 473 K, while a PELCO high performance silver paste can be used at higher temperatures up to 1200 K. All the contact material can be cured at 318 K overnight. The contacted samples are connected to the measurement equipment with silver or gold wires. For the room temperature measurement performed on a 14-pin dip header, the contacted sample is attached to the dip header using Apiezon N grease, and the gold wire connecting the contact sample is soldered to the dip header with indium. Indium and Apiezon N grease are both stable at room temperature but not at a higher temperature. At a temperature higher than 430 K, which is the melting point of indium, high temperature solder is used. For samples to be mounted to the ColdEdge open cycle CoolTran system, the silver wire is clipped to the screws of the dips of the ColdEdge sample holder.

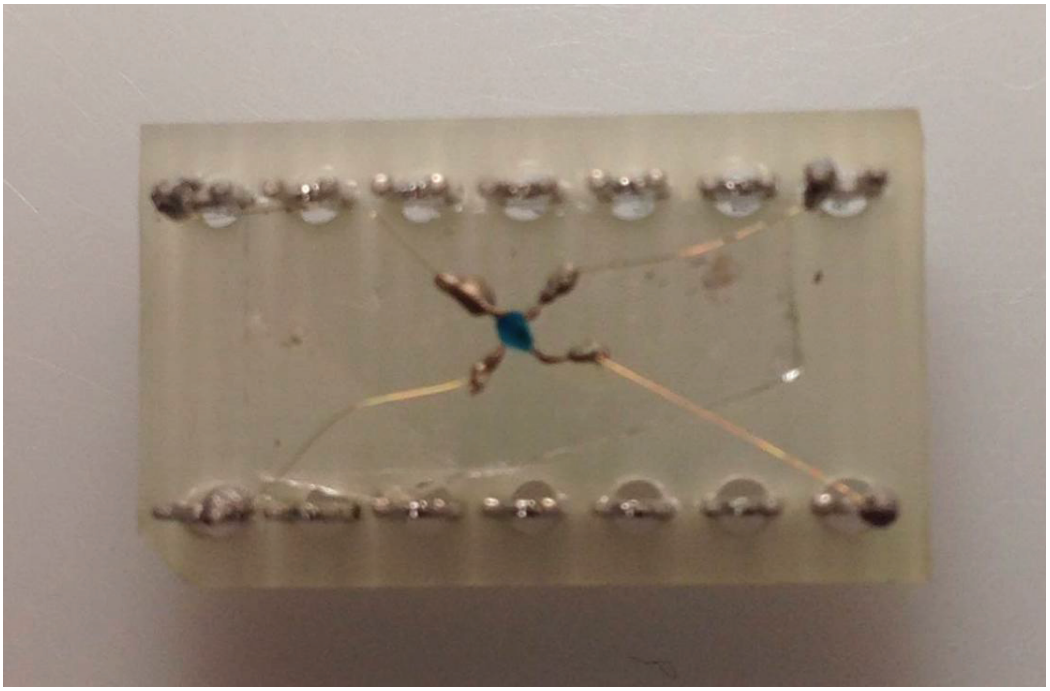

Figure 2.3: Representative picture of a dip header with a sample with four silver contacts.

2.3.2 DC electrical conductivity measurement

The DC electrical conductive property is investigated using both the 2-point method and the 4-point method. The technique for contact fabrication is discussed in subsection 2.3.1. The 2-point method needs two contacts on opposite sides of the sample. It is performed alongside the 4-point method to provide a comparison. Current-voltage (I-V) measurement is performed with the Keithley 2400 source meter. A voltage sweep with specified range, rate and interval is applied between two contacts, and the current is monitored at the same time. From the measured I-V curve, the resistance of the sample is extrapolated. We obtain the electrical conductivity from the dimensions of the sample.

The 4-point method is preferred to avoid the effects of contact resistance and provide a more

precise calculation of the conductivity by the method for measuring electrical resistivity from H. C. Montgomery [44]. Four contacts are made at four angles of the sample. Measurement is performed using the Keithley 2400 source meter. We apply variable current between two of the four contacts and monitor the voltage difference between the other two electrodes. As shown in Fig. 2.4, the sample has dimensions l_1, l_2 and l_3. The conductivity can be calculated by the equation:

$$\sigma = 1/HER \tag{2.1}$$

where σ is the conductivity and H is a function of l_2/l_1, which is obtained from the plot in Fig. 2.4; E is effective thickness; and R is the resistance obtained from the I-V curve.

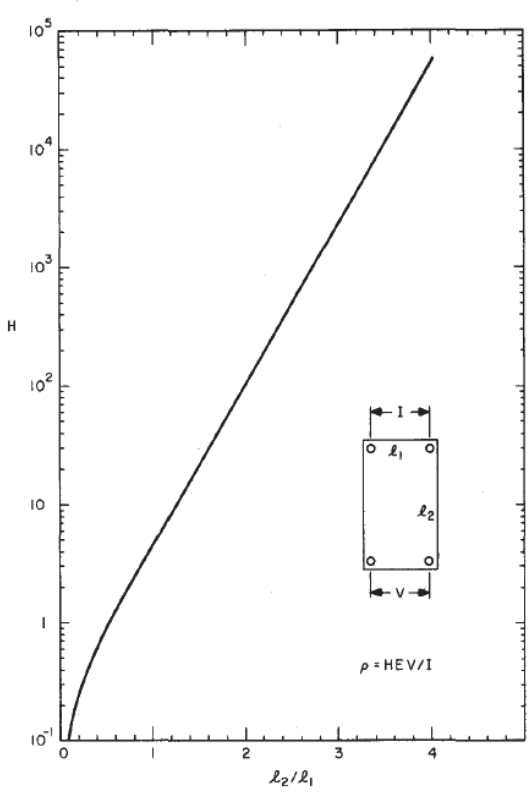

Figure 2.4: The relation between function H and sample dimensions (from reference [44]).

2.3.3 Impedance spectroscopy

The impedance spectroscopy provides AC information complementary to the DC electrical measurements. The material under investigation is considered as an equivalent two-component parallel combination of one capacitor and one resistor, as shown in Fig. 2.5(b). The equivalent impedance is calculated by:

$$Z = Z' - iZ'' = (1/R + i\omega C) \tag{5.2}$$

with real part:

$$Z' = R/[1 + (\omega RC)^2] \tag{5.3}$$

and imaginary part:

$$Z''= R[\omega RC/(1 + (\omega RC)^2] \tag{5.4}$$

where ω is the frequency, R is the resistance and C is the capacitance. Cole–Cole plot in Fig. 2.5(a) is plotted with the imaginary (Z″) as a function of the real (Z′) part of the impedance [45, 46]. Frequency ω increases in the counter-clockwise direction. From the Cole–Cole plot and the frequency, we can obtain the resistance and capacitance of the material. The maximum of Z′ is at the smallest frequency, and the joint of the Cole–Cole plot and x axis on the right hand side provide the resistance R. Z″ has the maximum when ωRC is equal to 1. We can thus calculate the capacitance C. We use a Stanford SR830 DSP lock-in amplifier and a Perkin–Elmer 7225 DSP lock-in amplifier to perform an impedance spectroscopy study of our crystalline sample. A constant voltage is applied. The real and imaginary parts of the current are obtained at a frequency between 0.001 Hz and 50000 Hz. We then obtain the variation of the imaginary part of impedance

as a function of frequency, and the variation of real and imaginary parts of impedance in the form of Cole-Cole plots. The waiting time for each data point taken is not the same. At a lower frequency, the waiting time is longer as the lock-in amplifier needs a longer time to equilibrate.

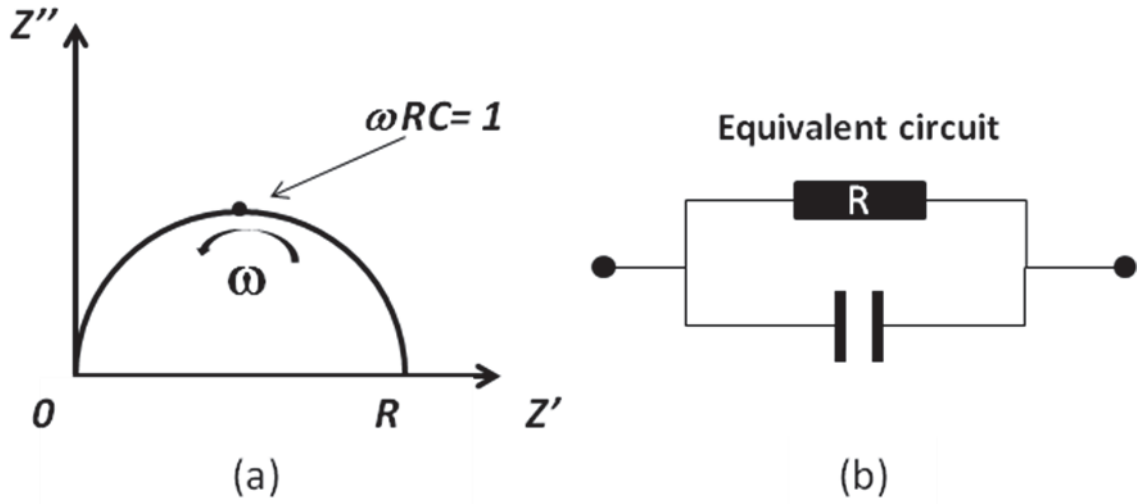

Figure 2.5: Circuit of two-component parallel combination of one capacitor and one resistor (b), and its Cole–Cole plot (a).

2.3.4 Variable temperature measurement technique

In this subsection, two variable temperature systems are described, which are a commercial ColdEdge open cycle CoolTran system and a home-built quartz tube variable temperature system. We introduce the experimental setup and their temperature control mechanisms.

2.3.4.1 ColdEdge open cycle CoolTran system

The ColdEdge open cycle CoolTran system was developed in our lab in 2010. It can perform

variable temperature electrical measurements from 78 K to 810 K in a vacuum environment. The system includes a temperature control system and a sample holder in a sample chamber that can be vacuumed. The temperature control system contains a built-in heater, a cooling system using liquid nitrogen flowing through a vacuumed transfer line, and a built-in thermocouple to read the sample temperature. We obtain the desired temperature from the equilibrium of the heater and the cooling system, which is controlled by a Lakeshore 331 temperature controller. Figure 2.6 shows a view of the ColdEdge open cycle CoolTran system.

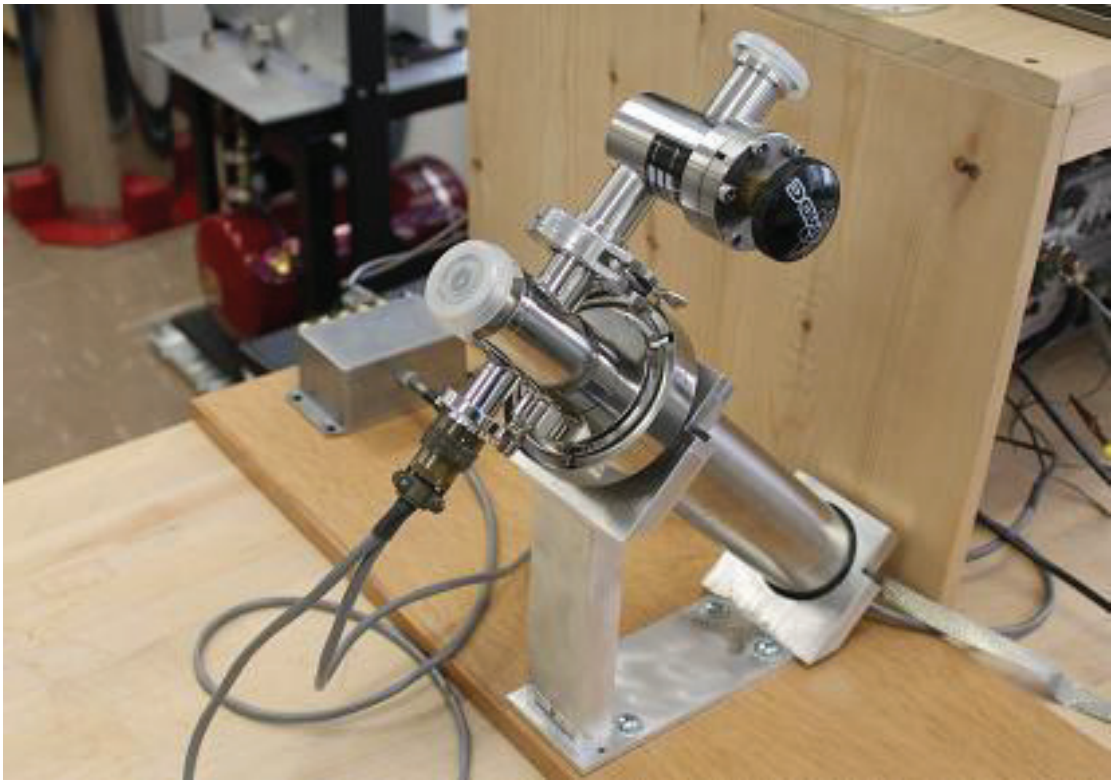

Figure 2.6: Picture of part of the ColdEdge open cycle CoolTran system.

We redesigned the sample holder to fit our electrical measurement requirements. Figure 2.7(a) shows the factory-designed sample holder. It is constructed with a copper plate and 10 pins

separated from the copper plate by ceramic columns. Samples are soldered to the pins. After several uses, the 10 ceramic columns, which should be electrically isolated, become conductive because of residue from the solder and the organic component inside the crystal samples (oxo-vanadium arsenate frameworks in chapter 4). We rebuilt the sample holder as shown in Fig. 2.7(b). With this new design, the copper in the middle benefits the thermal transfer, and the ceramic pieces made by MACOR machinable glass ceramic on both sides, which are replaceable if residue accumulates on them, ensure electrical insulation between pins. Stainless steel screws are used as pins so that no solder is needed, which reduces the likelihood of residue.

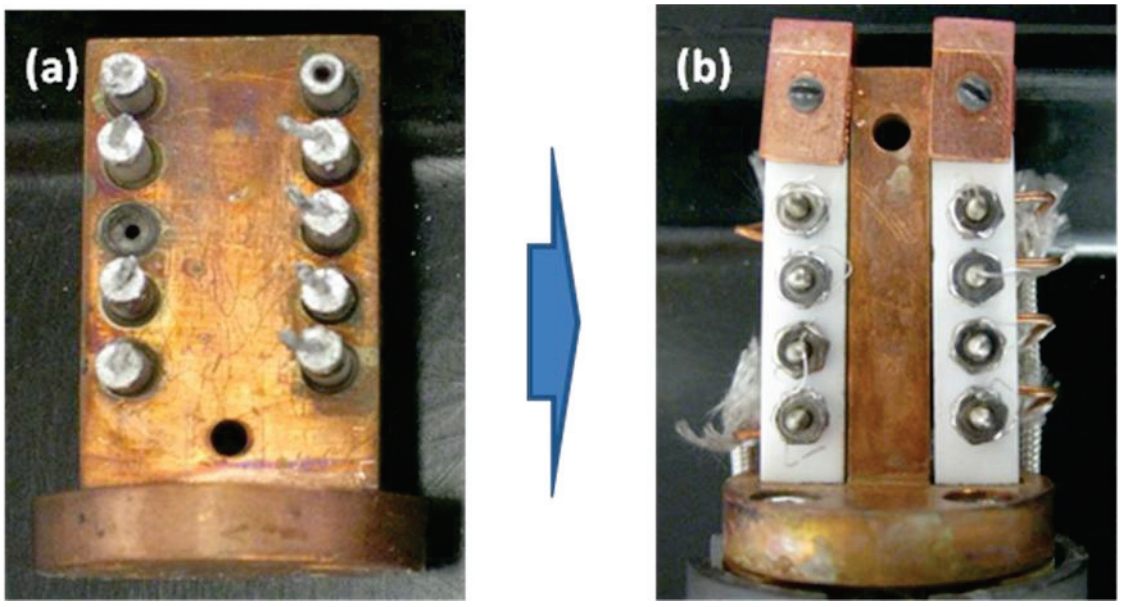

Figure 2.7: The factory designed sample holder (a) and the rebuilt sample holder (b) for the ColdEdge open cycle CoolTran system.

We then clip the silver wire connecting the sample to the screws and perform a temperature recalibration for the new sample holder, using a platinum thermocouple attached to test the temperature of the sample holder. Figure 2.8 shows the recalibration result. The x axis represents

the temperature of the sample holder, while the y axis represents the temperature read from the built-in thermocouple. The temperature deviation in the sample holder reading from the built-in thermocouple is tiny and can be ignored.

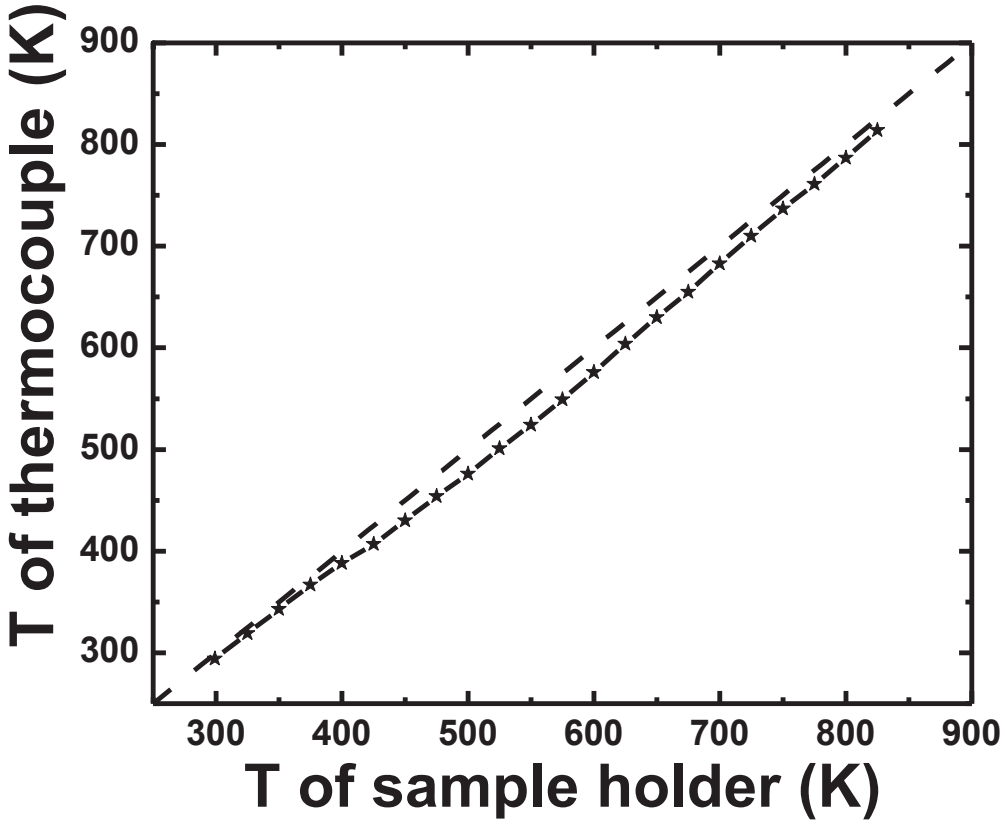

Figure 2.8: Temperature recalibration for the rebuilt sample holder of the ColdEdge open cycle CoolTran system.

2.3.4.2 Home-built quartz tube variable temperature measurement system

In this subsection, a home-built system for variable temperature measurement is discussed, which we call the home-built quartz tube variable temperature measurement system. Unlike the

ColdEdge open cycle CoolTran system, which can be used to perform both high and low temperature measurement, the home-built quartz tube variable temperature measurement system can go only up to 473 K. Samples should be first soldered to a mounting package (14-pin dip header) as shown in Fig. 2.3. The dip header is then mounted into the sample holder inside the quartz tube. As shown in Fig. 2.9, the home-built quartz tube system is equipped with a quartz tube, a sample holder for electrical measurement where the dip head is mounted, a heating system and two thermocouples. The sample holder is located in the middle of the quartz tube. The heating system enlaces the resistance heating wires around the right side of the quartz tube. Two PID controllers are utilized to control the temperature of the resistance heating wires. The heating wires heat the nitrogen gas in the right side of the quartz tube. Nitrogen then flows from right to left to transfer heat to the sample. A gas valve on the right is used to control the nitrogen flow. The temperature can be controlled by both the PID controllers and the nitrogen gas valve. Two thermocouples are used to read the sample temperature. One thermocouple is placed below the sample, while the other is placed above the sample. The reading from the upper thermocouple is always higher due to the rising of hot air. The temperature of the sample is calculated as the average of the two read temperatures. During the measurement, the nitrogen flow should be started 5 minutes before heating to fill the quartz tube with nitrogen and remove reactive gasses like oxygen, and should be kept flowing after measurement until the equipment has returned to room temperature.

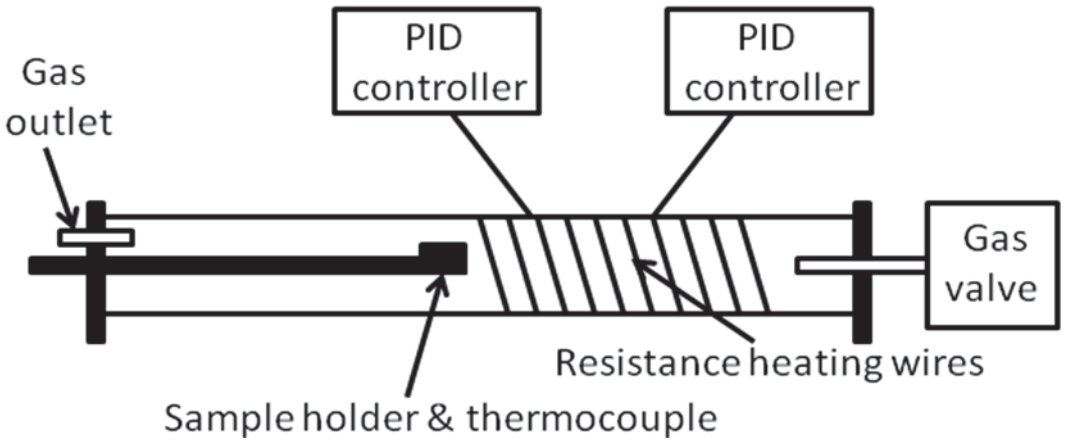

Figure 2.9: Schematic for the home-built quartz tube variable temperature measurement system.

2.3.5 Electrochemistry

Electrochemistry studies the interaction between electrical energy and chemical reaction taking place at the interface between two phases. An electrochemical reaction is driven by an externally applied voltage or creates a voltage, which is also called an oxidation-reduction (redox) reaction. Electrochemistry plays an important role in energy storage. In the work introduced in this article, we have performed electrochemical measurements not only on the solution state electrolyte but also on the solid state electrolyte, which are discussed in the following subsection.

2.3.5.1 Solution state electrochemistry

The solution state electrochemistry study is performed on vanadium oxide nanosheets material and $[NH_4]_3[V_xM'_{1-x}F_6]$ material. The details are discussed in Chapters 3 and 6, respectively. Here we introduce the commonly used voltammogram measurement technique for the solution state electrochemical study. Figure 2.10 shows the experimental setting. A complete electrochemical

cell is obtained by combining a working electrode (WE), a counter electrode (CE), a reference electrode (RE) and an electrolyte solution. In our experiment, the working electrode, the counter electrode and the electrolyte solution depend on the purpose of the experiment; while the Koslow silver/silver chloride reference electrode 1004 is always used as the reference electrode. The electrodes are connected to a Keithley 2400 source meter and a Keithley 2000 multimeter as shown in Fig. 2.10. The Keithley 2400 source meter is used to provide the voltage sweep between the working and counter electrodes, while the Keithley 2000 multimeter is used to monitor the voltage between the working and reference electrodes. We perform the voltammogram measurement using different voltage sweep ranges, sweep rates and voltage intervals.

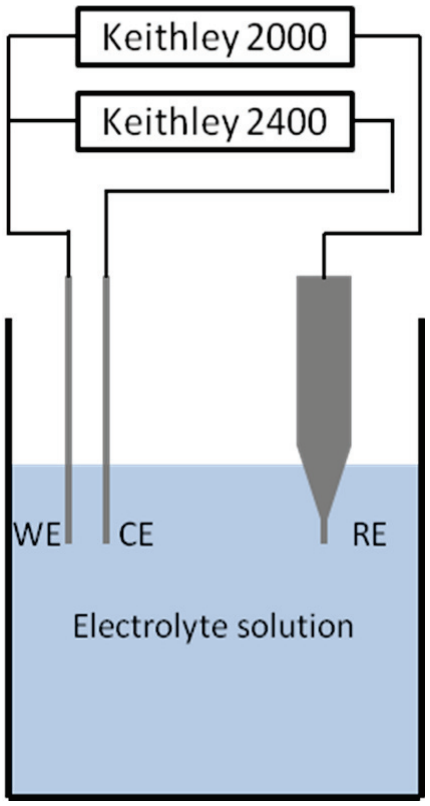

Figure 2.10: Schematics of the experimental setting for solution state electrochemical measurement.

2.3.5.2 Solid state electrochemistry

Solid state electrochemistry studies the solid state electrolyte. We perform the solid state electrochemical measurement of $[NH_4]_3[V_xGa_{1-x}F_6]$ crystal in Chapter 6. In this subsection, we introduce the technique used for the solid state electrochemistry study. Four silver contacts are fabricated on the crystal samples using the technique discussed in 2.3.1. Then three of the four contacts are chosen as working electrode (WE), counter electrode (CE), and pseudo-reference electrode (PRE) to perform a 3-point electrochemical measurement. The 3-point measurement combines a 2-point current-voltage measurement with the Keithley 2400 source meter, and a voltage measurement with the Keithley 2000 multimeter. As shown in Fig. 2.11, the two measurements share the working electrode. V_3 is the voltage obtained by the Keithley 2000 multimeter for the 3-point measurement, which is the voltage between working and pseudo reference electrodes, while V_2 is the voltage sweep provided by the Keithley 2400 source meter for the 2-point method, which is the voltage between working and counter electrodes. It is similar to the measurement system for solution state measurement. In the 3-point measurement, a silver electrode serves as the pseudo reference electrode. There is a special geometry requirement of the reference electrode placement in the solid electrolyte [47, 48]. In our experiment, the microelectrode concept is employed for the reference electrode, which will be presented with results and discussion in Chapter 6. The pseudo-reference electrode provides a constant potential, but the potential is attributed to the composition of the electrolyte and is unknown. To provide a certain reference potential, an Ag/AgCl reference electrode system is designed to standardize the voltammogram data. Figure 2.12 shows the sketch of the measurement setting for the solid state electrochemical measurement with an Ag/AgCl reference electrode system on the left.

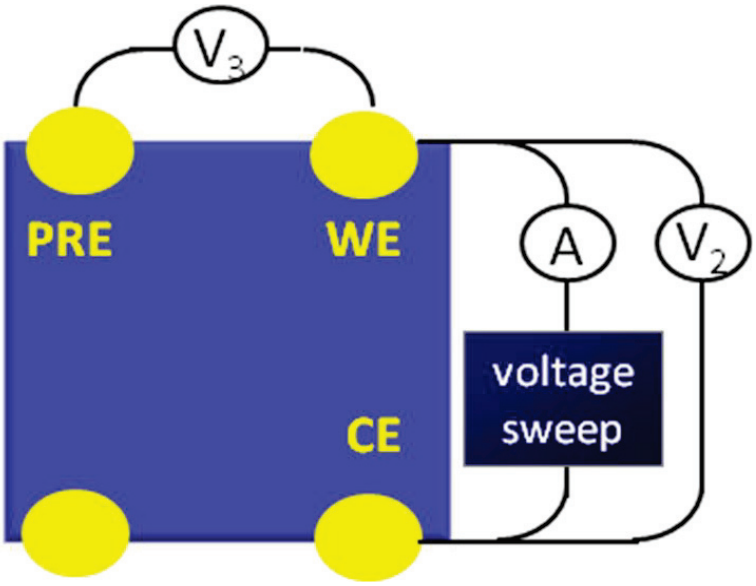

Figure 2.11: Schematic diagram of the solid state voltammogram measurement set-up with pseudo reference electrode.

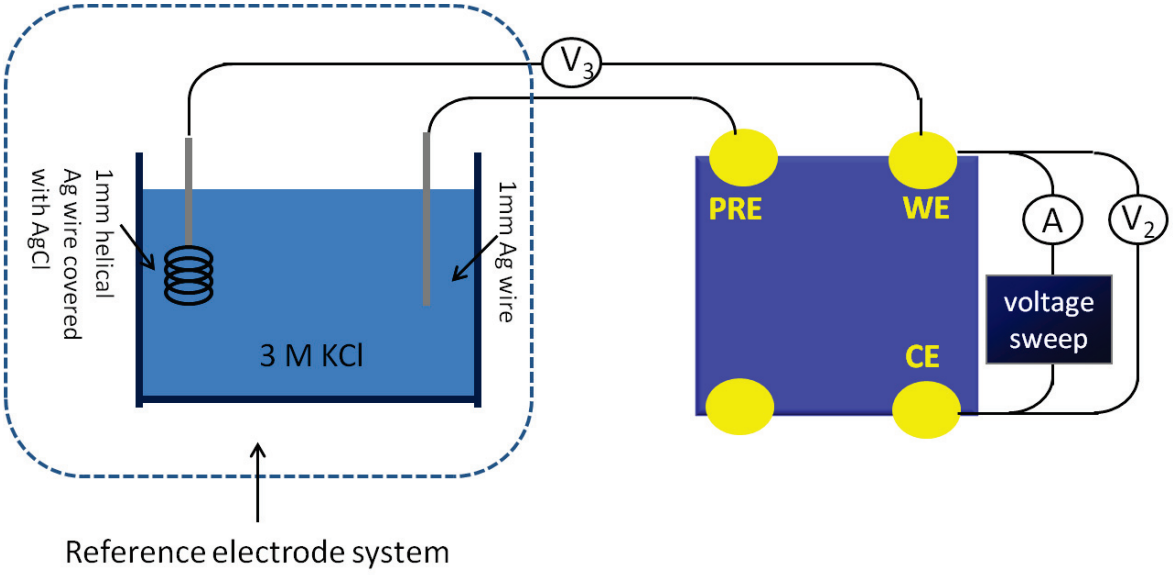

Figure 2.12: Schematic diagram of the solid state voltammogram measurement set-up with an Ag/AgCl reference electrode.

To obtain a stable and reproducible reference electrode that can be used under a variety of conditions, a home-built Ag/AgCl reference electrode is constructed from a 1 mm diameter Ag wire. The wire, after cleaning, is bent to a helical shape and then soaked in Clorox bleach for 1 hour. An AgCl film coating is then formed on the outside of the Ag wire. The Ag wire is rinsed with DI water, dried and used as an Ag/AgCl reference electrode [49]. The helical shape is adopted to increase the surface area of the reference electrode. A 3 M KCl solution is used as the electrolyte solution with the reference electrode system. The bare straight Ag wire with 1 mm diameter is used to connect the KCl solution electrolyte for the reference system and the solid sample. We set up the potentiometric cell assembled with the helical Ag/AgCl reference electrode against a commercial Ag/AgCl reference electrode to check the helical Ag/AgCl reference electrode. The potential drop on the helical Ag/AgCl reference electrode versus the commercial Ag/AgCl reference electrode were obtained using the Keithley 2182 as a function, and presented in Fig. 2.13. The tiny difference between the two reference electrodes can be ignored when we compare the magnitude of the drop to the peak potential in the voltammogram of the $[NH_4]_3[V_xGa_{1-x}F_6]$ crystal. The voltammogram versus pseudo electrode and versus Ag/AgCl reference electrode data will be discussed in Chapter 6.

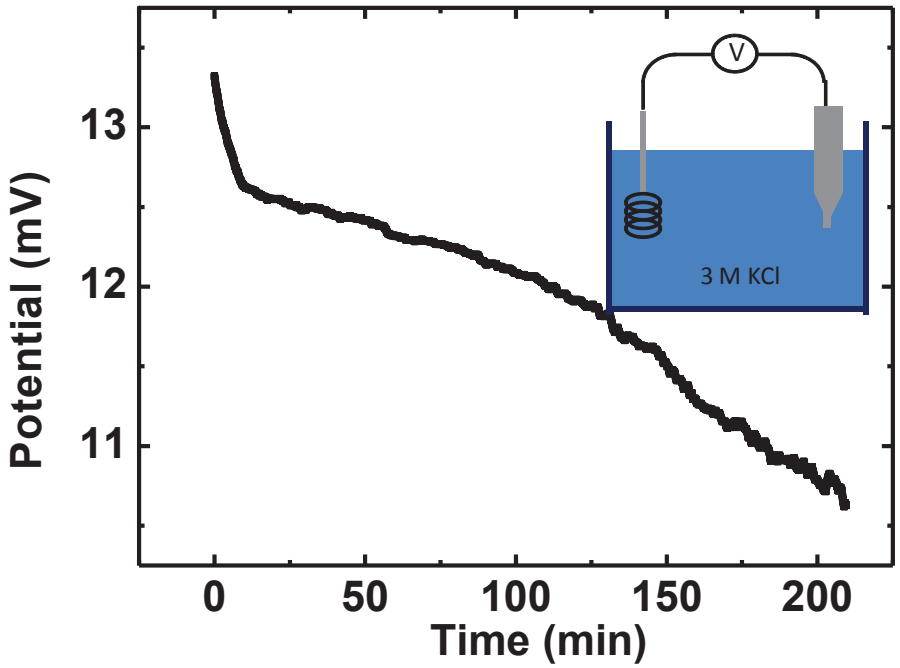

Figure 2.13: The half cell voltage of the helical Ag/AgCl reference electrode in 3 M KCl solution vs. the commercial Ag/AgCl reference electrode as a function of time.

Chapter 3 Electrochemical properties of a nanostructured vanadium oxide in aqueous salt solutions

In this chapter, we present a comparative electrochemical study of a nanostructured vanadium oxide material in chloride solution of different cations. Electrochemical energy storage plays an ever increasing role in the demand for effective, reliable and safe energy storage solution. Li-ion batteries are used as the main power sources in a variety of applications, such as mobile phones, laptop computers, medical devices and hybrid electric vehicles, and offer higher theoretical specific capacity and energy density than comparable energy storage devices because of the low atomic number and low redox potential of Li ion [50, 51]. Li ions serve as charge carrier diffusing into electrode materials. Their small ionic size facilitates fast kinetics and as a result permits the remarkable electrochemical performance observed [52]. Li-ion batteries are a mature technology for energy storage, yet come with issues include cost, Li supply, safety, reliability and stability [53, 54]. Approaches to mitigate the issues include use of different cations [54-56], electrolytes —solid [57], solid ionic liquid [58], organic ionic plastic [59] or polymeric [59-61] —with simultaneous investigations into the synthesis of new materials to address energy storage needs.

Metal oxides are ubiquitous, with applications ranging from catalysis to energy storage. Various vanadium oxides and nanostructured vanadium oxides garner considerable interest as ion insertion material for electrochemical energy storage [26, 53, 62-69]. In previous studies [26, 63-70], the results have indicated that nanostructure may improve the electrochemical properties of vanadium oxides compared to bulk material. The morphology of nanostructured materials suggests large available space for higher ion or molecule mobility, large accessible surface area for ion insertion and extraction [63, 71] and also short diffusion length for electrode rate capability [26]. These

features grant the material both battery-like electrochemical character and capacitor pulse-power-only electrochemical character which allow for an electrochemical storage device with both higher attainable energy density and achievable power density. However even with optimized nanostructures, Li-ion batteries with vanadium oxide electrode material are constrained and limited to meet the cycling stability requirement which is the major concern for long-term operation and advanced applications [72, 73].

To provide an alternative choice to Li-ion batteries, the development of new charge carrier is critical for improvement of electrochemical energy storage systems. Ions other than lithium are considered as charge carriers for secondary batteries, for example Mg^{2+}, Al^{3+}, and Zn^{2+}, when inserted into vanadium oxide aerogels showed excellent electrochemical activity [74]. Moreover, Na has attracted tremendous attention as a promising battery functional ion [54, 75, 76].

In this chapter, we report a nanostructured vanadium oxide material[77]. The hydrothermally synthesized vanadium oxide material is electrically characterized by variable temperature measurement. We also report the comparative study of the electrochemical insertion process of different cations into the same vanadium oxide material. The choice of alkali cations, Li^+, Na^+ and K^+, as well as the ammonium NH_4^+ ion aims at investigating the possibilities of using cations other than Li^+, which are more abundant and less costly, with acceptable performance in electrochemical energy storage applications. The electrochemical behavior of the vanadium oxide material as a function of various cations and cycles is investigated correlated with visual changes in the vanadium oxide nanosheets as observed by scanning electron microscopy and the specific charge adsorbed per cycle in the voltammogram cyclic experiment.

3.1 Physical characterization

The vanadium oxide material under investigation was obtained by hydrothermal synthesis, and the isolated material is rinsed with deionized (DI) water and subsequently dried in air. The vanadium oxide is isolated as the major product in the form of folded nanosheets crumpled into a quasi-spherical 3-dimensional object, (henceforth referred to as 3D VO) affording a large and accessible surface area. Morphological characterization of the sample was performed using a scanning electron microscopy (SEM), and the folded sheets are observed in the SEM image shown in Fig. 3.1. The diameter of a sphere on average is about 200 μm.

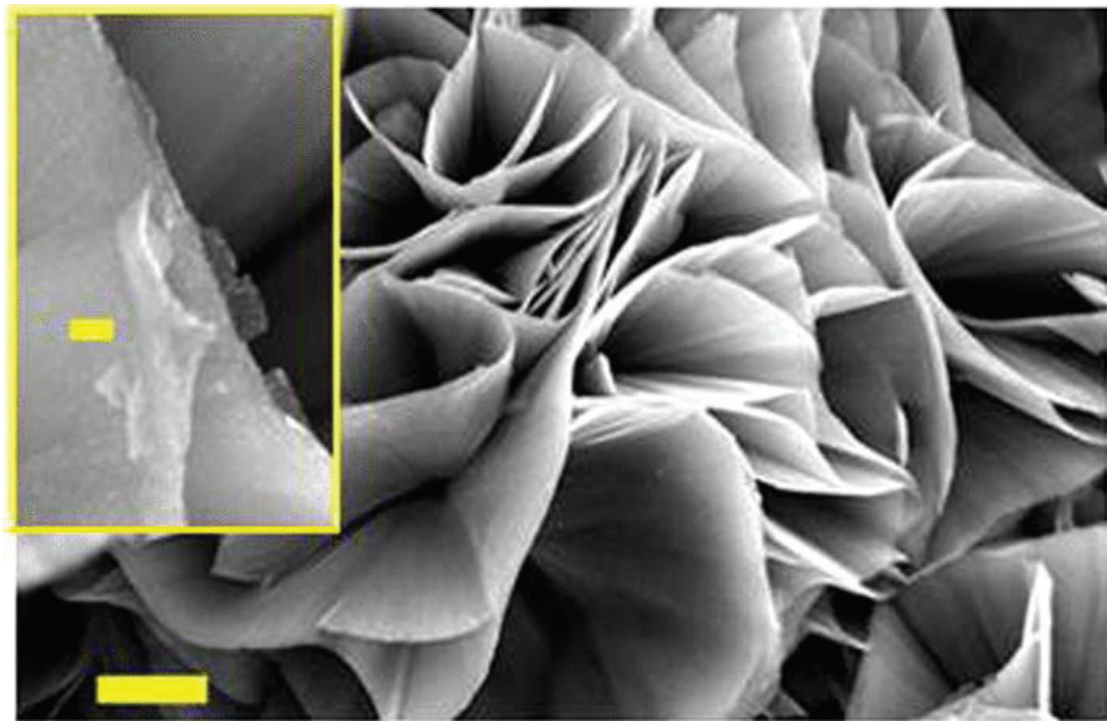

Figure 3.1: Scanning electron micrograph of the nanosheets assembled into a sphere. Scale bar on large image, 10 μm; inset, 1 μm.

The 3D VO spheres were attached to W wires by H20E Epotek silver conductive epoxy to fabricate electrodes for electrochemical measurement as described in section 3.3. The SEM experiments were performed on the electrodes and the surface of the vanadium oxide spheres before and after various cations insertion were studied. The surface change before and after electrochemical measurement with various chloride solution electrolytes will be described in section 3.3. Elemental analysis was performed by inductively coupled plasma optical emission spectroscopy, x-ray photoelectron spectroscopy (XPS) and energy dispersive x-ray spectroscopy analysis. The vanadium content of the sample is roughly 40% by weight among the various analyses. A few percent of Ga is also consistently present in all analyses. XPS data shows the presence of both V^{+4} and V^{+5} oxidation states, and the mixed valence is also supported by the dark green color of the 3D VO spheres. Combining the results of the various analyses, a reasonable suggested composition can be expressed as $VO_{2.2\text{-}2.4}$, with Ga acting as a potential dopant at less than 2% by weight. The electrochemical activity observed in the electrochemical measurement (in section 3.3) might correspond to reduction of the V^{+4} and V^{+5} by the various cations insertion processes into the 3D VO nanosheets. The density of the material is 3.08 g/ml as determined by the floatation method in CH_2I_2/CH_2Cl_2.

3.2 Electrical characterization

Variable temperature conductivity measurements were performed in the temperature range 80 K to 700 K. Two samples, each with two contacts on one single 3D VO sphere were fabricated for a lower temperature range measurement from 80 K to 350 K and a higher temperature range measurement from 290 K to 700 K respectively. The single 3D VO spheres were washed with DI water and air dried first. The two contacts were made on opposite sides of one sphere with H20E Epotek silver conductive epoxy for the lower temperature range and with PELCO high

performance silver paste for the higher temperature range respectively on a 5 x 5 x 0.5 mm, R plane Al_2O_3-sapphire wafer from MTI Corporation. Both samples were cured at 318 K for about 12 hours. The samples were connected and mounted to the ColdEdge open cycle CoolTran system (detailed description in Chapter 2) with silver wires. The variable temperature conductivity measurements were performed with Keithley 2400 source meter, which applied voltage sweep from -10 V to 10 V then back to -10 V between two contacts and recorded the current. The resistance information was extracted from the voltage and current measured. Then we calculated the conductivity from the resistance taking account of both the size of the single 3D VO spheres and the position of the electrode by the method for measuring electrical resistivity from H. C. Montgomery (detailed description in Chapter 2) [44].

Initially, both samples were measured at room temperature (about 300 K) and atmospheric pressure and then subjected to vacuum at a base pressure of 10^{-6} Torr for 3 hours. The conductivity values obtained which are due to the material itself plus adsorbed water decrease as the samples are subjected to vacuum. The room temperature conductivity values of the two measurements under vacuum are around 1×10^{-7} $\Omega^{-1}cm^{-1}$, and the difference between them is not significant. The variable temperature data was taken after the conductivity measurement at room temperature was stabilized under vacuum, indicating the minimization of contributions from adsorbed water. In the lower temperature range measurement, we decreased the temperature step by step from room temperature and simultaneously performed the same conductivity measurement as at room temperature every 10 K with waiting time of 15 min for each measurement. Then the sample was warmed-up to room temperature and the conductivity value obtained again. Data from room temperature to 350 K was obtained with the same temperature step and waiting time. In the higher temperature range measurement, we increased the temperature from 290 K to 800 K with a

temperature increment 20 K and waiting time of 15 min, and obtained the conductivity information in the same manner as in the lower temperature range. The conductivity values obtained from both samples in the temperature range from 290 K to 350 K overlap nicely. We combine the two data sets and the plot is presented in Fig. 3.2. The increase in conductivity as the temperature increases indicates semiconducting behavior. The data indicates two regions, below 350 K and above 350 K. In both the two regions, we observe the exponential dependence of conductivity upon temperature. We assume an Arrhenius type equation for the temperature dependence of the electrical conductivity [78]:

$$\sigma = \sigma_0 e^{-\frac{E_A}{kT}} \tag{3.1}$$

where the pre-exponent factor σ_0 is the maximum electrical conductivity at infinite temperature, E_A is the activation energy for the electrical conduction, T is the temperature and k is the Boltzmann constant. The activation energies E_A are calculated by the least-square straight-line fit to be 0.086 eV below 350 K and 0.51 eV above 350 K respectively.

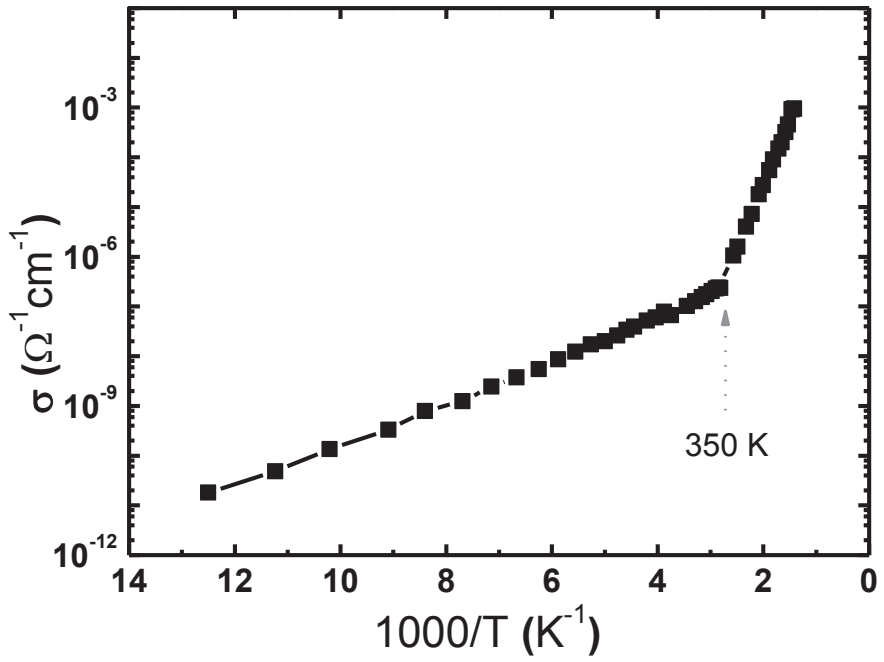

Figure 3.2: Variable temperature conductivity data from 80 K to 700 K. For T < 350 K, 10 K increments; T > 350 K, 20 K increments. Wait time between increments ~15 min throughout.

3.3 Electrochemical characterization

The 3D VO material is a promising candidate to be used in electrical energy storage application as the large surface area for ion insertion as well as adsorption offered by the nanosheets. We performed a comparative study for the electrochemical insertion of different alkali cations as well as ammonium cation into the 3D VO material. Electrodes are constructed from tungsten, 99.95% (metals basis) annealed W wire with 0.5 mm diameter from A Johnson Matthey Company cut into segments of length 60 mm, and scrubbed with Scotch-Brite Scour Pad, washed with DI water and air dried. The working electrode (WE) and counter electrode (CE) were each fabricated by

attaching 20 3D VO spheres to one end of the W wires with H20E Epotek silver conductive epoxy in a line of length 6 mm and cured at 318 K for 12 hours. The commercial Ag/AgCl reference electrode (RE) from Koslow Scientific Company was adopted. The electrochemical cell was assembled in a 30 ml beaker of diameter 32 mm with 20 ml 3M aqueous chloride solutions of various cations respectively as electrolyte. Reagent grade lithium chloride, sodium chloride and potassium chloride crystals from Spectrum Chemical Mfg. Corp. and 98+% ammonium chloride from A Johnson Matthey Company were mixed with DI water respectively to prepare the electrolytes. The Schematics of the electrochemical measurement system is shown in Fig. 3.3. The separation distance between WE and CE is 2.5 mm and between CE and RE is 15 mm as labeled in Fig. 3.3. The separation distances are kept constant in all the comparative measurement. The portions of the WE and CE with the 3D VO spheres attached are immersed into the electrolyte. A Keithley 2400 source meter applies voltage sweeps between the WE and CE, and the voltage of the WE versus the Ag/AgCl RE is obtained by a Keithley 2000 multimeter. Baselines were obtained by measuring two W wires covered with silver epoxy (up to 6 mm) as the WE and CE, Ag/AgCl as the RE, in 3M aqueous solutions of each of the chloride salts in the same experimental setting as described above.

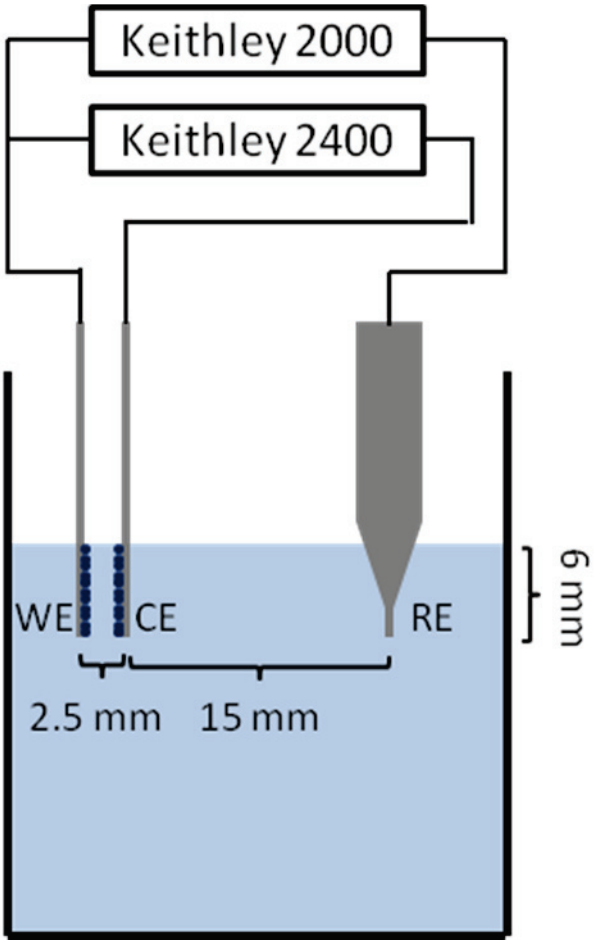

Figure 3.3: Schematics of the experimental setting for electrochemical measurement of the 3D VO materials in chloride aqueous solution of various cations.

The electrochemical measurements were all performed at room temperature, about 300 K. To investigate the effects of cation insertion into the nanosheets, we performed cyclic voltammetry measurement in 3M LiCl, NaCl, KCl, and NH_4Cl aqueous solutions both with the electrodes constructed with 3D VO material and the electrodes for baseline measurement as described above. For this comparative study, the potential sweep range between the WE and CE (baseline and 3D VO material) was kept constant, -2 to 2 V, as was the scan rate of 20 mV s^{-1}. The potential of the

WE versus the RE is depicted in Fig. 3.4, indicating the response of the 3D VO material, under identical measurement conditions, to insertion/adsorption of different cations. The 1st cycle (in all the measurements) starts with the WE at -2 V versus the CE, and thus some solution cations migrate towards the WE and adsorb/insert onto the nanosheets. As the potential is swept towards more positive values, the cations de-insert from the WE. We consider that during the 1st cycle, fewer cations are adsorbed, because steady-state conditions are not yet attained. This assumption is borne out by the observation that starting with the 2nd cycle, the de-insertion peak, which occurs around +0.04 V versus Ag/AgCl in all the panels in Fig. 3.4, dramatically increases in magnitude (grey dot plus line). Thus, the 2nd cycle is used as a starting point for the comparative study among the four cations. Cation insertion into the nanosheets occurs in the range -0.16 to -0.11 V versus Ag/AgCl (Fig. 3.4 all panels). Similarly, the 2nd cycle is used for the baseline measurements of the W wires with the Ag epoxy in the respective electrolytes. Acquiring of this baseline measurements allows evaluation of the response of the 3D VO material as distinct from that of the W wire with the Ag epoxy. The 2nd cycle of the baseline measurement in each electrolyte is shown in all the panels of Fig. 3.4 (light grey line). The electrochemical insertion/de-insertion process -or the reduction/oxidation of the vanadium centers- is presented by the following Faradaic reaction:

$$V^{+m}O_n + 1M^{+1} + 1e^- \rightleftharpoons M_1^{+1}V^{+m-1}O_n \qquad (3.2)$$

where M^+ is the cation in the electrolyte. Here, we are considering that only a single cation inserts per vanadium site [26].

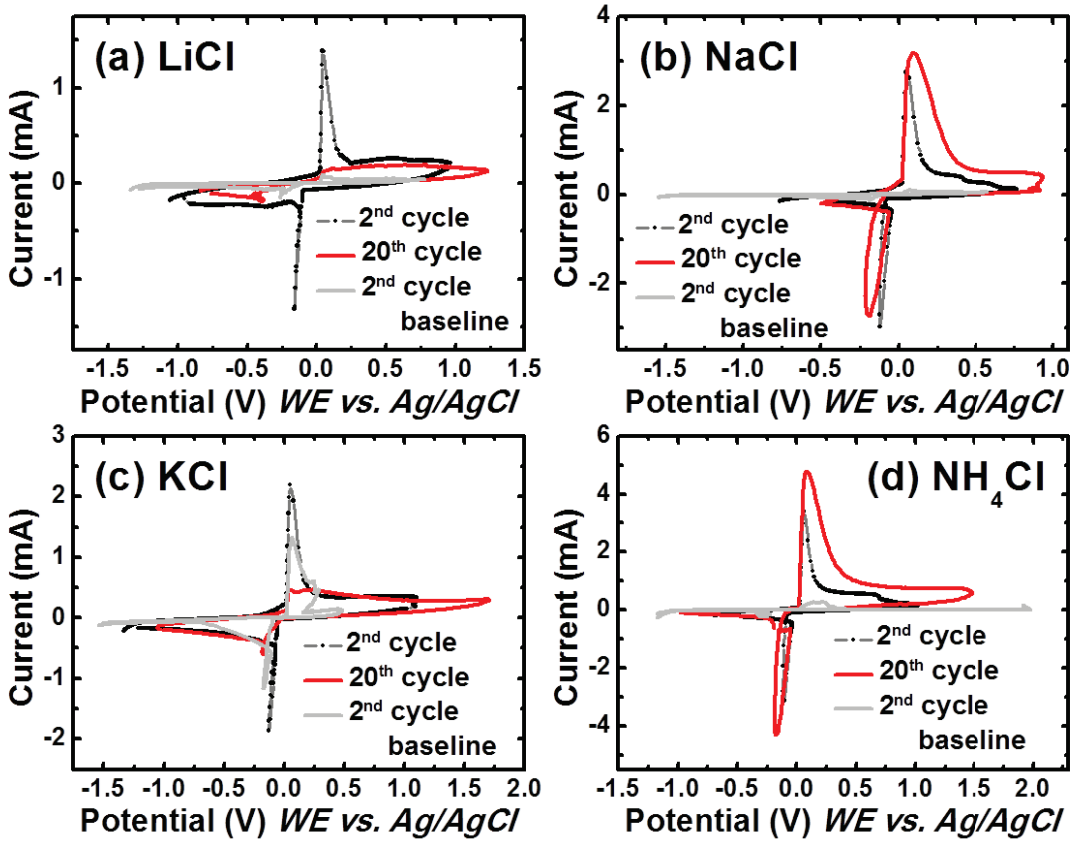

Figure 3.4: Voltammograms in 3M aqueous solutions of (a) LiCl, (b) NaCl, (c) KCl, and (d) NH_4Cl, with the vanadium oxide as WE vs. Ag/AgCl RE. In each panel, indicated are 2nd cycle of the baseline (light grey, line only), 2nd cycle (grey dot plus line), and 20th cycle (red, line only).

The response of the 3D VO material to different ion insertion processes is gleaned by inspecting the voltammograms of Fig. 3.4, coupled with the before and after images of the nanosheets obtained by SEM, depicted in Fig. 3.5. For each set of before and after images, electrodes were assembled, images obtained (all at same magnification), and the same electrodes were then placed in the appropriate electrolyte solution, voltammograms were obtained (up to 20 cycles) after which the electrodes were air-dried. The after images were obtained as close as possible to the location of

the before images. Assessing both the electrochemical data and the SEM images, a consistent observation emerges. Inspection of the voltammograms indicates that in NaCl and NH_4Cl electrolytes (Figs. 3.4(b) and 3.4(d)), the reduction/oxidation peaks increase in area as the number of cycles increase, attesting that the insertion/de-insertion is reversible in these electrolytes. Close examination of the reduction peak, especially in the case of Na^+ and NH_4^+ cations (Figs. 3.4(b) and 3.4(d)), show a loop (similar albeit much narrow loops are also present in the case of Li^+ and K^+). As the WE is swept towards more negative potential, after the de-insertion step at ~0.04 V, more cations from the solution migrate and are adsorbed onto the nanosheets in the WE. This momentary positive charge accumulation causes a shift in the potential of the WE vs. Ag/AgCl, forming the observed loop. In the case of Li^+ and K^+, this shift is very small, and we thus surmise that these cations interact strongly with the nanosheets and do not penetrate deeply into the spheres, whereas in the cases of Na^+ and NH_4^+, these ions interact less, moving across the nanosheet surfaces and deeper into the folds of the material, allowing for more cations during a cycle to insert. This assumption is consistent with the observations that in NaCl and NH_4Cl electrolytes, there is minimal material buildup on the nanosheets (determined from the SEM images in Fig. 3.5), and a concomitant increase occurs in the specific charge measured (as will be seen in Fig. 3.8). The stronger a cation binds, the less reversible the process is, leading to material buildup, which in turn prevents further electrochemical processes, and thus the specific charge diminishes or stays constant.

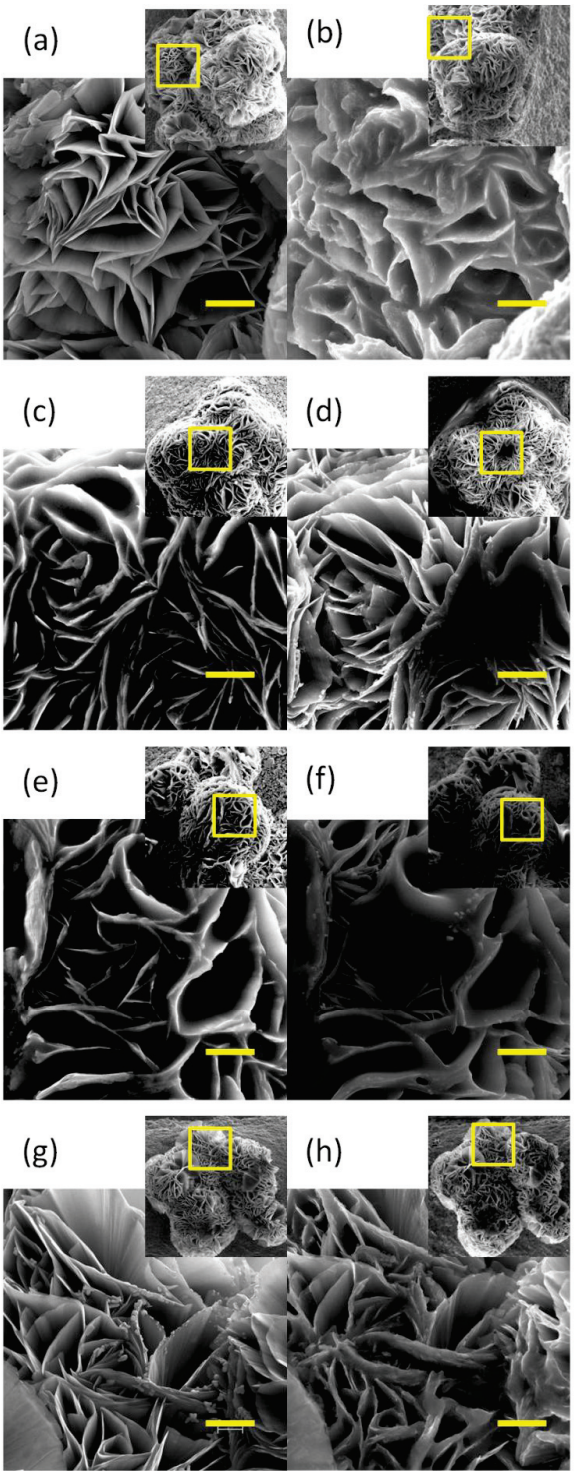

Figure 3.5: SEM images of nanosheets before ((a), (c), (e), and (g)) and after ion insertion: (b) Li^+, (d) Na^+, (f) K^+, and (h) NH_4^+. Inset in each panel (right top) shows overall location, with delineated area shown at higher magnification. Scale bar is 10 μm.

Hence, the voltammograms corresponding to processes in LiCl and KCl show a reduction of the reduction/oxidation peaks, attributable to these cations strongly adsorbing/binding to the nanosheets, resulting in irreversible electrochemical behavior and rapid degradation of the material due to the observed buildup seen in the after images, especially in LiCl electrolyte (Fig. 3.5(b)). In NaCl and NH_4Cl electrolytes, the after images (Figs. 3.5(d) and 3.5(h)) show less degradation than those obtained in LiCl and KCl (Figs. 3.5(b) and 3.5(f)). Degradation may be expressed as buildup of material on the nanosheets, seen in, e.g., Figs. 3.5(b) and 3.5(f) as thickening and coarsening of the nanosheets. We note minimal buildup with Na^+ and NH_4^+ cations as compared to Li^+ and K^+ cations. The deposited material is not soluble in water. In an attempt to reverse the degradation of the Li and K inserted nanosheets, we tried to dissolve the buildup by soaking of the electrodes in DI water for more than 12 hours. No reduction of buildup was noticed in images obtained after this step. Representative image is shown in Fig. 3.6 for the Li inserted nanosheets after soaking in DI water.

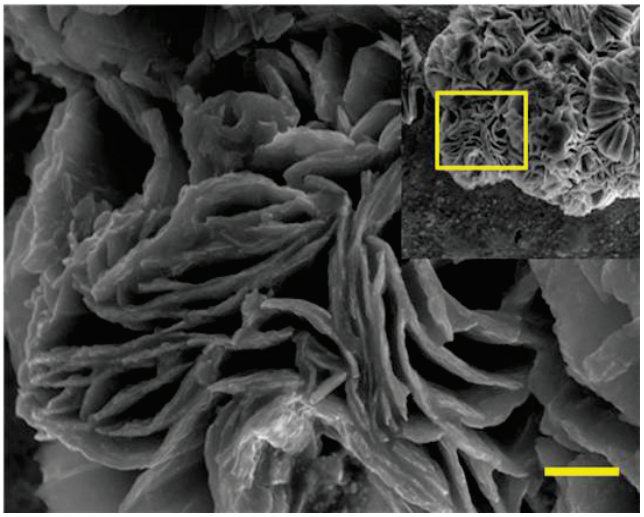

Figure 3.6: SEM images of Li^+ ion inserted nanosheets after DI water washed (soak in DI water for 12 hours), Inset in each panel (right top) shows overall location, with delineated area shown at higher magnification. Scale bar is 10 μm.

The amount of charge transferred in the insertion/de-insertion steps, as well as the specific charge per cycle for 4 different cations are calculated from the 1st cycle up to the 20th cycle in Fig. 3.7. During the cyclic voltammogram measurement, the potential is swept between WE and CE with a constant rate 20 mV s^{-1}. The voltammograms depicted in Fig. 3.4 reflect the potential difference between WE and RE which is swept with the effective scan rate (and also effective potential sweep range) vs. Ag/AgCl varying based on the response of the 3D VO material to cation insertion in a particular electrolyte. Concurrently with the 3-electrode measurements plotting in Fig. 3.4, we plot the 2-electrode current-voltage (I-V) traces as measured between the WE and CE when the potential is swept from -2 V to 2 V (WE to CE), and back to -2 V to complete a cycle. Figure 3.8 shows a representative plot of the I-V traces with voltage between the WE and CE and with selected cycle numbers for Li^+ ion only. Without a reference electrode at a stable potential, the current peaks we observed in Fig. 3.8 vary with various cycles and not provide the redox potential, yet the plots allow us to obtain current versus time information for the specific charge calculation. The charge transferred per cycle for the insertion/de-insertion process could be estimated from the current peak area in the same kind of I-V plots as shown in Fig. 3.8, using equation:

$$Q = \int IdV/R \tag{3.3}$$

here Q (C) is the charge amount transferred, I (A) and V (V) are current and voltage in the 2-electrode current-voltage (I-V) traces, and R is the constant voltage sweep rate which is 20 mV s^{-1}. The volume of 3D VO materials in the electrode is obtained assuming 20 spheres on each electrode with an average diameter of 200 μm, and density of 3.08 g/ml. The specific charge is calculated taking account of the mass of the 3D VO materials.

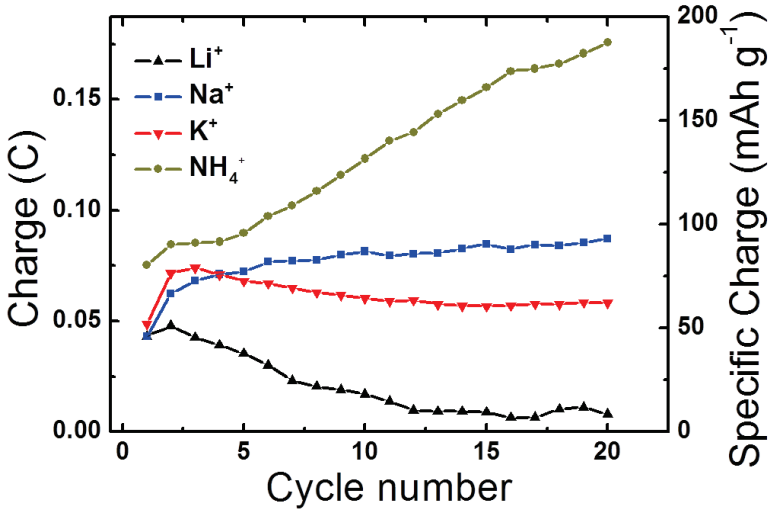

Figure 3.7: Charge and specific charge for the 3D VO material as a function of cycle number from the 1st cycle to 20th cycle for each of the cations studied.

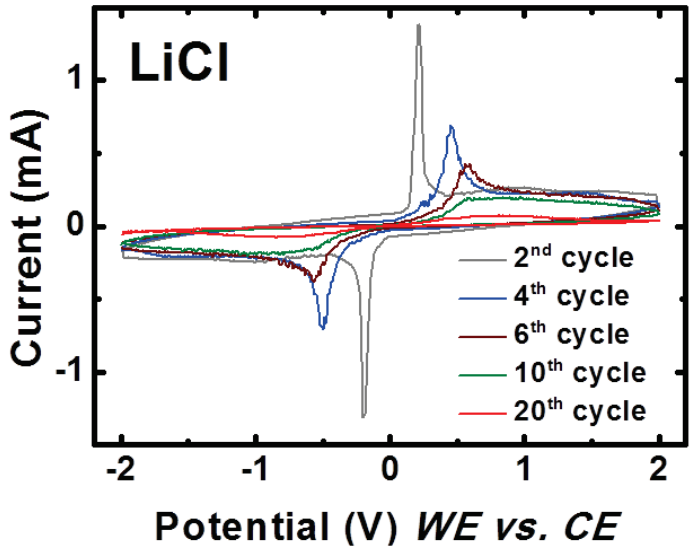

Figure 3.8: The current-voltage (I-V) traces as measured between the WE and CE in LiCl solution in 2nd cycle (grey), 4th cycle (blue), 6th cycle (wine), 10th cycle (olive) and 20th cycle (red).

From Fig. 3.7, we observe a decrease of specific charge for Li^+, and after an initial increase a slow decrease for K^+, as the number of cycles mounts. On the other hand, as the number of cycles mounts, we observe specific charge increases for both Na^+ and NH_4^+, with NH_4^+ showing the largest increase in this comparative study. This parallels the electrochemical behavior and also correlates with the degradation observed in the SEM images for Li^+ and K^+. The highest value of the specific charge is obtained for NH_4^+, 180 mAh g^{-1}, using the Faradaic reaction mentioned earlier with one cation per V site inserting into the VO material. The specific charge obtained for NH_4^+ is favorable [26, 53, 63-68, 79], especially as the electrolyte is a straightforward aqueous solution of NH_4Cl, and as measurements are performed under ambient conditions.

3.4 Conclusion

In this chapter, we report the detailed experiments and observations of electrical and electrochemical characterization of a 3D VO material. The variable temperature electrical conductivity measurements indicate semiconducting behavior. We perform cyclic voltammetry measurements on the 3D VO nanosheets in LiCl, NaCl, KCl, and NH_4Cl aqueous solution. The electrochemical behavior with different cations and various cycles are correlated with physical modifications to the nanosheets as observed by SEM, and to the amount of charge deposited as a function of cation and cycle number. The 3D VO nanosheets are electrochemically active not only in Li^+ but also Na^+, K^+ and NH_4^+ containing electrolyte. We find that Na^+ and NH_4^+ cations are viable candidates in vanadium reduction/oxidation processes for energy storage, as they cause minimal physical modifications to the vanadium oxide material, and show increase in the specific charge as a function of cycle number. The differing behavior of the various ions has implications for their use in electrical energy storage applications.

Chapter 4 Ionic and electronic properties of oxo-vanadium arsenate and phosphate frameworks

Porous materials, with ordered or irregular arrangement of pores and different pore sizes from nanometer to micrometer, contribute to various important technological processes from catalysis and separation to capacitive electrical storage [9, 14, 80-84]. Zeolitic materials consist of a broad range of porous crystalline solids are characterized by the presence of nanoscale channels and cavities delineated by their crystalline framework. [85-87] As a function of the structure, the specific surface area in zeolitic materials is high, potentially offering large electrical storage capabilities. Microporous aluminosilicate zeolite frameworks are electrically insulating but ionic conduction is measured in various zeolites as function of ion size and charge, and pore size and accessibility [88-91]. Select transition metal phosphate and arsenate three-dimensional framework materials structurally resembling zeolites may similarly support ionic conduction. The introduction of transition metals into the framework potentially allows the modification of the electrical characteristics of the framework itself, yielding mixed conductors. A promising utility of zeolite-like mixed conductors is in energy applications, *e.g.* electrical energy storage. Literature [27] reported a potential application of an electrically conducting zeolite-like framework electrical double-layer capacitor (EDLC), where the electrical energy storage is achieved by the charge separation at the interface between the electrically conducting electrode and electrolyte solution. After employing electrically conducting zeolite-like framework as electrode, both the short distance of charge separation (atomic in scale) and the large effective area supported by the microporous structure of the zeolite-like material contribute to the large attainable capacitance value of the EDLC. Yet, uses for electrically conducting zeolite-like

frameworks can be envisioned in other important energy applications, in ion-exchange membrane technologies and catalysis. It is therefore imperative to develop electrically conducting zeolite-like frameworks. In this chapter, we report two zeolite-like framework materials, a vanadium arsenate $[(As_6V_{15}O_{51})^{-9}]_\infty$, compound (1), and a vanadium phosphate $[(P_6V_{15}O_{51})^{-9}]_\infty$, compound (2) [92]. We compare the electrical characteristics of the two compounds through the measurements of conductivity as a function of temperature and extra-framework constituents. Our results indicate that compound (1) is a mixed conductor with framework electronic conduction and ionic conduction associated with the extra-framework constituents. Compound (2), in contrast, shows only ionic conductivity. Probing the electrical properties of zeolite-like mixed conductors paves the way for the innovative use of these materials.

4.1 Materials

The vanadium arsenate $[(As_6V^{IV}_{12}V^{V}_{3}O_{51})^{-9}]_\infty$, (1) and phosphate $[(P_6V^{IV}_{12}V^{V}_{3}O_{51})^{-9}]_\infty$, (2) were synthesized by hydrothermal methods to be crystalline cubes with ~50 μm edge. Figure 4.1(a) exhibits an individual crystal of (1). Both the structures of the two compounds were determined through single crystal x-ray crystallography. The crystal structure of (1) is reported in literature [93]. The structure is cubic and in the space group *Im3m* with lattice constant $\bar{a}$ equals to 16.62 Å at 100 K. As shown in Figs. 4.1(b) and 4.1(c), the V_5O_9 half pseudo spheres, which are statically disordered to form two kinds of half pseudo spheres with ratio 1:1, connect to each other via non-distorted AsO_4 tetrahedra and construct an anionic framework. The three-dimensional framework delineates a porous structure with accessible pore dimension of 4.1 Å, which allows for 37% solvent accessible void space of the total crystal volume. Organic cations and water species as

extra-framework constituents are situated within the framework cavities in order to compensate for the negative framework charge. They are usually mobile and make an allowance for the exchange with other cations such as alkali cations. Compound (2) [33, 94] was synthesized as a phosphate analog of compound (1) for comparative studies of the electronic properties of structurally similar yet compositional different materials. For compound (2), single crystal x-ray diffraction was performed at 290 K, and the vanadium phosphate framework crystallizes in the cubic space group *Im3m* with lattice constant *a* equals to 16.00 Å. The inorganic framework is similar to compound (1), with the phosphate group substituting for the arsenate tetrahedral unit. The charge balancing extra-framework constituents in (1) and (2) could not be located from the XRD data, yet has been inferred from elemental analysis, energy-dispersive x-ray, thermogravimetric analysis, and infrared spectroscopy.

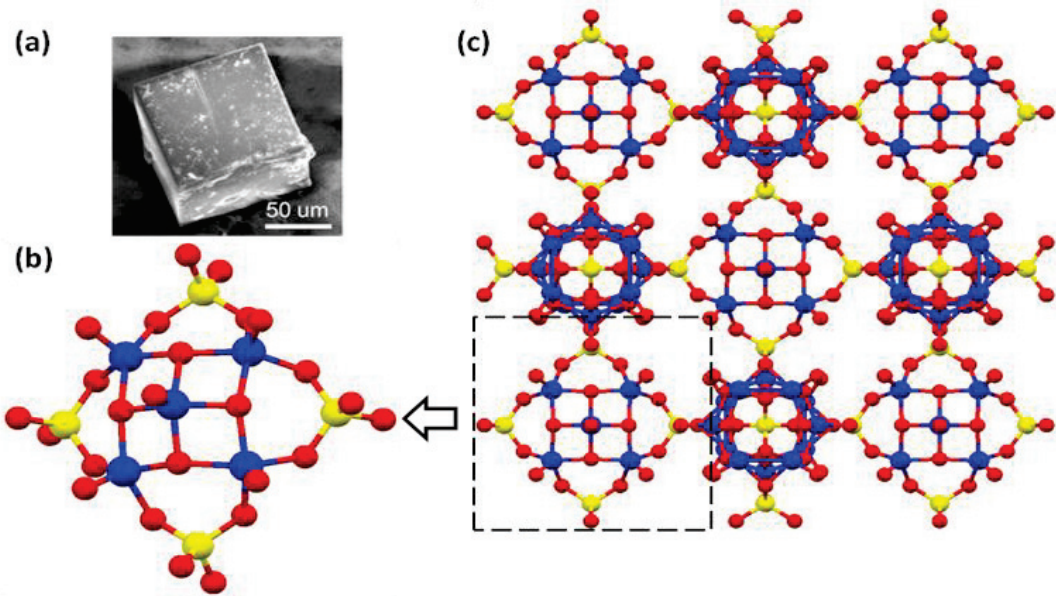

Figure 4.1: (a) Scanning electron micrograph of (1), scale bar 50 µm. (b) Half pseudo sphere unit in the crystal structure of (1). (c) Crystal structure of (1) down *a*. Yellow balls are As. Blue balls are V. Red balls are O.

4.2 Methods and experimental

We measure the electrical conductivity (σ) as a function of temperature on the as-synthesized single crystals, single crystals after heat treatment, and various ion-exchanged crystals, to probe the electrical properties of compounds (1) and (2) and their various ion-exchanged forms. We obtain the total conductivity (σ_{tot}) due to the framework plus the extra-framework constituents. The electronic conductivity (σ_{el}) is due to the empty framework (*i.e.* absence of extra-framework constituents), and the ionic conductivity (σ_{ion}) is attributed to the extra-framework constituents, organic and inorganic. The ionic conductivity (σ_{ion}) is obtained by subtraction, $\sigma_{ion} = \sigma_{tot} - \sigma_{el}$.

The measurement of empty framework provides the electronic conductivity (σ_{el}) of the material. We obtained the empty frameworks of both compounds (1) and (2) by a heat treatment. From the thermogravimetric analysis of the as-synthesized compound (1) [93], the organic extra-frame constituents located within the pores of the framework could be expelled by heating to yield an empty framework with void pores. The thermogravimetric analysis result as shown in Fig. 4.2 indicates three steps of weight loss. The first weight loss starts around 313 K is attributed to the loosely held water. We observe a 10% weight loss by the time 370 K is reached. The second weight loss at around 470 K is attributed to the tightly held water. The organic extra-framework constituents are expelled at around 600 K as observed from the third weight loss step. By 700 K, the pores within the framework are essentially empty. The heat treatment was performed by heating the as-synthesized single crystals with organic extra-framework constituents in a quartz tube furnace under a flow of N_2 gas, and then the empty framework was kept under an overpressure of N_2 until measurement to avoid water reoccupying of the framework pores. For compound (1), we tried two routes: (a) contacting the as-synthesized crystals with the PELCO

high performance silver paste and obtaining their room temperature and ambient pressure conductivity value, subjecting them to the heat treatment up to 700 K for two hours, and obtaining the conductivity value again; and (b) subjecting loose crystals to the heat treatment the same as route (a) and afterwards obtaining their conductivity values. While the first route provided a direct before and after comparison, more crystals cracked during the heating if they were initially contacted then not. For the second route, and as a reference, we would measure the room temperature and ambient pressure conductivity of a crystal from the same reaction. The conductivity values of the empty framework obtained from the two routes did not differ significantly. For compound (2), heat treatment was performed only on the silver paste contacted single crystals. Two electrodes were first fabricated on the as-synthesized single crystals with the PELCO high performance silver paste and the room temperature DC conductivity at ambient pressure was obtained. Then the samples were heated up to 570 K for 1/2 hours and 720 K for 1/2 hours respectively. After 720 K, disintegration of the crystals was observed. More silver paste was added to the contacts of the samples after 570 K heat treatment to avoid the situation of contacts becoming loose. After the heat treatment of both 570 K and 720 K, no current could be detected in the conductivity measurement indicating the empty framework of compound (2) as essentially electrically insulating.

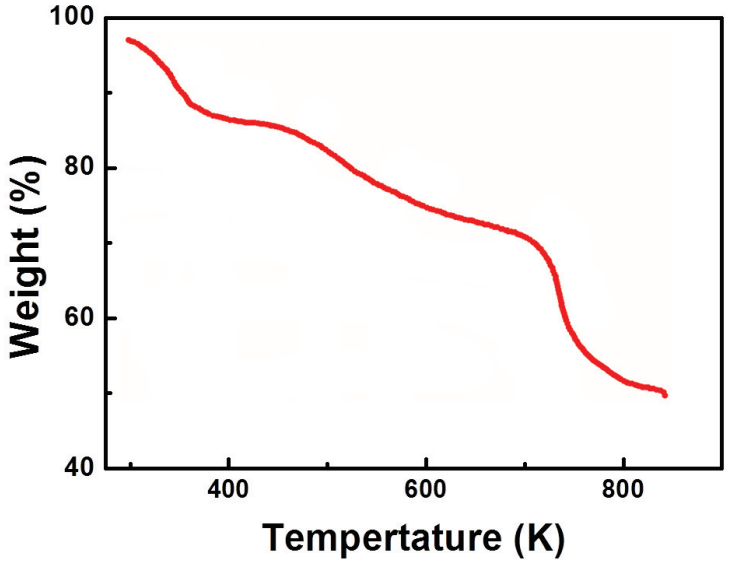

Figure 4.2: The thermogravimetric analysis result of compound (1) in the temperature range from 293 K to 973 K.

We obtain the ionic conductivity (σ_{ion}) by subtracting the electronic conductivity from the total conductivity (σ_{tot}). The total conductivity for organic ions is obtained directly on the as-synthesized crystals. We performed various ion exchange processes with alkali ions on the as-synthesized crystals. As described above, the mobility of the extra-framework constituents side the porous structure makes the ion exchange feasible. To obtain the framework with compounds (1) and (2), all at room temperature. After the crystals were soaked for several days, they were filtered off and washed twice with DI water. For compound (1), we started with the as-synthesized framework and exchanged the organic cation with Li, Na, K and Rb ions from solutions of their chloride salts. The concentrations of the alkali halides were around 3 M (LiCl, 3.1 M, NaCl and KCl, 3.2 M, and RbCl, 2.2 M). Reagent grade LiCl, NaCl, KCl and RbCl

crystals from Spectrum Chemical Mfg. Corp. were mixed with DI water respectively to prepare the solution for the ion exchange experiments. Our attempts in exchanging the organic cation with Rb^+ always resulted in the disintegration of the crystals. For (2), the organic extra-framework constituents were exchanged with Na^+ and K^+ successfully (salt solution concentrations same as those used for (1)). For the electrical measurements on the ion-exchanged frameworks, two methods were used. In the first case, as-synthesized materials were contacted, measured, and then soaked in an alkali halide solution (with the contacts), and re-measured after the ion exchange process. This route provided a direct before and after comparison. In the second and preferred case, crystals were chosen from a reaction, soaked in the desired alkali halide solution, and then contacted and measured. A crystal of the as-synthesized material from the same reaction was also measured, providing a comparison point.

Electrical measurements were performed on the individual crystals as-synthesized, after heat treatment and after ion exchange processes of both (1) and (2). Single crystals down to ~50 μm were contacted on a side by H20E Epotek silver conductive epoxy or PELCO high performance silver paste. The contacts were cured at 318 K for a few hours, and connected to the measurement holder by silver or gold wires. Figure 4.1(a) shows a representative crystal of compound (1), and while crystals of various sizes were isolated, we deliberately chose the smaller crystals to minimize crystal imperfections and to facilitate complete ion exchange for reliable comparison of electrical transport on the same crystal. While the majority of the measurements were performed in a 2-point geometry, we also performed 4-point measurements on the as-synthesized compounds (1) and (2), and compared the conductivity values between the 2- and 4-point measurements. The differences were not significant, and for the comparative

measurements we present under sections 4.3, 4.4 and 4.5, mainly 2-point contact geometries were employed.

DC measurements were obtained using a combination of a Keithley 2400 source meter, a Keithley 2000 multimeter and an SRS SR570 low-noise current amplifier. The voltage sweep was provided by Keithley 2400 source meter, and we obtained the current value by the Keithley 2000 multimeter and the SRS SR570 low-noise current amplifier. Conductivity values were calculated from the measured resistance by the method from H. C. Montgomery (detailed description in Chapter 2) [44]. The room temperature DC conductivity at ambient pressure measured for an as-synthesized cube of compound (1) with 50 μm edge is 3×10^{-8} Ω^{-1} cm^{-1}. AC measurements are performed by phase sensitive detection using lock-in techniques. Typically the in-phase and out-of-phase AC response currents under applied AC voltage were measured, allowing for the establishment of complex dielectric functions and complex impedance plots [45, 46, 95, 96]. Complex impedance measurements on contacted single crystal were performed using an SRS SR830 DSP lock-in amplifier, and Cole-Cole plots obtained. Details of the measurement method are described in Chapter 2.

Variable temperature data from both DC and AC measurements were obtained on two measurement systems, which were a commercial ColdEdge open cycle CoolTran system and home-built quartz tube variable temperature system (detailed description in Chapter 2). A number of identical measurements were obtained in both systems, and values of the calculated conductivities compared. Representative data are plotted in Figs. 4.3, 4.4 and 4.5.

4.3 Variable temperature DC conductivity of oxo-vanadium arsenate

The variable temperature DC conductivity measurement for compound (1) was performed in the

ColdEdge open cycle CoolTran system. Samples contacted with PELCO high performance silver paste on a 5 x 5 x 0.5 mm, R plane Al_2O_3-sapphire wafer from MTI Corporation were cured at 318 K for 4.5 hours and then connected to the sample holder with silver wire. While curing the contacts occurred at roughly the same temperature as the beginning of the initial water loss from the framework as observed from the thermogravimetric analysis result in Fig. 4.2, the samples were then in ambient atmosphere during the rest of the contacting and wiring process. So the contribution to the conductivity from the loosely held water in the pores cannot be ignored. We probed this contribution by the following comparative measurement. Room temperature conductivity values were obtained for contacted crystals in the Cold Edge unit first at atmospheric pressure and then the chamber was evacuated to a base pressure of 10^{-6} Torr for 30 min (at room temperature). The surface water and loosely held water in the pores were expelled, and the conductivity values were obtained again. We observed the conductivity decrease due to the loss of water from within the pores and surface water for all the samples. The after vacuum conductivity value for the empty framework samples and the as-synthesized samples were about 100 times smaller than before vacuum, while the after vacuum conductivity value for Li, Na and K ions exchanged samples were about 1000 times smaller. Then the samples, without surface water and loosely held water, were heated to 690 K in increments of 15 K and a wait time of 15 min between increments. The various ionic and electronic conductivities were measured following the same manner allowing for comparisons. For each type, several similar measurements were obtained. The representative conductivity data were plotted in Fig. 4.3 which shows the total conductivity of the vanadium arsenate framework (denoted by the symbol star) as well as all the various electronic and ionic conductivities (organoammonium, Li^+, Na^+, and K^+). The variable temperature data of the empty framework samples after heat treatment indicates

semiconducting behavior, with an activation energy of around 0.75 eV in the temperature range 400-667 K. Fitting the framework data to standard expressions for Mott variable range hopping in one-, two- or three-dimensions [97-99], or to models using activation across an energy gap [100], does not appear to account for the electron dynamics within the framework. Various effective dimensionalities were considered for the framework electrons [27].

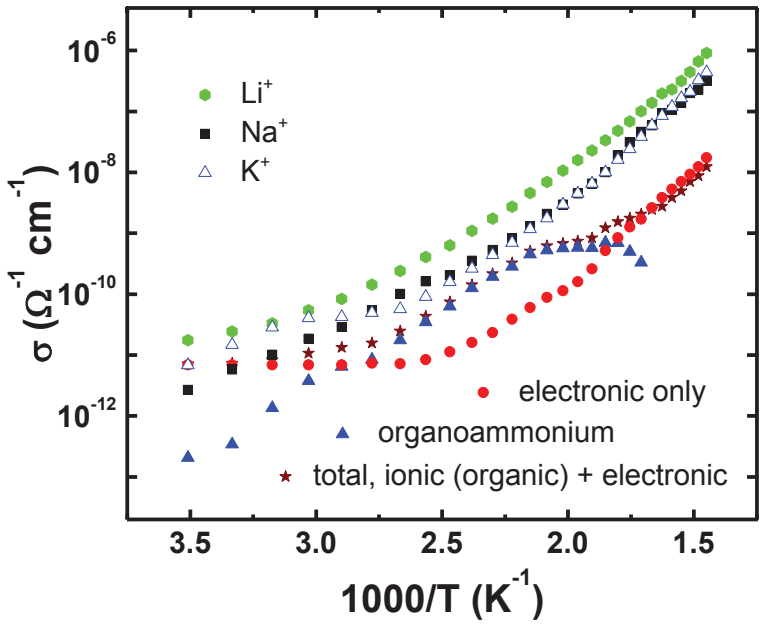

Figure 4.3: Variable temperature conductivity of (1) and ion-exchanged (1). The comparative plot highlights the electronic (circle) contribution to the total conductivity (star). The temperature range is 285-690 K.

The ionic conductivity obtained by subtracting the electronic conductivity from the total conductivity could be expressed by equation $\sigma = nq\mu$, where n is density, q is charge and μ is mobility of carriers. The density and mobility are considered with thermal activated behavior, n

as $e[-E_1/k_BT]$ and μ as $e[-E_2/k_BT]$, such that $n\mu$ varies as $e[-(E_1 + E_2)/k_BT]$ as a function of temperature. $(E_1 + E_2)$ could be extracted from the measured conductivities, and both the framework electron density and the mobility of ions with the framework pores thus the conductivities increase as the temperature increases. Concurrently, the de-trapping and subsequent mobility of the ions may be influenced by the increasing electron density, as temperature increases. The free and mobile framework electrons may screen the potential traps holding the ions in the pores of the framework. The ionic conductivity in compound (1), which is influenced by the electronic conductivity, cannot be fitted to a simple Arrhenius-activated model of ionic transport [90, 91, 101, 102] in the temperature range 285-690 K. Yet, the data indicate the occurrence of channeling of ions through a sublattice occurs, through a mechanism that at least includes phonon-assisted hopping [103, 104]. The ionic conduction in compound (1) could be elucidated by the attachment sites within the vanadium arsenate framework, and the interaction between ionic degrees of freedom of the extra-framework constituents and the carriers in the framework [103, 104]. The trace with the inorganic cation exchanged framework of compound (1) shows a slightly stronger than exponential increase of the conductivity as a function of temperature as observed in Fig. 4.3. The activation energies of the ionic conductivities of various alkali cations were extracted over the same temperature region ~360-667 K, and the representative values were 0.59 eV for Li^+, 0.55 for Na^+, and 0.65 for K^+. In the case of the organoammonium cation, as shown in Fig. 4.3, the increase of the organoammonium conductivity levels off and then decreases around 560 K, attributed to the expelling of the organoammonium cations. The trend of organoammonium conductivity as a function of time is in agreement with the total conductivity trace (symbol star), which shows a slight decrease but then an increase because of the influence of the increasing contribution of the

framework electronic conductivity. To obtain the activation energy before the organoammonium cations start to be expelled, the representative value of 0.57 eV for the activation energy was evaluated with an upper temperature limit of 560 K. The activation energies of the ionic conductivities of different ions have been proved to be correlated with the ion size and type, and thus their relative electrostatic, covalent and polarizability effects, and this work is in progress [105-108].

4.4 Variable temperature DC conductivity of oxo-vanadium phosphate

We performed the DC conductivity measurement on the structurally similar vanadium phosphate material, compound (2). The Na^+ and K^+ exchanged compound (2) were prepared from the ion exchange processes as described at section 4.2. The time we soaked the as-synthesized crystal into the NaCl and KCl aqueous solutions respectively is about 4 days. The samples for electrical measurement were fabricated by contacting the as-synthesized and Na^+ and K^+ exchanged individual crystals with H20E Epotek silver conductive epoxy and cured at 318 K for 12 hours. Then the samples were contacted to the dip header with gold wire. The conductivity measurements were performed at the quartz tube system at ambient pressure, under a flow of N_2 gas, with an initial wait period of around 30 min. The variation of the conductivity is shown in Fig. 4.4. Comparing the values of the conductivity before and after the wait period under the flow of gas of all the three traces, we observe a decrease, attributed to loss of water from the crystal. The variable temperature conductivity were obtained with the same temperature increment (10 K) and waiting time (15 min). The room temperature measured conductivity of the empty framework from heat treatment is too small compared to the room temperature conductivity of the as-synthesized compound indicating that the vanadium phosphate framework does not support electronic conduction. Thus, the total conductivity plotted in Fig. 4.4 in this case is also

the ionic conductivity. Fitting the conductivity data in the range 310-475 K, we observe an exponential increase of the ionic conductivity, distinct from the slightly stronger than exponential increase observed for compound (1) in Fig. 4.3. The framework of compound (2) compared to that of compound (1) does not show electronic conductivity, and thus in (2) we do not have interactions between framework carriers and the ionic conductivity of the extra-framework constituents.

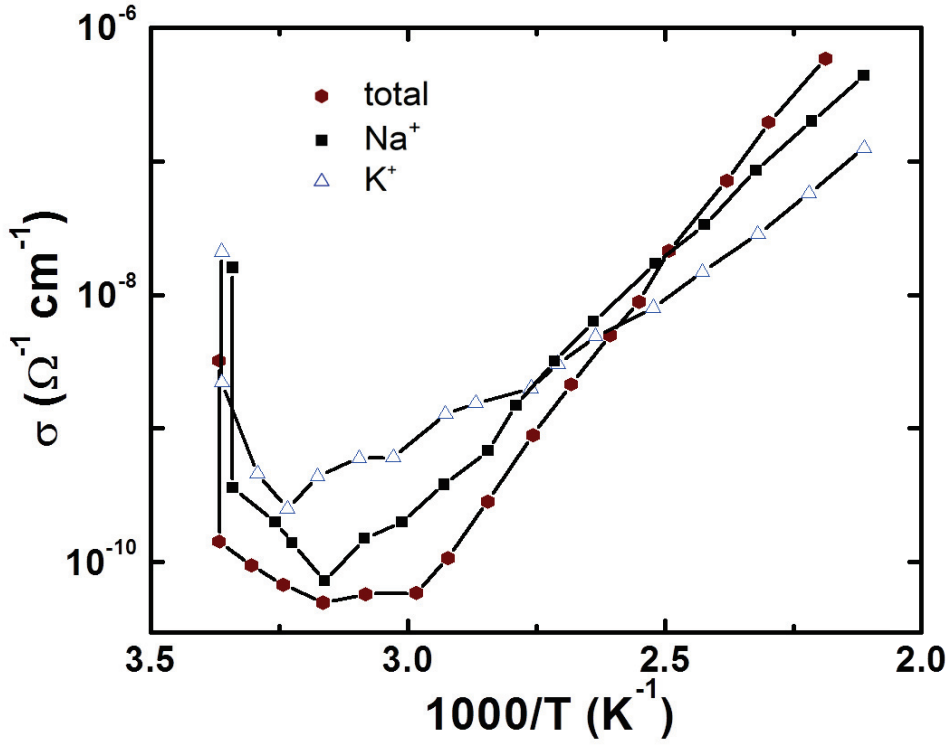

Figure 4.4: Variable temperature conductivity of (2) and ion-exchanged (2). The temperature range is 310-475 K.

4.5 Variable temperature AC electrical characterization of oxo-vanadium phosphate

We performed AC studies on compound (1) with various cations to provide complementary information to the DC measurements. The variable temperature AC studies were performed on same sort of samples as used in section 4.3 in the ColdEdge open cycle CoolTran system. The chamber was evacuated for 1 hour to 10^{-6} Torr, and the samples were heated to 490 K first. Then Cole-Cole plots were obtained at temperatures 490 K, 600K, and 700 K. The AC measurement took about 40 min for each temperature value with the waiting time between each value of about 30 min. Room temperature AC information was also obtained by connecting the sample directly to an SRS SR830 DSP lock-in amplifier. In our contacted samples, we note that the surface area covered by the contacts compared to the total surface area of the single crystal is not negligible, and thus the influence of the contacts is an open question. The contacts behave similar to contacts on semiconducting materials [100], partially non-ohmic, especially at low frequencies and ambient temperatures. Yet, the measurements described by Fig. 4.5 are performed on roughly same sized single crystals of compound (1) with similarly sized contacts, allowing us to extract comparative information. We applied AC voltage with frequency sweep from low to high. The imaginary (Z'') and real (Z') part of the impedance could be extracted from the measured AC response current, and Cole-Cole plots plotted [45, 46].

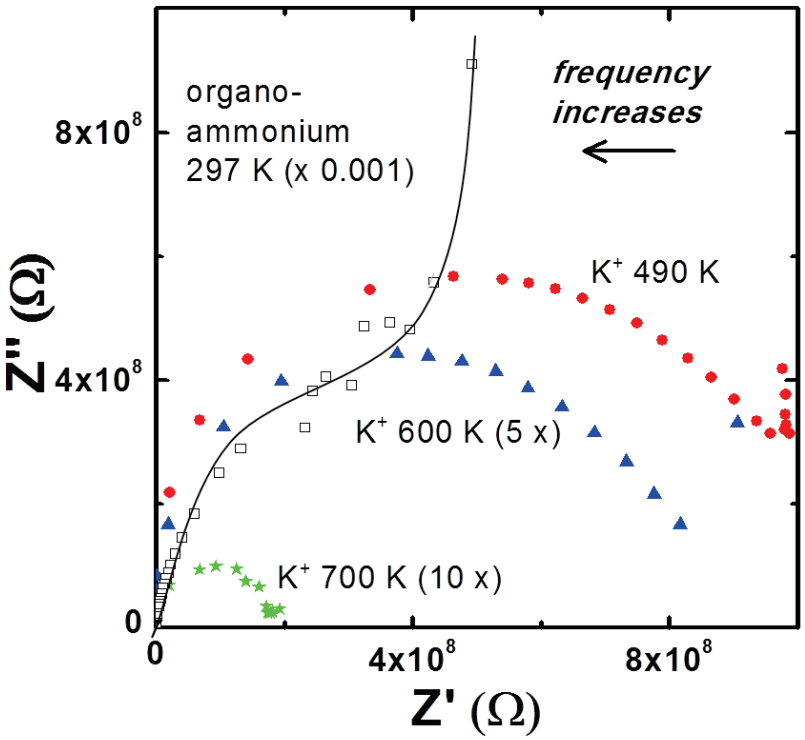

Figure 4.5: Plots of impedance measurement on (1) and ion-exchanged (1) at various temperatures. For the organoammonium trace at 297 K, a line is drawn through the experimental points to guide the eye. As indicated, the frequency increases from right to left in the figure. To better represent the data, some of the traces are multiplied by an appropriate factor.

In Fig. 4.5, we exhibit the Cole-Cole plots for the K^+ exchanged compound (1) at different temperatures, and the as-synthesized compound (1) with organoammonium cation at room temperature for comparison. The resistance of each trace could be measured as the diameter of the semi-circle depicted. The resistances obtained at 490, 600 and 700 K for the K^+ exchanged compound (1) decrease as we expected and are in agreement with the DC measurement result. More pronouncedly formed semi-circle is observed at higher temperature. A deviation from the

circular trace at very low frequencies is observed indicates an effective increase in the complex part of the impedance at low frequency. We attribute the deviation to the contact resistance. Similar trend was observed for the as-synthesized compound (1) with organoammonium cation. We obtained data at 490 and 600 K for the organoammonium sample, which are not shown because of the uncertainty from the loss of organic ions during the sample heating phase. The 297 K Cole-Cole plot for the K^+ material was less conclusive, and thus not included. Instead, we show the room temperature impedance trace of as-synthesized organoammonium material with more pronounced deviation of the semi-circle.

An equivalent circuit model provides an interpretation of the Cole-Cole plots as shown in Fig. 4.6. We consider a capacitor and resistor in parallel for the extra framework ions and the framework. The charge separation of extra framework ions and the electrons in the framework formed the capacitance (C_{EDL}), and electrochemical leakage -*e.g.* charge transfer between the ions and the framework, and diffusion of ions within the pores, constitutes the parallel resistance ($R_{parallel}$) [109]. The ionic, electronic and contact resistances in series with the parallel circuits of C_{EDL} and $R_{parallel}$ construct a resistance (R_{series}). As the temperature is increased, the contact resistance as well as the ionic and electronic resistances decrease as expected (and shown in Fig. 4.3), so do the contribution of the series resistance R_{series} to the measurement. But, even at 700 K for the K^+ exchanged (1), there is a slight deviation at low frequency due to R_{series}. Nevertheless, the conductivity values could be extracted from the resistance measured as the diameter of the semi-circle taking account of the size of the crystals used. And the conductivities obtained overlap what we depicted in Fig. 4.3, thus provide complement for the DC measurements and add to our understanding of electrical properties of zeolite-like mixed conductors.

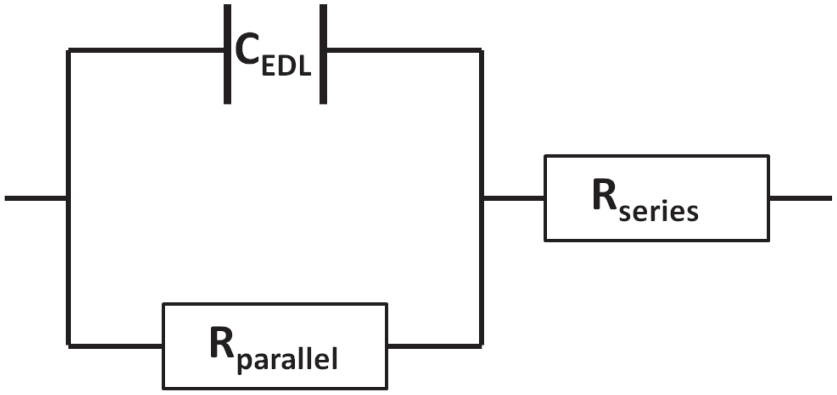

Figure 4.6: The equivalent circuit model corresponding to the Cole-Cole plot as shown in Fig. 4.5. C_{EDL} is the capacitance formed at the electrical double-layer; $R_{parellel}$ is the resistance from electrochemical leakage; R_{series} is ionic, electronic and contact resistance in series.

4.6 Conclusion

We compare the electrical characteristics of two structurally similar but compositionally different zeolite-like frameworks as a function of temperature and various extra-framework constituents. The oxo-vanadium arsenate framework is a mixed conductor with both electronic conduction from the framework and ionic conduction from the extra-framework constituents, and where these two interact with each other. We assume the electronic conduction influences the ionic conduction as the temperature increases by assisting the de-trapping of the ions in the pores of the framework. We observe a slightly stronger than exponential increase of the ionic conductivity as a function of temperature. Yet in the oxo-vanadium phosphate material, only ionic conductivity is detected. Understanding the conductivity pathways in zeolite-like mixed conductors, electronic and ionic conductivities and their interplay, impacts fundamental endeavors as well as applications.

Chapter 5 Electrical properties and crystal structures of strontium manganese vanadate and arsenate frameworks

An increasing emphasis is placed on transition metal oxides with a variety of structures and properties [110-112], which is widely used in various fields. For example, it can be used in energy storage as the electrode material for supercapacitors [113-115] and rechargeable batteries [116-118]. Manganese compounds catch our attention because of the interesting structural and electrical properties. They have the tendency to form open frameworks [28-30, 118] and provide mixed valence which is critical for the electron transfer and energy storage [118-121]. In this chapter, we report two transition metal oxide materials, a strontium manganese vanadate, compound (1), and a strontium manganese arsenate, compound (2), both prepared by hydrothermal method. The morphology of a representative crystal of compound (1) is shown in Fig. 5.1. It is a rectangular plate-like crystal of about 200 μm wide and 15 μm thick and brown in color. A structural change of compound (1) caused by high temperature is deduced by thermogravimetric analysis (TGA). We present the comparative study of the structure of compound (1) before and after the structural change and compound (2) by single crystal x-ray diffraction (XRD) analysis. The structural change of compound (1) is due to the loss of water from the μ_3-OH_2 and μ_4-OH sites. After the structural change, the structure of compound (1) is similar to that of compound (2). We also measured the conductivity of compound (1) as a function of temperature and crystal direction by employing a 4-point conductivity measurement in a single crystal. An anisotropic protonic conductivity is observed which vanishes after the structural change.

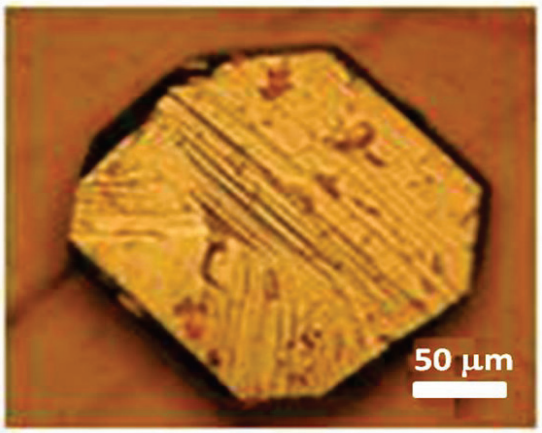

Figure 5.1: Optical micrograph of the rectangular single crystal of (1) with side length ~200µm and thickness ~15µm.

5.1 Thermogravimetric analysis and UV-VIS adsorption edge spectrum analysis

We studied the thermal stability of the hydrothermally synthesized compound (1) by thermogravimetric analysis (TGA). The as-synthesized single crystals were picked out from the reaction, washed with DI water, dried and ground in a mortar with a pestle to uniform powder. TGA experiment was performed on the powdered sample with a Perkin Elmer TGA7 thermogravimetric analyzer in a nitrogen atmosphere. The mass of the power samples was monitored as a function of temperature from 296 K to 872 K at a heat rate of 8~9 K min^{-1}. As observed in the plot in Fig. 5.2, the sample is very stable until around 675 K. Then a weight loss of about 6% is observed from 675 K to 775 K, which is assumed to be attributed to the expelling of hydrogen and oxygen atoms as water from the crystal structure and indicates a structural change in the strontium manganese vanadate framework. This structural change will be further investigated by single crystal x-ray diffraction in section 5.2. Above 775 K, the new structure after the structural change is stable up to 872 K.

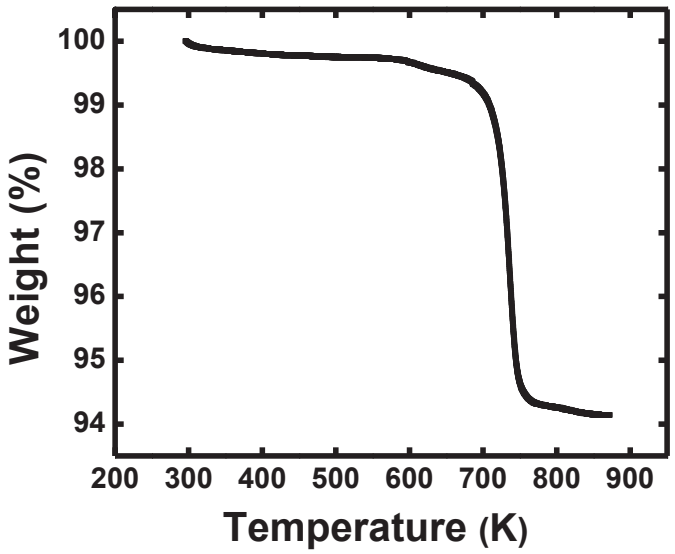

Figure 5.2: TGA result of (1) run at 8~9 K min^{-1} in the temperature range 296 K to 872 K.

The ultraviolet-visible (UV-Vis) diffuse reflectance measurement was performed on the powder sample of compound (1) following the same procedure as the TGA experiment, with the Evolution 300 UV-Vis spectrophotometer and the Praying Mantis diffuse reflectance accessory (DRA) at room temperature. The optical bandgap was extrapolated from the UV-VIS adsorption edge spectrum to be 1.21 eV. It is similar to the bandgap of GaAs, which is 1.43 eV.

5.2 Single crystal x-ray diffraction analysis

As discussed in section 5.1, a structural change of compound (1) occurs in the temperature range 675 K to 775 K as deduced from the TGA result. In this section, we compare the crystal structure of compound (1) before and after a heat treatment by single crystal XRD analysis to explore this structural change. Single crystal samples were picked from reaction, washed with DI water and dried. And single crystal XRD experiment was performed on one of them at 100 K. Then the

crystals were heated up slowly to 800 K, and stayed at 800 K for 1.5 hours in a quartz tube furnace under a flow of N_2 gas. After cooled down, the crystals were still brown and without any obviously difference observed under microscope. Single crystal XRD measurement was performed again at 295 K on one of the single crystals after the heat treatment.

The crystal structure of compound (1) before the heat treatment is best solved in the monoclinic space group C2/m with an R value 2.11%, and the lattice parameters are a = 9.3196(19) Å, b = 6.4409(13) Å, c = 7.6405(15) Å and β = 117.81(3)°. The crystal data and structure refinement are shown in Table 5.1. The fractional atomic coordinates, bond lengths and angles are shown in Tables 5.2, 5.3, 5.4 and 5.5 respectively. The crystal structure down a is shown in Fig. 5.3(a) and the molecular formula is $SrMn_2(VO_4)_2(\mu_3\text{-}OH)(\mu_4\text{-}OH_2)$. The octahedral manganese units connect to each other via Mn-O bonds and form $Mn<^{O}_{O}>Mn$ chains in the b direction as shown in Fig. 5.3(d). A geometrical distortion is observed in the MnO_6 octahedra. Among the six Mn-O bonds, the average bond length of the four shorter Mn-O bond is about 2.05 Å which is similar to the value reported in reference [122], where the average Mn-O bond length is 2.01 Å for Mn^{3+} ion, while the two longer bonds are around 2.19 Å indicating the elongation Jahn-Teller distortion. The Jahn-Teller distortion removes the degeneracy of electronic state and lowers the overall energy of the structure [123]. The $Mn<^{O}_{O}>Mn$ chains and vanadium tetrahedral units form manganese vanadate layers. And the layers in turn are connected to each other through strontium sites along the c direction to form a 3-dimensional structure. The distance between two layers is 3.13 Å. According to the bond valence sum analysis [124], the oxidation state of vanadium is +5 and that of manganese is + 2.5. The +2.5 oxidation state of manganese is due to the simultaneous presence of Mn^{+2} and Mn^{+3} in the framework. Based on these oxidation state assignments, 3 additional hydrogen sites are assigned to balance the charge of the framework. The hydrogen sites (gray balls

in Fig. 5.3(d)) are attached to the oxygen sites in the Mn<$^{O}_{O}$>Mn units forming a chain, which are the only chemically reasonable locations for hydrogen, to form μ_3-OH and μ_4-OH_2 respectively, and refined independently with the restraint that O-H bonds equal to 0.83 Å. The distance between oxygen sites in μ_3-OH and μ_4-OH_2 near each other is around 2.60 Å. And a hydrogen atom trapped between 2 oxygen sites has two bonds, one short and strong bond and one long and weak bond, in the shape of O-H$^{\cdots}$O, as shown in Table 5.5. Hydrogen may migrate from μ_3-OH_2 to μ_4-OH to induce protonic conduction [125].

The crystal structure of compound (1) after the heat treatment at 800 K is solved in the monoclinic space group $P2_1/m$ with an R value 13.00%. The structure down *a* is shown in Fig. 5.3(b). The lattice parameters are *a* = 9.2830(7) Å, *b* = 6.0268(9) Å, *c* =7.6676(13) Å, and β = 118.765(11)°, and the molecular formula is $SrMn_2(VO_4)_2O_{0.5}$. The crystal data and structure refinement are shown in Table 5.6. The fractional atomic coordinates, bond lengths and angles are shown in Tables 5.7, 5.8 and 5.9 respectively. The space group change from C2/m to $P2_1/m$ indicates the decrease in symmetry. The unit cell parameters are similar to that of the crystal structure before the heat treatment, except the *b* value which is decreased from 6.4409(13) Å to 6.0268(9) Å. Based on the molecular formula after the heat treatment, the structure loses all the hydrogens and some of the oxygen. We assume the following chemical reaction occurs during the heat treatment:

$$SrMn_2(VO_4)_2(\mu_3\text{-}OH)(\mu_4\text{-}OH_2) \rightarrow SrMn_2(VO_4)_2O_{0.5} + 1.5H_2O \qquad (5.1)$$

The distance between two manganese atoms in a Mn<$^{O}_{O}$>Mn chain decreases from 3.22 Å to 3.01 Å which contributes to the *b* value decrease. Every two Mn<$^{O}_{O}$>Mn chains connected to each other through tetrahedral vanadium in the Sr-Mn-V-O framework are divided to one chain which remains unchanged after the heat treatment, chain (1), and the other chain which is disordered after

the heat treatment, chain (2). As shown in Fig. 5.3(e), the oxygen atoms lost during the heat treatment are only from chain (2). The following comparison of chain (2) before and after the heat treatment (Figs. 5.3(d) and 5.3(e)) aids in the elucidation of the structural change. In chain (2) before the heat treatment, there are two types of oxygen atoms. One is attached to hydrogen, and the other is attached to the vanadium sites. After the heat treatment, the oxygen atoms attached to hydrogen are expelled, and the chain is broken. The manganese atoms in this broken chain move to the sites of the expelled oxygen, while the remaining oxygen atoms are still connected to vanadium sites and the tetrahedral vanadium is unaffected. Thus we conclude that the structural change is mainly influencing chain (2) during the heat treatment.

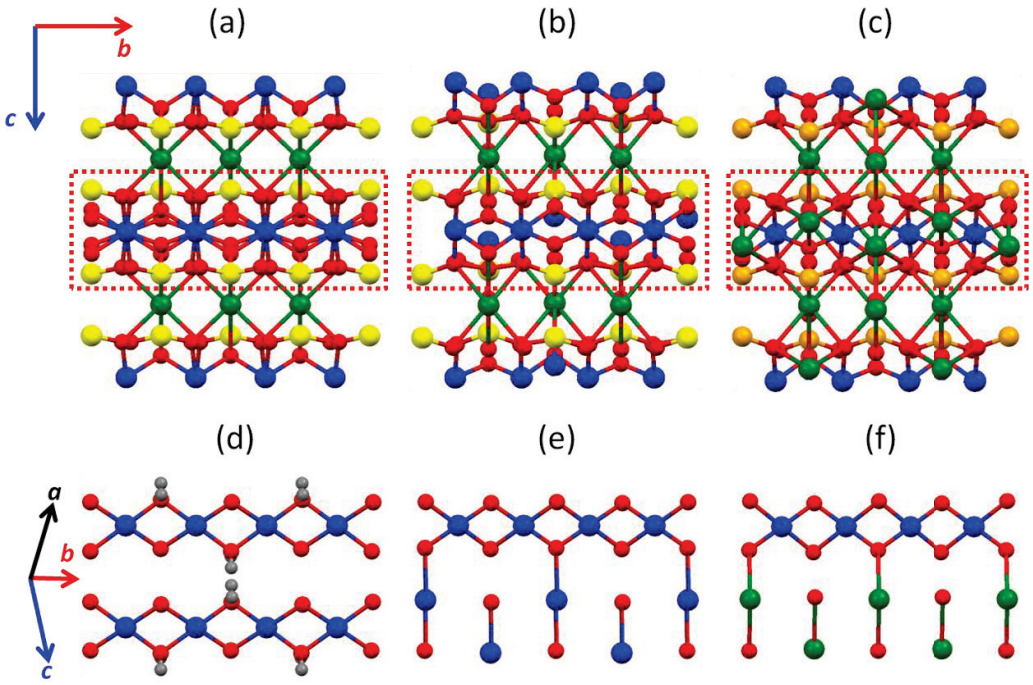

Figure 5.3: Crystal structure down *a* of (1) before the heat treatment (a), after the heat treatment (b) and (2) (c). The Mn$<^{O}_{O}>$Mn chains of (2) before the heat treatment (d), after the heat treatment (e), and (2) (f). Yellow balls are V. Orange balls are As. Blue balls are Mn. Green balls are Sr. Red balls are O. Gray balls are H.

Compound (2) with similar crystal structure was synthesized and studied for comparison. Single crystal XRD diffraction on the hydrothermal synthesized compound (2) was obtained at 295 K. The crystal structure is solved with an R value of 7.44%, and the structure down *a* is depicted in Fig. 5.3(c). The lattice parameters obtained are $a = 9.2430(6)$ Å, $b = 6.0401(2)$ Å, $c = 7.5923(5)$ Å, and $\beta = 118.796(9)°$, in the monoclinic space group $P2_1/m$, the same space group in which we obtain the best solution for compound (1) after the heat treatment. The crystal data and structure refinement are shown in Table 5.10. The fractional atomic coordinates, bond lengths and angles are shown in Tables 5.11, 5.12 and 5.13 respectively. From the molecular formula, ($Sr_2Mn(AsO_4)_2O$), compound (2) has a different composition. In the structure of compound (2), tetrahedral arsenate is located at the same sites as the tetrahedral vanadate unit in compound (1) after the heat treatment. The ratio of Sr and Mn is 2:1 as the strontium takes the same manganese sites in the disordered $Mn<^{O}_{O}>Mn$ chains of the strontium manganese after the heat treatment (as shown in Figs 5.3(e) and 5.3(f)).

Table 5.1: Crystal data and structure refinement for (1) before the heat treatment

Chemical formula	$SrMn_2(VO_4)_2(\mu_3\text{-}OH)(\mu_4\text{-}OH_2)$
Formula weight	462.40
Temperature	100(2) K
Wavelength	0.71073 Å
Crystal system	Monoclinic
Space group	*C2/m*
Unit cell dimensions	a = 9.3196(19) Å
	b = 6.4409(13) Å
	c = 7.6405(15) Å
	β = 117.81(3)°
Volume	405.67(14) $Å^3$
Z	2
Density (calculated)	3.786 Mg m^{-3}
Absorption coefficient	11.816 mm^{-1}
F(000)	434
Crystal size	0.17 x 0.12 x 0.01 mm^3
Theta range for data collection	3.01-30.09°
Index ranges	-12<=h<=13, -9<=k<=6, -10<=l<=9
Reflections collected	2436
Independent reflections	637 [R(int) = 0.0275]
Completeness to theta = 30.09°	98.8 %
Absorption correction	Gaussian
Max. and min. transmission	0.885 and 0.203
Refinement method	Full-matrix least-squares on F^2
Data / restraints / parameters	637 / 2 / 48
Goodness-of-fit (S) on F^2	1.120
Final R indices [I>2sigma(I)]	R = 0.0211, wR2 = 0.0512
R indices (all data)	R = 0.0236, wR2 = 0.0523
Largest diff. peak and hole	0.705 e $Å^{-3}$and -0.545 e $Å^{-3}$

Table 5.2: Fractional atomic coordinates for (1) before the heat treatment

Element	Equivalent position			Occupancy
	x	y	z	
Sr	0.0000	0.0000	0.0000	0.250
Mn	0.2500	0.2500	0.5000	0.500
V	0.41529(7)	0.0000	0.21226(8)	0.500
O1	0.3429(3)	0.5000	0.4109(4)	0.500
O2	0.3079(3)	0.0000	0.3498(4)	0.500
O3	0.0355(2)	0.2802(3)	0.2565(2)	1.000
O4	0.2726(3)	0.0000	-0.0218(4)	0.500
H1	0.324(6)	0.5000	0.297(4)	0.500
H2	0.443(3)	0.5000	0.463(14)	0.250

Table 5.3: Bond lengths in the structure of (1) before the heat treatment

Bond	Length/ Å	Bond	Length/ Å
Sr-O2	2.867(3)	V-O3#1	1.7378(18)
Sr-O3	2.5697(16)	Mn-O1	2.0869(17)
Sr-O4	2.622(3)	Mn-O2	2.1857(17)
V-O2	1.757(3)	Mn-O3	2.006(2)
V-O4	1.658(3)		
Symmetry codes: #1 x+1/2, -y+1/2, z.			

Table 5.4: Angles in the structure of (1) before the heat treatment

Angle	Angle/ °	Angle	Angle/ °
O2-Sr-O2#2	180.00(17)	O2-V-O4	104.54(13)
O2-Sr-O3#3	64.67(5)	O3#1-V-O3#6	109.12(12)
O2-Sr-O4	58.76(8)	O3#1-V-O4	109.26(8)
O3-Sr-O3#4	90.78(7)	Mn-O1-Mn#7	100.99(11)
O3-Sr-O4	105.35(6)	Mn-O2-Mn#8	94.90(9)
O4-Sr-O4#2	180.00(10)	V-O2-Mn	131.52(5)
O1-Mn-O1#5	180.0	Mn-O2-Sr	96.01(8)
O1-Mn-O2	98.96(7)	V-O2-Sr	92.52(10)
O1-Mn-O3	90.48(9)	Mn-O3-Sr	110.92(7)
O2-Mn-O2#5	180.0	Mn-O3-V#9	122.17(9)
O2-Mn-O3	88.16(8)	Sr-O3-V#9	125.58(9)
O3-Mn-O3#5	180.0	V-O4-Sr	104.18(12)
O2-V-O3#1	112.26(7)		

Symmetry codes: #1 x+1/2, -y+1/2, z. #2 -x, -y, -z. #3 x, -y, z. #4 -x, y, -z. #5 -x+1/2, -y+1/2, -z+1. #6 x+1/2, y-1/2, z. #7 -x+1/2, y+1/2, -z+1. #8 -x+1/2, y-1/2, -z+1. #9 x-1/2, y+1/2, z.

Table 5.5: Hydrogen bonds for (1) before the heat treatment

D-H···A	Length/ Å			Angle/ °
	D-H	H···A	D···A	D-H···A
O1-H1...O4#10	0.803(19)	1.86(2)	2.648(3)	166(5)
O1-H2...O1#11	0.83(2)	1.76(2)	2.591(6)	177(10)

Symmetry codes: #10 -x+1/2, -y+1/2, -z. #11 -x+1, -y+1, -z+1.

Table 5.6: Crystal data and structure refinement for (1) after the heat treatment

Chemical formula	$SrMn_2(VO_4)_2O_{0.5}$
Formula weight	444.39
Temperature	297.7(4) K
Wavelength	0.71073 Å
Crystal system	Monoclinic
Space group	$P2_1/m$
Unit cell dimensions	a = 9.2830(7)Å
	b = 6.0268(9) Å
	c = 7.6676(13) Å
	β = 118.765(11)°
Volume	376.05(9) $Å^3$
Z	2
Density (calculated)	3.925 Mg m^{-3}
Absorption coefficient	12.729 mm^{-1}
F(000)	414
Crystal size	0.13 x 0.12 x 0.02 mm^3
Theta range for data collection	4.208-33.006°
Index ranges	-14<=h<=13, -9<=k<=8, -11<=l<=11
Reflections collected	12010
Independent reflections	1456 [R(int) = 0.1319]
Completeness to theta = 30.09°	99.7 %
Absorption correction	Gaussian
Max. and min. transmission	1.000 and 0.334
Refinement method	Full-matrix least-squares on F^2
Data / restraints / parameters	1456 / 0 / 85
Goodness-of-fit (S) on F^2	1.184
Final R indices [I>2sigma(I)]	R = 0.1300, wR2 = 0.3816
R indices (all data)	R = 0.1621, wR2 = 0.3998
Largest diff. peak and hole	6.603 e $Å^{-3}$and -2.075 e $Å^{-3}$

Table 5.7: Fractional atomic coordinates for (1) after the heat treatment

Element	Equivalent position			Occupancy
	x	y	z	
Sr	0.7391(3)	0.2500	0.0080(4)	0.500
Mn1	0.5000	0.0000	0.5000	0.500
Mn2	0.9021(3)	0.2500	0.5839(4)	0.500
V1	0.1615(5)	0.2500	0.1978(6)	0.500
V2	0.3201(5)	0.2500	0.7707(6)	0.500
O1	0.034(3)	0.2500	-0.036(4)	0.500
O2	0.044(3)	0.2500	0.306(4)	0.125
O3	0.2826(17)	0.009(2)	0.274(2)	1.000
O4	0.445(2)	0.2500	0.656(4)	0.500
O5	0.456(3)	0.2500	0.014(4)	0.500
O6	0.1948(19)	0.019(2)	0.705(2)	1.000
O7	0.574(2)	0.2500	0.405(3)	0.500
O8	0.823(7)	0.2500	0.761(13)	0.125

Table 5.8: Bond lengths in the structure of (1) after the heat treatment

Bond	Length/ Å	Bond	Length/ Å
Sr-O1#1	2.91(3)	V1-O3	1.756(14)
Sr-O2#1	2.64(3)	V2-O4	1.77(3)
Sr-O3#2	2.591(14)	V2-O5	1.68(2)
Sr-O4#3	2.76(2)	V2-O6	1.726(15)
Sr-O5#3	2.65(3)	Mn1-O3#3	1.928(14)
Sr-O6#4	2.557(15)	Mn1-O4#3	2.130(19)
Sr-O8	2.37(8)	Mn1-O7	1.937(11)
V1-O1	1.60(2)	Mn2-O8	1.82(8)
V1-O2	1.66(3)		

Symmetry codes: #1 x, y, z+1. #2 -x+2, y+1/2, -z+1. #3 x-1, y, z. #4 -x+2, -y, -z+2.

Table 5.9: Angles in the structure of (1) after the heat treatment

Angle	Angle/ °	Angle	Angle/ °
O1#1-Sr-O2#1	55.0(7)	O3-V1-O3#7	111.6(9)
O1#1-Sr-O3#2	66.7(5)	O5-V2-O	103.4(11)
O1#1-Sr-O5#3	175.1(6)	O4-V2-O6	111.7(6)
O1#1-Sr-O6#4	104.4(5)	O5-V2-O6	111.4(7)
O1#1-Sr-O8	38.6(17)	O6#7-V2-O6	107.5(10)
O2#1-Sr-O3#2	110.0(5)	O3#3-Mn1-O3#5	180.0
O2#1-Sr-O6#4	62.8(5)	O3#3-Mn1-O4#5	86.7(7)
O2#1-Sr-O8	93.6(17)	O3#5-Mn1-O4#5	93.3(7)
O2#1-Sr-O4#3	170.3(7)	O3#3-Mn1-O7	92.7(7)
O2#1-Sr-O5#3	129.9(8)	O3#5-Mn1-O7	87.3(7)
O3#2-Sr-O3#5	74.1(6)	O4#3-Mn1-O4#5	180.0
O3#2-Sr-O4#3	62.7(5)	O4#3-Mn1-O7	83.3(6)
O3#2-Sr-O5#3	109.5(5)	O4#5-Mn-O7	96.7(6)
O3#5-Sr-O6#4	103.0(5)	O7-Mn1-O7#8	180.0
O3#2-Sr-O8	42.1(8)	V1-O1-Sr#9	95.7(12)
O4#3-Sr-O5#3	59.8(8)	V1-O2-Sr#9	104.9(12)
O4#3-Sr-O3#4	123.7(5)	Mn1#10-O3-Sr#5	111.2(6)
O4#3-Sr-O8	76.7(18)	V1-O3-Sr#5	116.2(7)
O5#3-Sr-O6#4	79.3(5)	V1-O3-Mn1#10	123.2(7)
O5#3-Sr-O8	136.5(17)	V2-O4-Mn1#2	132.2(5)
O6#4-Sr-O6#6	78.7(7)	Mn1#2-O4-Mn1#10	90.1(10)
O6#4-Sr-O8	130.6(10)	V2-O4-Sr#10	95.1(10)
O1-V1-O2	104.4(13)	Mn1#2-O4-Sr#10	99.1(6)
O1-V1-O3	112.4(6)	V2-O6-Sr#4	114.4(7)
O2-V1-O3	107.8(7)	Mn1#11-O7-Mn1	102.1(8)

Symmetry codes: #1 x, y, z+1. #2 -x+2, y+1/2, -z+1. #3 x-1, y, z. #4 -x+2, -y, -z+2. #5 -x+2, -y, -z+1. #6 -x+2, y+1/2, -z+2. #7 x, -y+1/2, z. #8 -x+1, -y, -z+1. #9 x, y, z-1. #10 x+1, y, z. #11 -x+1, y+1/2, -z+1.

Table 5.10: Crystal data and structure refinement for (2)

Chemical formula	$Sr_2Mn(AsO_4)_2O$
Formula weight	492.35
Temperature	297.6(4) K
Wavelength	0.71073 Å
Crystal system	Monoclinic
Space group	$P2_1/m$
Unit cell dimensions	a = 9.2430(6) Å
	b = 6.0401(2) Å
	c = 7.5923(5) Å
	β = 118.796(9)°
Volume	371.45(4) $Å^3$
Z	2
Density (calculated)	4.402 Mg m^{-3}
Absorption coefficient	19.369 mm^{-1}
F(000)	454
Crystal size	0.10 x 0.04 x 0.01 mm^3
Theta range for data collection	4.21-35.76°
Index ranges	-14<=h<=14, -9<=k<=9, -12<=l<=12
Reflections collected	14008
Independent reflections	1813 [R(int) = 0.1008]
Completeness to theta = 30.09°	97.5 %
Absorption correction	Gaussian
Max. and min. transmission	0.907 and 0.325
Refinement method	Full-matrix least-squares on F^2
Data / restraints / parameters	1813 / 0 / 79
Goodness-of-fit (S) on F^2	1.373
Final R indices [I>2sigma(I)]	R = 0.0744, wR2 = 0.1746
R indices (all data)	R = 0.0820, wR2 = 0.1776
Largest diff. peak and hole	2.461 e $Å^{-3}$and -5.377 e $Å^{-3}$

Table 5.11: Fractional atomic coordinates for (2)

Element	Equivalent position			Occupancy
	x	y	z	
Sr1	0.24362(18)	0.2500	0.0152(2)	0.500
Sr2	0.58638(15)	0.7500	0.41708(18)	0.500
Mn	0.0000	0.5000	0.5000	0.500
As1	-0.17291(15)	0.2500	0.77970(18)	0.500
As2	0.34197(15)	0.7500	0.80226(19)	0.500
O1	-0.2956(9)	0.4754(12)	0.7097(12)	1.000
O2	-0.0390(15)	0.2500	0.0244(17)	0.500
O3	-0.0485(11)	0.2500	0.6661(14)	0.500
O4	0.2192(8)	0.5173(11)	0.7270(11)	1.000
O5	-0.0741(10)	0.7500	0.5922(12)	0.500
O6	0.4565(16)	0.7500	0.0474(15)	0.500
O7	0.4587(15)	0.7500	0.6923(18)	0.500

Table 5.12: Bond lengths in the structure of (2)

Bond	Length/ Å	Bond	Length/ Å
Sr1-O1#1	2.526(8)	Sr2-O7#6	3.107(3)
Sr1-O2#2	2.647(13)	Sr2-O7#7	2.852(11)
Sr1-O3#2	2.724(9)	As1-O1	1.686(7)
Sr1-O4#2	2.640(8)	As1-O2	1.664(11)
Sr1-O6#3	3.029(14)	As1-O3	1.739(9)
Sr1-O7#3	2.572(13)	As2-O4	1.722(7)
Sr2-O1#4	2.558(7)	As2-O6	1.639(10)
Sr2-O1#5	2.741(8)	As2-O7	1.652(11)
Sr2-O4#6	2.988(8)	Mn-O3	2.148(6)
Sr2-O5#4	2.756(8)	Mn-O4	1.930(7)
Sr2-O6	2.464(10)	Mn-O5	1.924(5)
Symmetry codes: #1 -X, 1-Y, 1-Z. #2 +X, +Y, -1+Z. #3 +X, 1+Y, 1+z. #4 1+X, +Y, 1+Z. #5 +X, 1/2-Y,+Z. #6 1-X, 2-Y, 2-Z. #7 +X,+Y,1+Z.			

Table 5.13: Angles in the structure of (2)

Angle	Angle/ °	Angle	Angle/ °
O1#1-Sr1-O1#8	82.1(3)	O7#7-Sr2-O7#6	98.4(2)
O1#1-Sr1-O2#2	77.0(2)	O1#11-As1-O1	107.7(5)
O1#1-Sr1-O3#2	120.6(2)	O1-As1-O2	112.2(3)
O1#1-Sr1-O4#2	101.0(2)	O1-As1-O3	110.4(3)
O1#1-Sr1-O6#3	107.8(2)	O2-As1-O3	103.9(5)
O1#1-Sr1-O7#3	65.6(2)	O4-As2-O4#12	109.4(5)
O2#2-Sr1-O3#2	59.8(3)	O4-As2-O6	109.8(4)
O2#2-Sr1-O4#2	109.3(2)	O4-As2-O7	108.6(4)
O2#2-Sr1-O6#3	173.4(3)	O6-As2-O7	110.6(7)
O2#2-Sr1-O7#3	129.5(3)	O3-Mn-O3#1	179.999(1)
O3#2-Sr1-O4#2	62.9(2)	O3-Mn-O4	86.6(3)
O3#2-Sr1-O6#3	113.6(3)	O3#1-Mn- O4	93.4(3)
O3#2-Sr1-O7#3	170.7(3)	O3-Mn-O5#1	82.7(3)
O4#9-Sr1-O4#2	75.4(3)	O3-Mn-O5	97.3(3)
O4#2-Sr1-O6#3	65.8(2)	O4-Mn-O4#1	179.999(1)
O4#2-Sr1- O7#3	110.1(2)	O4-Mn-O5	92.1(3)
O6#3-Sr1- O7#3	57.1(3)	O4#1-Mn- O5	87.9(3)
O1#10-Sr2-O1#5	85.3(2)	O5-Mn-O5#1	179.999(1)
O1#10-Sr2-O4#6	83.5(2)	As1-O1-Sr1#1	116.0(4)
O1#5-Sr2-O5#10	149.94(14)	As1-O1-Sr2#5	96.1(3)
O1#5-Sr2- O3	75.1(3)	Sr1#1-O1-Sr2#5	112.4(3)
O1#5-Sr2-O7#7	64.9(3)	As1-O2-Sr1#7	100.5(5)
O4#6-Sr2- O5#10	55.30(19)	As1-O3-Sr1#7	95.7(4)
O4#6-Sr2- O6	68.4(3)	As1-O3-Mn	131.8(2)
O4#6-Sr2-O7#6	53.4(3)	Mn-O3-Sr1#7	100.5(3)
O5#10-Sr2- O6	111.5(4)	Mn-O3-Mn#8	89.3(3)
O5#10-Sr2-O7#7	115.1(3)	As2-O4-Sr1#7	116.4(3)
O6-Sr2-O7#7	133.5(4)	As2-O4-Mn	125.5(4)

Angle	Angle/ °	Angle	Angle/ °
As2-O4-Sr2#6	98.4(3)	Sr2-O6-Sr1#3	101.4(4)
Sr1#7-O4-Sr2#6	98.4(2)	As2-O7-Sr1#3	104.5(6)
Mn-O4-Sr1#7	109.9(3)	As2-O7-Sr2#6	95.7(2)
Mn-O4-Sr2#3	101.6(3)	Sr1#3-O7-Sr2#6	100.4(2)
As2-O6-Sr1#3	87.8(5)	Sr2#6-O7-Sr2#3	152.9(4)
As2-O6-Sr2	170.8(8)		
Symmetry codes: Symmetry codes: #1 -X, 1-Y, 1-Z. #2 +X, +Y, -1+Z. #3 +X, 1+Y, 1+z. #5 +X, 1/2-Y,+Z. #6 1-X, 2-Y, 2-Z. #7 +X,+Y,1+Z. #8 -X, -1/2+Y, 1-Z. #9 +X, 1/2-Y, -1+Z. #10 1+X, +Y, 1+Z. #11 -X, 1-Y, 2-Z. #12 1-X, 1-Y, 2-Z.			

5.3 Variable temperature electrical characterization

Taking account of the layered structure of compound (1), we made the hypothesis that the electrical conductivity is different along different crystallographic directions [126-129]. Through x-ray diffraction, we determined that the manganese vanadate planes are parallel to the surface of the crystal (optical image of a crystal in Fig. 5.1, and ball and stick model of manganese vanadate planes in Fig. 5.3(a)). We studied the electrical conductivity parallel and perpendicular to the layers plane by measuring the resistances parallel and perpendicular to the plate surface of the crystal sample. Conductivity measurements, using a 4-point method, were adopted to exclude the contact resistance and obtain the conductivity as a function of crystal direction. We fabricated four contacts on a single crystal with H20E Epotek silver conductive epoxy [44, 126]. Current-voltage (I-V) measurements were performed from 295 K to 428 K in the ColdEdge open cycle CoolTran system (see Chapter 2), with a temperature increment of 25 K and a wait time of 30 min between increments. Variable current was applied through two of the four contacts and the voltage

difference between the other two was monitored by the Keithley 2400 source meter. The measured I-V characteristics in all directions were found to be ohmic over the voltage range -21 V~ 21 V. The electrical conductivities, σ, were extracted taking into account the size of the plate-like single crystal [44]. At room temperature, the various values of σ ranged from 2×10^{-7} Ω^{-1} cm^{-1} to 2×10^{-6} Ω^{-1} cm^{-1}, depended on crystal directions. The conductivity within the manganese vanadate planes was greater than the conductivity between the planes, as expected. The measured electrical conductivities parallel and perpendicular to the layer are shown as a function of the reciprocal of temperature (1000/T) in Fig. 5.4, where σ_1 and σ_2 are conductivities within the manganese vanadate planes, while σ_c is the conductivity between the planes which is along the *c* direction of the crystal structure. The conductivities are all anisotropic in the temperature range 160 K to 428 K, with σ_c smaller than σ_1 and σ_2. Although it is easy to distinguish the *c* direction conductivity which is perpendicular to the plate surface of a single crystal, we are not able to tell which one is the *a* direction or *b* direction conductivity from the shape of the crystal. Here, σ_1 and σ_2 only denote the conductivities in two different directions both parallel to the plate surface of a single crystal. We performed several variable temperature measurements of both σ_1 and σ_2 in the temperature range 285 K-810 K, and no significant difference of the conductivity value among them was observed, indicated the conductivity parallel to the plate surface should be identical in different directions. As observed from Fig. 5.4, the conductivities in all directions increase as the temperature increases, indicating semiconducting behavior. Above 225 K, the activation energy is almost independent of temperature. According to Arrhenius type electrical conductivity equation [78], (detailed description in chapter 3) the activation energy was obtained to be 0.35 eV from the least-square straight-line fits. As discussed in section 5.2, the migration of hydrogen in compound (1) provides protonic conduction. And In the protonic conduction model, the activation energy calculated is the

energy required for the proton to move from μ_3-OH_2 to μ_4-OH. Yet, the plot below 225 K shows a non-linear relationship between the logarithm of the conductivity and the reciprocal of temperature. It indicates the activation energy changes with temperature. The conductivity in this temperature range is influenced by the electronic conduction of the framework which is due to the migration of electrons between manganese ions with different valences [130, 131]. Study of a set of conductivity data parallel to the plate surface in temperature range 100 K to 265 K from a 2-point measurement in the ColdEdge open cycle CoolTran system aids in the explanation. The set of conductivity data was measured with temperature increment of 15 K and waiting time of 20 min and it is plotted as a function of $T^{-1/4}$ in Fig. 5.5. According to the Mott variable range hopping theory at low temperature [132, 133]:

$$\sigma = \sigma_0 e^{-(\frac{T_0}{T})^{1/4}} \tag{5.2}$$

where σ_0 is the maximum electrical conductivity at infinite temperature, T is the temperature and T_0 is a constant equal to $0.016/kN(E_F)$ with k as the Boltzmann constant and $N(E_F)$ as the density of states at Fermi level. As observed from the plot in Fig. 5.5, the conductivity is almost linear in $T^{-1/4}$ indicating a good fit to the Mott variable range hopping theory.

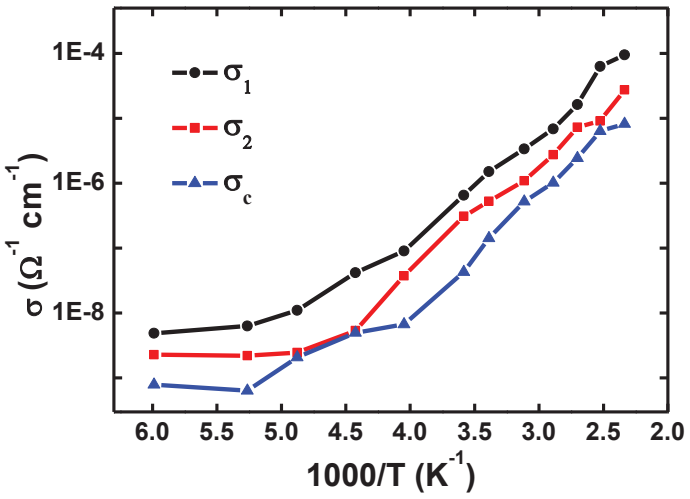

Figure 5.4: Variable temperature conductivity of (1) perpendicular to the manganese vanadate layers plane (triangle), parallel to the manganese vanadate layers plane (circle and square). The temperature range is 160-428 K.

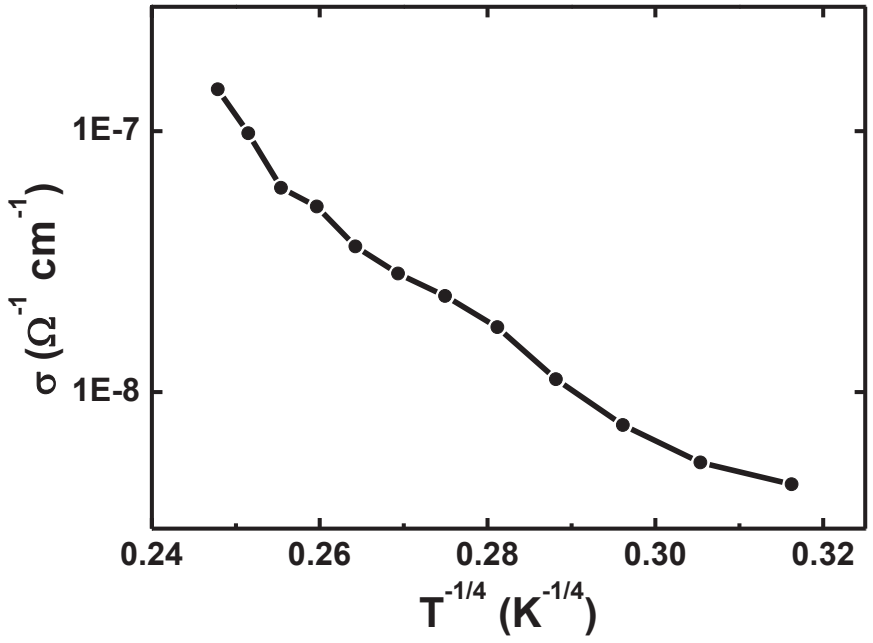

Figure 5.5: Variable temperature conductivity data of (1) parallel to the manganese vanadate layers plane plotted as a function of $T^{-1/4}$. The temperature range is 100-265 K.

The structural change in the temperature range 675 K to 775 K was observed by TGA and deduced from single crystal XRD analysis. To investigate the change in the electrical properties as a function of structural changes, we performed the following two experiments. In the first route, we explored the room temperature electrical properties of compound (1) before and after a heat treatment. The conductivity measurement at room temperature and ambient pressure was performed on the same contacted sample both before and after a heat treatment to provide a direct comparison. This measurement was performed in 2-point geometry to avoid the higher probability of cracking which frequently happens in samples with 4 contacts upon heating (all samples were contacted with PELCO high temperature paste). The contacted samples were measured first to obtain the room temperature conductivity before the heat treatment. Then they were heated at 773 K for two hours in a quartz tube furnace under a flow of N_2 gas. The cooled samples were checked for cracks under an optical microscope, and no obvious changes were observed for the crystals and the contacts. Then the conductivity at room temperature and ambient pressure was remeasured, and a 10-fold decrease observed. The samples were then left under ambient conditions for 10 days, remeasured, but no recovery of the conductivity was observed, indicating an irreversible structural change. In the second route, we carried out the variable temperature conductivity measurement on both the as-synthesized crystals and loose crystals from the same reaction, after subjecting them to the same heat treatment as in the first route. Both 2- and 4-point geometries were employed for the measurement, and no obvious differences were observed. To avoid the affect of the contact resistance and obtain more precise values of conductivity, we only adopted the results from the 4-point measurement. The conductivity of the as-synthesized crystal was measured in the ColdEdge open cycle CoolTran system. We obtained the conductivity in the temperature range 285 K to 810 K, with temperature

increment of 15 K and waiting time of 20 min. The σ_{before} is plotted in Fig. 5.6. The conductivity increases as the temperature increases from 285 K to 660 K showing semiconducting behavior. We extract the activation energy to be 0.35 eV, which is the same value obtained from the data presented in Fig. 5.4. The conductivity decreases about 10 times at 675 K, which is attributed to the structural change as observed in the TGA and XRD result. The loss of μ_3-OH_2 and μ_4-OH sites during the structural change eliminates protonic conduction. As we continue heating the sample we observe the conductivity increasing again from 675 K to 810 K, now due to electronic conduction of the crystal structure after the structural change. The mixed valence of manganese gives rise to the electron hopping between the nearest neighbors Mn^{+2} and Mn^{+3}, which provides electronic conduction [130, 131].

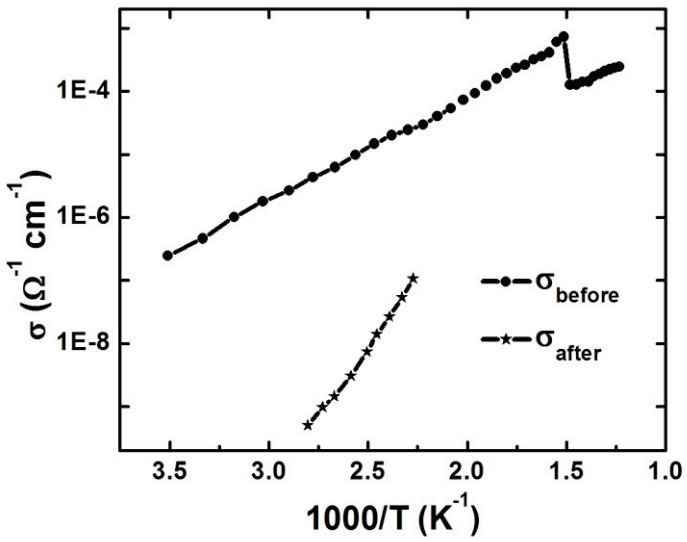

Figure 5.6: Variable temperature conductivity data of (1) before the heat treatment (circle) and after the heat treatment (star), in the direction parallel to the manganese vanadate layers plane. The temperature range is 285-810 K for the former and 360-440 K for the latter.

This electronic conduction was explored a step further with the conductivity measurement of compound (1) after a heat treatment. The variable temperature measurement was performed in the quartz tube system (see Chapter 2) under a flow of N_2 gas from 360 K to about 440 K with the same increment of 10 K and a wait time of 15 min between increments. Conductivity increased with temperature and is plotted together with the conductivity data before the heat treatment (σ_{before}) in Fig. 5.6 for comparison. The former is much smaller than the latter in magnitude.

5.4 Conclusions

In this chapter, we study a hydrothermally synthesized strontium manganese vanadate framework. TGA result indicates a structural change in the temperature range 675 to 775 K. The frameworks before and after the structural change are investigated with single crystal XRD analysis and they are both layered structures. The structural change is attributed to the loss of water from the μ_3-OH_2 and μ_4-OH sites. The crystal structure of a hydrothermally synthesized compound (2) is also studied for comparison. It is similar to the structure of compound (1) after the structural change but has a different composition. We also explore the variable temperature conductivity properties of compound (1) before and after the structural change. Before the structural change, compound (1) has anisotropic protonic conductivity in various crystal directions which increases as the temperature increases. Much smaller conductivity is also detected in compound (1) after the structural change which is attributed to the electronic conduction.

Chapter 6 Electrochemical properties and crystal structures of the cryolite-type compounds $(NH_4)_3V_xGa_{1-x}F_6$ and Na_3VF_6

The elpasolite family with a double perovskite crystal structure has a common formula, A_2BMX_6, where A and B are monovalent cations, M is a multivalent cation and X is a halogen. The cryolite family with formula A_3MX_6 is a special class of elpasolites, with A and B being the same element. Both the elpasolite family and cryolite family have been intensely investigated because of their interesting structural phase transition properties [134-141]. Some of these compounds have a tendency to form a higher symmetry structure when temperature is increased or hydrostatic pressure is lowered [142-145]. The magnetic [146, 147] and ionic transport [135, 148, 149] properties of elpasolites and cryolites have also been extensively studied.

The transition metal center with a mixed valence in a material offers the opportunity for electrochemical energy storage [115, 116, 150]. In this chapter, we report on two cryolite-type compounds, $(NH_4)_3V_xGa_{1-x}F_6$ and Na_3VF_6, both with vanadium as the transition metal center. $(NH_4)_3VF_6$ and $(NH_4)_3GaF_6$ are typical cryolite-type compounds with ammonium ions as the monovalent cations, and $(NH_4)_3V_xGa_{1-x}F_6$ is an intermediate member hydrothermally synthesized from the parent $(NH_4)_3VF_6$ structure with vanadium partially substituted by gallium in the synthesis step. In the preparation, the ratio of gallium substitution affects the color of the crystal samples. According to the previous reports, the parent $(NH_4)_3VF_6$ single crystals are green [147, 151], while $(NH_4)_3GaF_6$ single crystals are colorless [152, 153]. When less gallium is incorporated in the crystals, the color shifts to blue indicating the oxidation state of vanadium is changed by the gallium substitution. This chapter investigates the blue crystal samples of $(NH_4)_3V_xGa_{1-x}F_6$, compound (1a), the greenish blue (an intermediate color between blue and green) crystal samples

of $(NH_4)_3V_xGa_{1-x}F_6$, compound (1b), and the green crystal samples of $(NH_4)_3V_{0.7}Ga_{0.3}F_6$, compound (1c), where the value of x in each of the formulas is not the same. The crystal structure does not change with the amount of substituted gallium, and the compounds discussed have a similar morphology; as example Fig. 6.1 is an optical micrograph of a single crystal of (1a). To study the influence of the ammonium cation in these structures, we have synthesized Na_3VF_6, compound (2), which is green in color. We present a comparative study of (1) and (2) to investigate the roles of ammonium and sodium ions in the structural and electrochemical properties. All crystal structures are determined by single crystal x-ray diffraction (XRD) analyses performed at room temperature. Compounds (1a) and (1c) are cubic and in the space group *Fm3m*, with a slight difference in the lattice constant *a*, while compound (2) has a monoclinic unit cell of space group $P2_1/n$. The electrochemical behavior of compounds (1a) and (1c) is investigated by both solid state and solution state electrochemical methods. For the solid-state electrochemical studies, experimental data is correlated with electrical potential distribution analyses. The AC electrical properties of compounds (1a), (1b), (1c) and (2) are also explored by impedance spectroscopies.

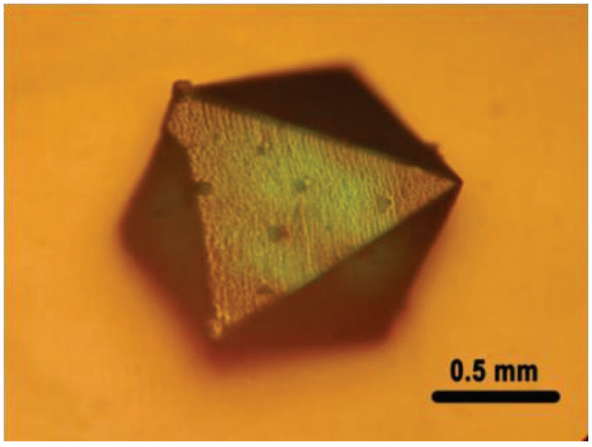

Figure 6.1: Optical micrograph of a single crystal of $(NH_4)_3V_xGa_{1-x}F_6$ (1a) with ~1 mm edge.

6.1 Single crystal x-ray diffraction analysis

Single crystal x-ray diffraction (XRD) measurements were performed on compounds (1a), (1c) and (2), at room temperature. Figure 6.1 shows an optical micrograph of a single crystal of (1a). From the single crystal XRD analysis, both compounds (1a) and (1c) crystallize in the cubic space group *Fm3m*with lattice constant *a* equal to 9.0406(2) Å and 9.0707(1) Å, respectively. The XRD analysis reveals that the substitution of vanadium by gallium in $(NH_4)_3VF_6$ does not induce drastic crystallographic changes. However, the compound (1c) has a larger lattice constant than the compound (1b), because the former contains more gallium than the latter and the gallium ion has a larger radius than the vanadium ion. The crystal data and structure refinement for compound (1c) are shown in Table 6.1 and the atomic positions are shown in Table 6.2. The Wyckoff positions are adopted to identify the atom positions. For a given space group the Wyckoff positions are defined for a set of points whose site-symmetry groups are the conjugate subgroups of the space group. The select Wyckoff positions for the space group *Fm3m* shown in Table 6.3 are from the *International Tables for Crystallography* [154]. In these types of tables, the multiplicity column refers to the number of atomic positions that can be generated by the symmetry at this position, the letter is a label assigned alphabetically without physical meaning, the symmetry column lists all the symmetry elements associated to the position, and the coordinate column lists coordinates of all the atomic positions related by symmetry. V/Ga ions occupy the (0, 0, 0) site (Wyckoff position 4*a*) of the cubic cell. N atoms sit on both the (1/2, 0, 0) and (1/4, 1/4, 1/4) sites (Wyckoff position 4*b* and 8*c*) with an occupying ratio 1:2. V/Ga ions and N atoms in the (1/2, 0, 0) site occupy the same independent crystallographic position in the asymmetric unit, and V/Ga and N sites are

consistent with those in the previously reported crystal structures for $(NH_4)_3VF_6$ [147, 151] and $(NH_4)_3GaF_6$ [153, 155]. The ideal cubic structural model of cryolite-type compounds with NH_4^+ cations [136, 139] is shown in Fig. 6.2, where the F atoms are assigned to the Wyckoff position 24*e*.

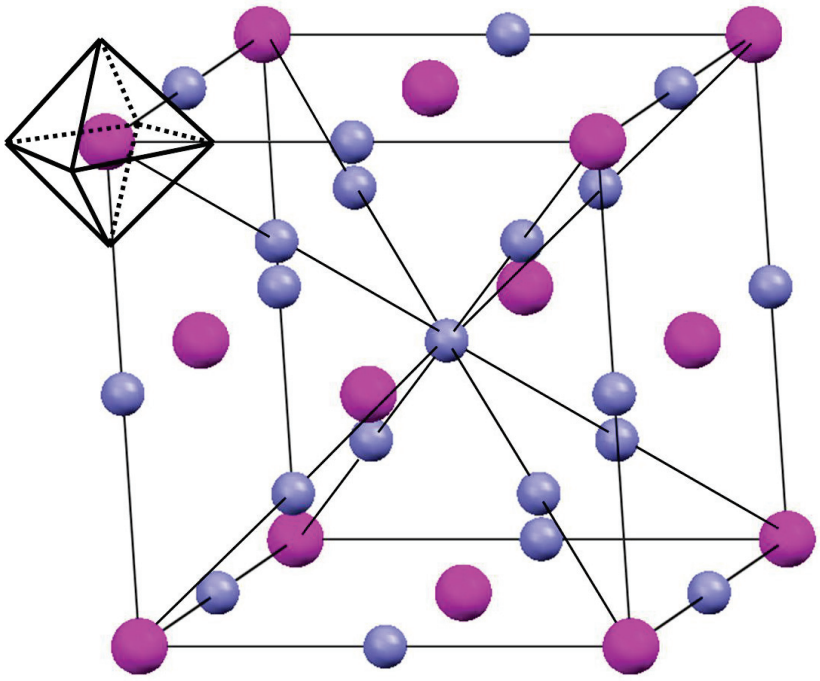

Figure 6.2: Ideal cubic structure of $(NH_4)_3V_{0.7}Ga_{0.3}F_6$ (1c). Magenta balls are V/Ga. Blue balls are N. Black polyhedron is the hypothetical ideal V/GaF_6 octahedron with F atoms assigned to the Wyckoff position 24*e*.

However, in our case, the electron density map indicates that F atoms are located at the Wyckoff position 96j, not 24e. The occupancy frequency of the F sites is constrained to 1/4 to maintain the correct stoichiometry, which suggests that the V/GaF_6 octahedra have a random distribution among four possible orientations [153, 155, 156]. One such orientation is shown in Fig. 6.3, where the V/GaF_6 octahedron sits at the (0, 0, 0) site and NH_4^+ cations sit at both the (1/2, 0, 0) and (1/4,

1/4, 1/4) sites. Positions of H atoms (H1) associated with NH_4^+ ions at the (1/2, 0, 0) site and those (H2) associated with NH_4^+ ions at the (1/4, 1/4, 1/4) site were generated with the N-H bond length set to 0.88 Å. H1 was assigned to the Wyckoff position 32*f*. Because of the 4-fold rotational symmetry, there are two orientations of how NH_4^+ ions are distributed, each of which has a 1/2 occupancy frequency as shown in the Fig. 6.3, where the brown and gray H atoms are from two different orientations. F atoms are attracted by H1 and shift from the ideal Wyckoff position 24*e* as shown in Fig. 6.2 to the Wyckoff position 96*j* as shown in Fig. 6.3. The V/GaF_6 octahedra connect to the NH_4^+ ions through N-H···F bonds [157]. The final structures of compounds (1a) and (1c) were refined with R values of 2.86 and 3.26, respectively. Tables 6.4 and 6.5 list the bond lengths and angles for compound (1c).

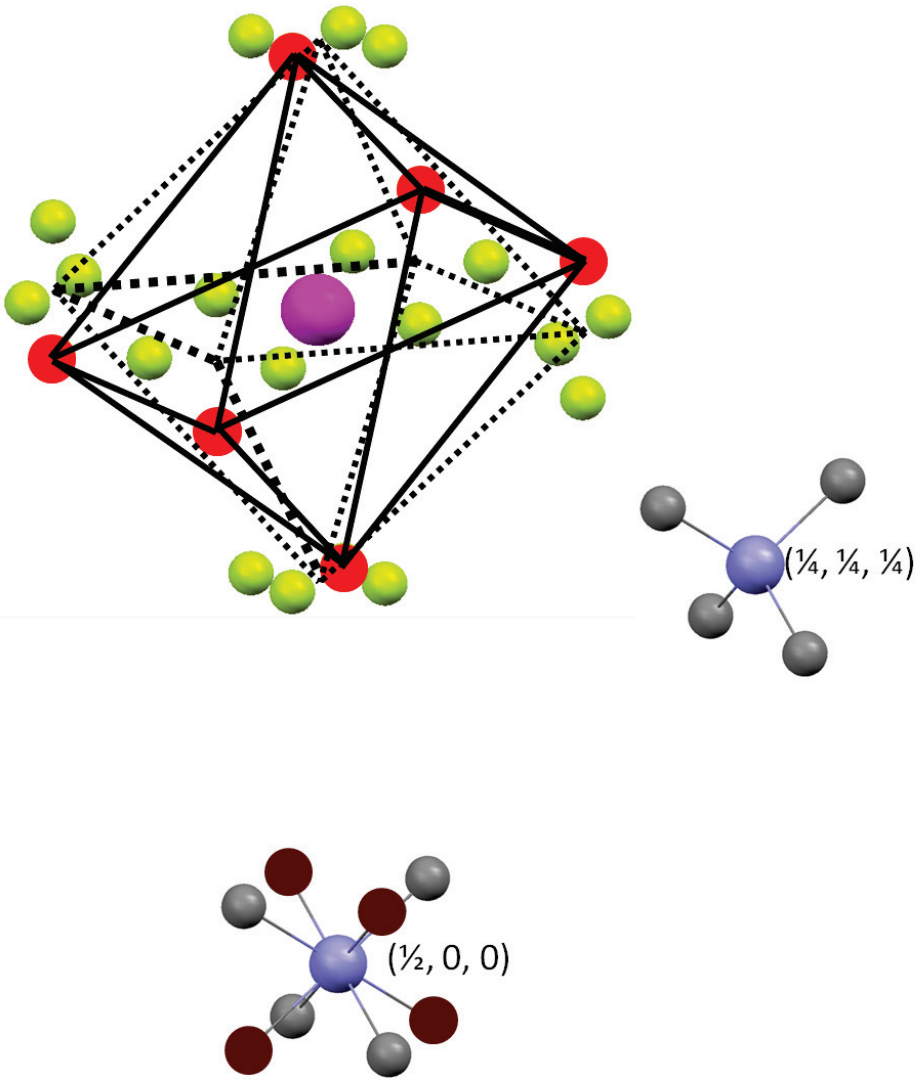

Figure 6.3: Crystal structure of $(NH_4)_3V_{0.7}Ga_{0.3}F_6$ (1c). The V/GaF_6 octahedron sits at the (0, 0, 0) site. The NH_4^+ ions sit at both the (1/2, 0, 0) and (1/4, 1/4, 1/4) sites. Magenta balls are V/Ga. Blue balls are N. Gray and brown balls are H. Red and yellowgreen balls are 96*j* F positions with red occupied and yellowgreen unoccupied. Solid lines show one possible V/GaF_6 octahedron orientation. Dashed lines show the hypothetical V/GaF_6 octahedron orientation.

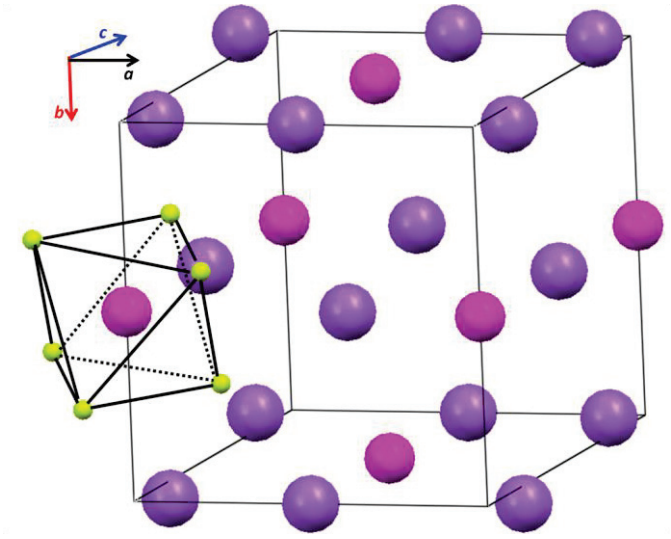

Figure 6.4: Crystal structure of Na_3VF_6 (2). Magenta balls are V. Violet balls are Na. Yellowgreen balls are F. Black polyhedron is VF_6 octahedron.

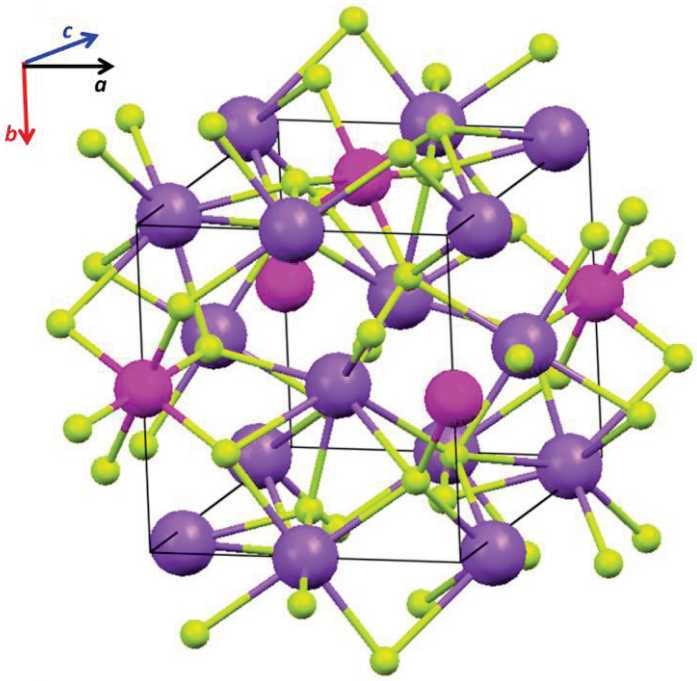

Figure 6.5: Crystal structure of Na_3VF_6 (2) showing the three dimensional framework. Magenta balls are V. Violet balls are Na. Yellowgreen balls are F.

Single crystal XRD analysis was performed on compound (2) at room temperature. The structure was refined in the monoclinic space group $P2_1/n$, and was found to agree with previous reports [146, 158]. The crystal data and structure refinement are shown in Table 6.6. The lattice parameters are $a = 5.5147(11)$ Å, $b = 5.7021(11)$ Å, $c = 7.9371(15)$ Å, and $\beta = 90.147(16)°$. The R value is 4.43 for the final structure. Figure 6.4 depicts the crystal structure, and we indicted the disorder around the Na site at (0.4873(3), 0.4464(3), 0.7534(3)). Tables 6.7, 6.8 and 6.9 show the fractional atomic coordinates, bond lengths and bond angles, respectively. With Na^+ ions as the monovalent cations, the VF_6 octahedra tilt and rotate to form a less symmetric structure than the cryolite-type family with NH_4^+ cations. The difference between the VF_6 octahedra in the Na_3VF_6 structure and the hypothetical ideal V/GaF_6 octahedra in the $(NH_4)_3V_{0.7}Ga_{0.3}F_6$ structure, averaged over all 4 possible tilted V/GaF_6 octahedra, can be deduced by comparing Figs. 6.2 and 6.4. The tilted VF_6 and NaF_6 octahedra share vertices and form a three dimensional framework, as shown in Fig. 6.5. The remaining Na^+ ions fill the holes between these octahedra.

Table 6.1: Crystal data and structure refinement for (1c)

Chemical formula	$[NH_4]_{12}[Ga_{0.30}V_{0.70}F_6]_4$
Formula weight	898.71
Temperature	293(2) K
Wavelength	0.71073Å
Crystal system	Cubic
Space group	$Fm\bar{3}m$
Unit cell dimensions	a = 9.07070(10) Å
Volume	46.315(14) $Å^3$
Z	1
Density (calculated)	2.000 Mg m^{-3}
Absorption coefficient	2.085 mm^{-1}
F(000)	450
Crystal size	0.20 x 0.13 x 0.05 mm^3
Theta range for data collection	3.89 to 32.39°
Index ranges	-13<=h<=13, -13<=k<=13, -7<=l<=13
Reflections collected	1951
Independent reflections	98 [R(int) = 0.0907]
Completeness to theta = 30.09°	100.0 %
Absorption correction	Gaussian
Max. and min. transmission	0.912 and 0.765
Refinement method	Full-matrix least-squares on F^2
Data / restraints / parameters	98 / 2 / 14
Goodness-of-fit (S) on F^2	1.132
Final R indices [I>2sigma(I)]	R = 0.0286, wR2 = 0.0720
R indices (all data)	R = 0.0286, wR2 = 0.0720
Largest diff. peak and hole	0.350 e $Å^{-3}$and -0.391 e $Å^{-3}$

Table 6.2: Fractional atomic coordinates for (1c)

Element	Equivalent position			Occupancy
	x	y	z	
Ga	0.0000	0.0000	0.0000	0.30
V	0.0000	0.0000	0.0000	0.70
N1	0.5000	0.5000	0.5000	1.00
N2	0.2500	0.2500	0.2500	1.00
F	0.2012(6)	0.0000	0.0508(12)	0.25
H1	0.5558(13)	0.5558(13)	0.5558(13)	0.50
H2	0.3039(13)	0.3039(13)	0.1961(13)	0.50

Table 6.3: Selected Wyckoff positions for space group ($Fm\bar{3}m$) from the International Tables for Crystallography [154]

Multiplicity	Wyckoff letter	Site symmetry	Coordinates
			(0, 0, 0) +, (0, 1/2, 1/2) +, (1/2, 0, 1/2) +, (1/2, 1/2, 0) +
96	j	m . .	(0, y, z), (0, -y, z), (0, y, -z), (0, -y, -z), (z, 0, y), (z, 0, -y), (-z, 0, y), (-z, 0, -y), (y, z, 0), (-y, z, 0), (y, -z, 0), (-y, -z, 0), (y, 0, -z), (-y, 0, -z), (y, 0, z), (-y, 0, z), (0, z, -y), (0, z, y), (0, -z, -y), (0, -z, y), (z, y, 0), (z, -y, 0), (-z, y, 0), (-z, -y, 0)
32	f	. 3m	(x, x, x), (-x, -x, x), (-x, x, -x), (x, -x, -x), (x, x, -x), (-x, -x, -x), (x, -x, x), (-x, x, x)
24	e	4m . m	(x, 0, 0), (-x, 0, 0), (0, x, 0), (0, -x, 0), (0, 0, x), (0, 0, -x)
8	c	-43m	(1/4, 1/4, 1/4), (1/4, 1/4, 3/4)
4	b	m-3m	(1/2, 1/2, 1/2)
4	a	m-3m	(0, 0, 0)

Table 6.4: Bond lengths in the structure of (1c)

Bond	Length/ Å	Bond	Length/ Å
V/Ga-F	1.882(5)	F-F#1	0.651(16)
		F-F#2	0.92(2)

Symmetry codes: #1 x, z, -y. #2 x, y, -z

Table 6.5: Bond angles in the structure of (1c)

Angle	Angle/ °	Angle	Angle/ °
F#1-V/Ga-F#3	76.3(3)	F-V/Ga-F#7	118.3(7)
F#3-V/Ga-F#4	86.57(16)	F#2-V/Ga-F#3	90.0
F-V/Ga-F#3	61.7(7)	F-V/Ga-F#2	28.3(7)
F-V/Ga-F#1	19.9(5)	F#3-V/Ga-F#8	151.7(7)
F#3-V/Ga-F#5	103.7(3)	F#1-F-F#9	90.000(1)
F#4-V/Ga-F#5	160.1(5)	F#1-F-F#2	45.000(1)
F-V/Ga-F#5	93.43(16)	F#1-F-V/Ga	80.0(2)
F#5-V/Ga-F#6	180.0(7)	F#2-F-V/Ga	75.8(3)

Symmetry codes: #1 x, z, -y. #2 x, y, -z. #3 z, -y, x. #4 z, x, y. #5 -y, -x, -z. #6 y, x, z. #7 -z, y, -x. #8 z, y, -x. #9 x, -z, -y.

Table 6.6: Crystal data and structure refinement for (2)

Chemical formula	Na_3VF_6
Formula weight	233.91
Temperature	299.1(2) K
Wavelength	0.71073 Å
Crystal system	Monoclinic
Space group	$P2_1/n$
Unit cell dimensions	a = 5.5147(11) Å
	b = 5.7021(11) Å
	c = 7.9371(15) Å
	β = 90.147(16)°
Volume	249.58(8) $Å^3$
Z	2
Density (calculated)	3.113 Mg m^{-3}
Absorption coefficient	2.289 mm^{-1}
F(000)	220
Crystal size	0.16 x 0.14 x 0.11 mm^3
Theta range for data collection	4.201-32.201°
Index ranges	-8<=h<=8, -8<=k<=8, -11<=l<=11
Reflections collected	2093
Independent reflections	2093
Completeness to theta = 30.09°	99.7 %
Absorption correction	Analytical
Max. and min. transmission	0.836 and 0.776
Refinement method	Full-matrix least-squares on F^2
Data / restraints / parameters	2093 / 0 / 50
Goodness-of-fit (S) on F^2	0.919
Final R indices [I>2sigma(I)]	R = 0.0443, wR2 = 0.1189
R indices (all data)	R = 0.0777, wR2 = 0.1322
Largest diff. peak and hole	0.541 e $Å^{-3}$and -0.636 e $Å^{-3}$

Table 6.7: Fractional atomic coordinates for (2)

Element	Equivalent position			Occupancy
	x	y	z	
V	0.5000	0.0000	0.5000	1.00
Na1	0.0000	0.5000	0.5000	1.00
Na2	0.4873(3)	0.4464(3)	0.7534(3)	1.00
F1	0.6110(4)	0.0525(4)	0.7257(3)	1.00
F2	0.3352(4)	-0.2769(4)	0.5672(3)	1.00
F3	0.2189(4)	0.1742(4)	0.5488(3)	1.00

Table 6.8: Bond lengths in the structure of (2)

Bond	Length/ Å	Bond	Length/ Å
V-F1	1.915(2)	Na2-F1#3	2.302(3)
V-F2	1.899(2)	Na2-F2#4	2.895(3)
V-F3	1.882(2)	Na2-F2#5	2.612(3)
Na1-F1#1	2.283(2)	Na2-F2#2	2.318(3)
Na1-F2#2	2.305(2)	Na2-F3#5	2.335(3)
Na1-F3	2.249(2)	Na2-F3	2.688(3)
Na2-F1	2.358(3)	Na2-F3#6	2.754(3)

Symmetry codes: #1 x-1/2, -y+1/2, z-1/2. #2 x, y+1, z. #3 -x+3/2, y+1/2, -z+3/2. #4 -x+1, -y, -z+1. #5 -x+1/2, y+1/2, -z+3/2.

Table 6.9: Angles in the structure of (2)

Angle	Angle/ °	Angle	Angle/ °
F1-V-F1#4	180	F2#2-Na2-F3#6	151.52(11)
F2-V-F1	91.09(10)	F2#5-Na2-F3#6	74.30(8)
F2-V-F1#4	88.91(10)	F3#5-Na2-F1	137.25(12)
F2-V-F2#4	180	F3#5-Na2-F2#4	160.53(11)
F3-V-F1	89.21(10)	F3#5-Na2-F2#5	64.62(9)
F3#4-V-F1	90.79(10)	F3#6-Na2-F2#4	120.52(9)
F3-V-F2#4	90.82(10)	F3-Na2-F2#4	57.52(8)
F3-V-F2	89.18(10)	F3#5-Na2-F3#6	78.01(11)
F3#4-V-F3	180	F3#5-Na2-F3	117.32(8)
F1#1-Na1-F1#5	180	F3-Na2-F3#6	128.59(7)
F1#1-Na1-F2#7	85.62(8)	V-F1-Na1#9	141.80(12)
F1#1-Na1-F2#2	94.38(8)	V-F1-Na2	98.31(10)
F2#7-Na1-F2#2	180.00(15)	V-F1-Na2#10	109.36(12)
F3-Na1-F1#1	84.90(9)	Na1#9-F1-Na2#10	99.04(10)
F3#8-Na1-F2#7	89.21(8)	Na2#10-F1-Na2	121.48(12)
F3-Na1-F2#7	90.79(8)	V-F2-Na1#11	141.06(12)
F3-Na1-F3#8	180	V-F2-Na2#9	94.30(10)
F1#3-Na2-F1	88.76(8)	V-F2-Na2#4	82.37(9)
F1-Na2-F2#5	77.54(9)	V-F2-Na2#11	124.93(12)
F1#3-Na2-F2#2	102.33(11)	Na1#11-F2-Na2#4	83.40(8)
F1-Na2-F2#4	60.08(8)	Na1#11-F2-Na2#11	93.46(9)
F1-Na2-F3#6	73.04(9)	Na2#11-F2-Na2#4	102.16(10)
F1#3-Na2-F3#6	63.90(9)	Na2#9-F2-Na2#4	150.93(12)
F1#3-Na2-F3#5	106.00(11)	V-F3-Na1	147.40(13)
F1-Na2-F3	63.41(9)	V-F3-Na2	88.67(9)
F1#3-Na2-F3	136.35(11)	V-F3-Na2#1	94.21(10)
F2#2-Na2-F1	133.89(12)	V-F3-Na2#9	104.34(11)
F2#2-Na2-F2#5	115.70(8)	Na1-F3-Na2#9	108.26(10)

F2#5-Na2-F2#4	123.27(8)	Na1-F3-Na2	85.50(9)
F2#2-Na2-F2#4	77.84(10)	Na1-F3-Na2#1	79.15(8)
F2#5-Na2-F3	70.93(8)	Na2#9-F3-Na2	100.57(9)
F2#2-Na2-F3#5	82.75(11)	Na2-F3-Na2#1	155.77(11)
F2#2-Na2-F3	79.06(10)	Na2#9-F3-Na2#1	101.99(11)

Symmetry codes: #1 x-1/2, -y+1/2, z-1/2. #2 x, y+1, z. #3 -x+3/2, y+1/2, -z+3/2. #4 -x+1, -y, -z+1. #5 -x+1/2, y+1/2, -z+3/2. #6 x+1/2, -y+1/2, z+1/2. #7 -x, -y, -z+1. #8 -x, -y+1, -z+1. #9 -x+1/2, y-1/2, -z+3/2. #10 -x+3/2, y-1/2, -z+3/2. #11 x, y-1, z.

As previously discussed, compounds (1a), (1b) and (1c), with NH_4^+ ions, crystallize in a higher symmetry group than compound (2), with Na^+ ions, at room temperature. The first explanation of this phenomenon is based on a consideration of packing of ions [146]. Different symmetries are caused by the different radii of the monovalent cations in the elpasolite family and cryolite family structures. Larger monovalent cations have the tendency to form structures with higher symmetry. Since NH_4^+ ions have larger radii than Na^+ ion, compounds containing the former will form crystals with a higher symmetry group. The second factor that leads to higher symmetry in compounds containing NH_4^+ ions is due to the tetragonal symmetry of NH_4^+ ions. The NH_4^+ ion at the (1/4, 1/4, 1/4) site is located at the center of a cubic that is 1/8 of the unit cell as shown in Fig. 6.6. The eight vertices of the cubic are occupied by four NH_4^+ ions and four $(V/GaF_6)^{3-}$ ions respectively to form a tetrahedral environment, which is favored by a NH_4^+ tetrahedron with four H atoms pointing toward the four negatively charged V/GaF_6 octahedra. Consequently, the tetrahedral NH_4^+ located at the (1/4, 1/4, 1/4) site enhances the stability of the cubic structure with an orientational preference not present to the spherical Na^+ ion. The NH_4^+ at the (1/2, 0, 0) site also plays an important role in stabilizing the cubic structure. As discussed before, the F atoms are attracted by the H atoms, causing the V/GaF_6 octahedra to tilt and deviate from the 4-fold

rotational axis. As a result, the V/GaF_6 octahedra are disordered over four orientations, which stabilizes the cubic structure by increasing the entropy and lowering the free energy of the crystal [139].

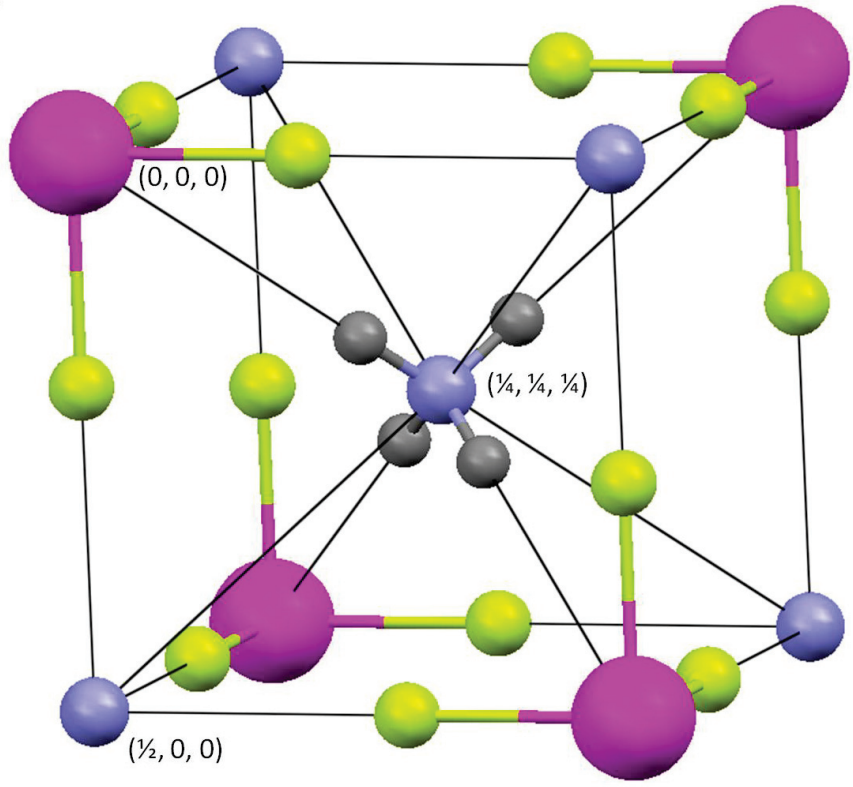

Figure 6.6: Crystal structure of $(NH_4)_3V_{0.7}Ga_{0.3}F_6$ (1c) showing the tetrahedral environment that is suitable for an NH_4^+ ion. Magenta balls are V/Ga. Yellowgreen balls are ideal position of F. Blue balls are N. Gray balls are H.

6.2 Solution state electrochemical characterization

The electrochemical behavior of compounds (1a) and (1c) in aqueous solutions was studied with the experimental techniques as described in Subsection 2.3.5.1. We adopted the same experimental setting as shown in Fig. 2.10. The cyclic voltammetry measurement was performed in a 10 ml

beaker (diameter 25 mm). The working electrode (WE) and counter electrode (CE) were fabricated by covering silver wires (1 mm diameter) with EPO-TEK H20E conductive silver epoxy and curing it at 318 K for 12 hours to simulate the silver epoxy contacts we used in the solid state electrochemistry study. A commercial Ag/AgCl reference electrode (RE) from Koslow Scientific Company was used as a reference. The separations between the three electrodes, which were kept constant throughout the measurements, were 2 mm between WE and CE, 15 mm between the CE and RE and 17 mm between WE and RE. A Keithley 2400 source meter was used as the voltage source and to monitor the current between the WE and CE, while a Keithley 2000 multimeter was used to measure the voltage difference between the WE and RE. We performed baseline measurements of 5 ml of DI water, of 0.020 M VCl_4 aqueous solution and of 0.030 M NH_4VO_3 aqueous solution, respectively. Solutions of (1a) and (1c) were prepared by dissolving 0.061 g of (1a) in 5 mL of DI water and 0.025 g of (1c) in 4 ml DI water to obtain 0.053 M aqueous solution of (1a) and 0.026 M aqueous solution of (1c), respectively. The electrochemical measurements of these two solutions as a function of time were performed to study the electrochemical behavior of compounds (1a) and (1c) with respect to the oxidation state of the vanadium centers in an aqueous solution. We applied different potential sweep ranges between the WE and CE; -1.2 to 1 V provided the best potential window to observe and track the current peaks. The scan rate was kept constant at 20 mV s^{-1}. In this section, all the cyclic voltammetry measurements were performed at room temperature and the voltammograms were recorded and plotted with both the potentials of the WE vs. CE (black dot plus lines in Figs. 6.7, 6.8, 6.9 and 6.10), and the WE vs. Ag/AgCl RE (green dot plus lines in Figs. 6.7, 6.8, 6.9 and 6.10). The current peaks in the plots of the potential between the WE and CE, without a stable and standardized reference potential, do not provide the redox potential. However, the plots with constant scan rate allow us to obtain current versus time

information and to compare the specific charges absorbed during the redox reactions. The potential of the WE vs. Ag/AgCl RE was swept with an effective scan rate and an effective potential sweep range which varied based on the redox reaction of vanadium ions in the electrolyte. The current peaks in the plots of the potential of the WE vs. Ag/AgCl RE provide the redox potential of different redox reactions of vanadium ions.

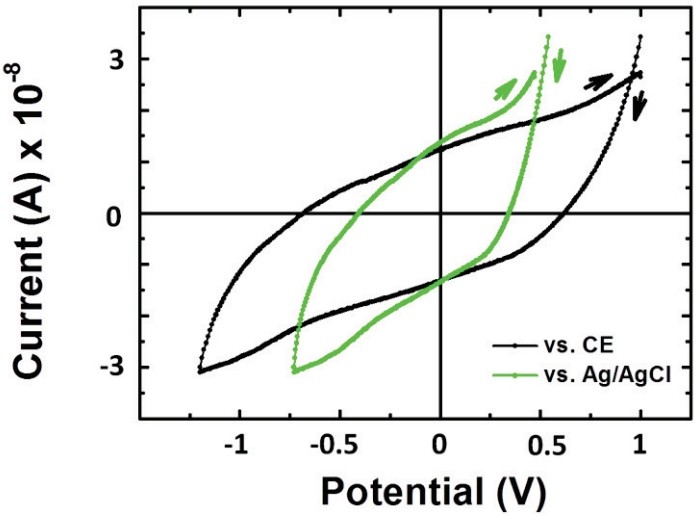

Figure 6.7: Voltammogram of DI water baseline, 1st cycle: potential of the WE vs. CE, which is the potential sweep applied between the WE and CE (black dot plus line), and potential of the WE vs. Ag/AgCl RE, which is the potential measured between the WE and Ag/AgCl RE (green dot plus line). Current is measured between the WE and CE.

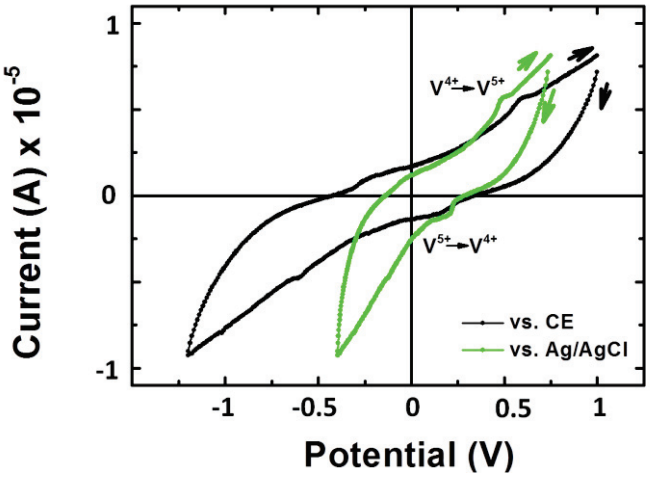

Figure 6.8: Voltammogram of 0.030 M NH_4VO_3 aqueous solution baseline, 1st cycle: potential of the WE vs. CE, which is the potential sweep applied between the WE and CE (black dot plus line), and potential of the WE vs. Ag/AgCl RE, which is the potential measured between the WE and Ag/AgCl RE (green dot plus line). Current is measured between the WE and CE.

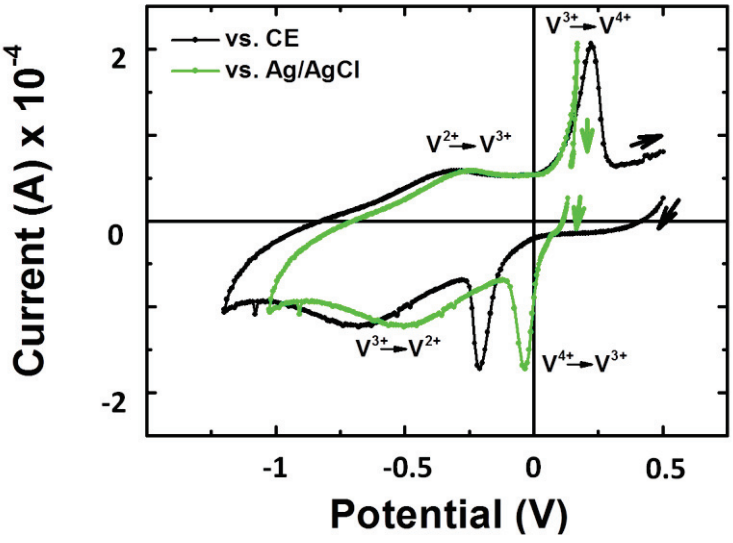

Figure 6.9: Voltammogram of 0.020 M VCl_4 aqueous solution baseline, 8th cycle: potential of the WE vs. CE, which is the potential sweep applied between the WE and CE (black dot plus line), and potential of the WE vs. Ag/AgCl RE, which is the potential measured between the WE and Ag/AgCl RE (green dot plus line). Current is measured between the WE and CE.

Baseline measurements of DI water, VCl_4 aqueous solution and NH_4VO_3 aqueous solution were performed for comparison. Figure 6.7 shows that for DI water the magnitude of current is small and there is no observable current peak. Figure 6.8 illustrates the electrochemical behavior of the NH_4VO_3 aqueous solution with V^{5+}, which as expected is yellow in color [159]. We applied the voltage sweep between the WE and CE by starting with the WE at 1 V vs. the CE. The potential was then swept toward the more negative value (cathodic scan) until -1.2 V, and then swept back toward the more positive value (anodic scan) to 1 V. The voltammogram with the potential of the WE vs. Ag/AgCl (green dot plus line in Fig. 6.8) indicates a current peak couple with a half-wave potential, which is the middle position of the two peaks, at 0.35 V. A reduction peak of V^{+5} to V^{+4} is observed in the cathodic scan and an oxidation peak of V^{+4} to V^{+5} is observed in the anodic scan. The same voltage sweeps were performed up to 10 times and the cyclic voltammograms obtained did not change significantly. The first cycle was shown in Fig. 6.8. We performed similar cyclic voltammetry measurement of the VCl_4 aqueous solution with V^{+4}, which has a blue color associated with the oxidation state of vanadium [159]. The voltage between the WE and CE was swept from 0.5 V to -1.2 V, then back to 0.5 V. One current peak couple of V^{+3}/V^{+4} was observed in the first 6 cycles, and by the 7^{th} cycle, another current peak couple V^{+2}/V^{+3} appears, after the increase of the V^{+3} concentration during the first 6 cycles. The newly observed peak dramatically increased in magnitude in the 8^{th} cycle. Figure 6.9 shows the cyclic voltammogram of the 8^{th} cycle with 2 current peak couples at 0.06 V and -0.38 V, respectively. The cathodic scan yields two reduction peaks of V^{+4} to V^{+3} and V^{+3} to V^{+2}, and the anodic scan yields two oxidation peaks of V^{+2} to V^{+3} and V^{+3} to V^{+4}. Acquiring these baseline measurements provided the potentials of the vanadium-containing current peak couples, which are qualitatively similar to previous reports [160-162] but with slight differences because of the different reactants involved and different

vanadium ion concentrations in our samples.

As previously discussed, the substitution of vanadium by gallium affects the oxidation state of vanadium in $(NH_4)_3V_xGa_{1-x}F_6$ and yields samples containing vanadium ions with mixed valences. The color of vanadium ion in the aqueous solutions varies with its oxidation states, which is violet for 2^+, green for 3^+, blue for 4^+ and yellow for 5^+ [159]. Based on the color, we inferred the aqueous solution of compound (1a) had more V^{4+} ions, while that of (1c) had more V^{3+} ions. We performed the cyclic voltammetry measurements on these two solutions as a function of time. We started with the WE at 1 V vs. the CE. During the cathodic scan to -1.2 V, the vanadium ions were reduced. The potential was then swept back to 1 V, and the vanadium ions were oxidized. For each measurement, various current peaks attributed to different redox reactions were observed, which increased in magnitude during the first several cycles until steady-state conditions were attained. Sweeps were made until the magnitude of the current peaks stabilized, indicating steady-state conditions. For differently aged solutions, steady-state conditions appear after different number of sweeps, as indicated in Figs. 6.10(a), 6.10(c), 6.10(d), 6.10(e), 6.10(f), 6.10(i) and 6.10(j) where cycle numbers provided are those of the first cycle after steady-state conditions were attained. Further, intermediate steps, i.e. before the steady-state conditions are attained, for compound (1a) on day 5 and for compound (1c) on day 3 are shown in Figs. 6.10(b), 6.10(g) and 6.10(h), respectively, to show the progression of vanadium oxidation states. The current peak couples corresponding to different redox reactions are identified by the current peak potentials observed in the baseline measurements of the aqueous solutions of NH_4VO_3 and VCl_4. The current peak potentials of the different redox reactions between vanadium ions in different oxidation states obtained in the voltammograms of the aqueous solutions of compounds (1a) and (1c) are slightly different than those obtained for NH_4VO_3, and VCl_4, due to different concentrations of vanadium ions of various

oxidation states. The solution state voltammograms of compounds (1a) and (1c) are plotted in Fig. 6.1.0, where Figs. 6.10(a), 6.10(b), 6.10(c), 6.10(d) and 6.10(e) show results of compound (1a) on days 1, 5, 10 and 21, respectively. The initial color of the solution of (1a) is blue, which changed to green after 1 day of exposure to atmospheric conditions, indicating oxidation of the vanadium centers. The color green indicates a combination of blue from V^{4+} and yellow from V^{5+} [159]. The solution was monitored and data recorded on days 5 and 10, when the solution was still in green color. The solution turned yellow after 21 days. The voltammograms in Figs. 6.10(a), 6.10(b), 6.10(c), 6.10(d) and 6.10(e) are in agreement with the observation based on the solution color and the oxidation states of vanadium. The voltammogram on day 1 after steady-state condition shows a small current peak couple of V^{2+}/V^{3+} and a large current peak couple of V^{3+}/V^{4+}. The current peak couples of both V^{2+}/V^{3+} and V^{3+}/V^{4+} then decrease while the current peak couple of V^{4+}/V^{5+} increases on days 5 and 10 as shown in Figs 6.10(b), 6.10(c) and 6.10(d). On day 21, only the V^{4+}/V^{5+} current peak couple is observed. The solution state voltammograms of compound (1c) are shown in Figs. 6.10(f), 6.10(g), 6.10(h), 6.10(i) and 6.10(j) on days 1, 3 and 7, respectively. The initial color of the solution of (1c) is green, indicating a more mixed valance state than the solution of compound (1a). On day 1, the voltammogram of solution of (1c) starts with a large V^{2+}/V^{3+} current peak couple and a small V^{3+}/V^{4+} current peak couple, which is expected for a solution with more V^{3+} ions. On day 3, the measurements were performed for up to 25 cycles. At the 3^{rd} cycle, a voltammogram similar to that of compound (1a) on day 1 is observed, indicating that the solution of (1c) is aged in 2 days to attain a similar vanadium mixed valance state as that of solution of (1a) on day 1. We then noted that the voltammogram change after the 3^{rd} cycle in the same day following the same trend as we observed in compound (1a) on day 5. Figs. 6.10(g) and 6.10(h) show the solution state voltammograms of the 12^{th} and 20^{th} cycles of compound (1c) on day 3,

which are similar to those of the 5^{th} and 18^{th} cycles of compound (1a) recorded on day 5. After 7 days, the solution of (1c) is yellow in color and only the V^{4+}/V^{5+} current peak couple is observed, and the voltammogram of (1c) is similar to the voltammogram of (1a) on day 21.

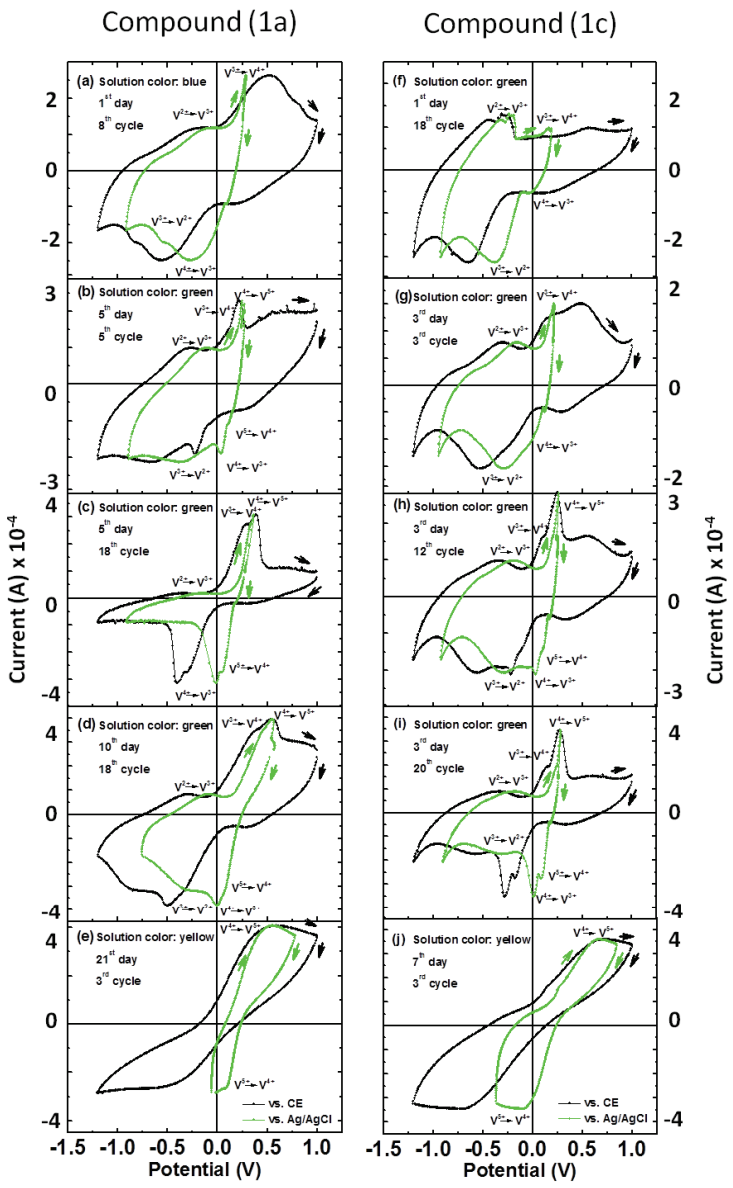

Figure 6.10: Voltammograms of aqueous solutions of (1a) in the left column, and (1c) in the right column, with silver epoxy as WE and CE, as a function of time. The starting color of the solution is indicated, and its implications regarding the oxidation states of vanadium centers are discussed in the text. For (1a): (a) 1st day, (b and c) 5th day, (d) 10th day, and (e) 21st day. For (1c): (f) 1st day, (g, h and i) 3rd day, and (j) 7th day. Shown are potential of the WE vs. CE, which is the potential sweep applied between the WE and CE (black dot plus line), and potential of the WE vs. Ag/AgCl RE, which is the potential measured between the WE and Ag/AgCl RE (green dot plus line). Current is measured between the WE and CE.

6.3 Solid state electrochemical characterization

Solid state electrochemistry is the study of the electrochemical properties of solids, including solid electrolytes. We performed the solid state electrochemical measurements using the single crystal of compound (1a) as the electrolyte. Four silver electrodes were placed on a single crystal with a ~1 mm edge by using EPO-TEK H20E silver conductive epoxy. All four electrodes had a diameter of ~0.1 mm and were cured at 318 K overnight. The sample was then connected to the dip header with gold wires. The room temperature conductivities obtained were 2×10^{-7} $\Omega^{-1}cm^{-1}$ for (1a) by the 4-point conductivity measurement method [44] (detailed discussion in Section 2.3.2), and 3×10^{-7} $\Omega^{-1}cm^{-1}$ for (1b), and 5×10^{-7} $\Omega^{-1}cm^{-1}$ for (1c) by a 3-point measurement. A 3-point electrochemical measurement was performed with three of the four silver electrodes as working electrode (WE), counter electrode (CE), and pseudo-reference electrode (PRE), using the Keithley 2000 multimeter and Keithley 2400 source meter, as shown in Fig. 2.11. Because of the small size of the silver electrodes, we assume the presence of a significant potential gradient only in the close proximity of the WE and CE during measurements. In the bulk, the potential was assumed to be uniform, and the potential gradient was small in the region where we placed the PRE; the simulation of the potential distribution is presented in Section 6.4. Therefore, the PRE placement satisfied the geometry requirement of the reference electrode placement in the solid electrolyte [47, 48] and provided a constant potential. However, the potential provided by the PRE, which was based on the composition of the electrolyte, was not standardized. To address this issue, an Ag/AgCl reference electrode system was designed, as discussed in Subsection 2.3.5.2 and shown in Fig. 2.12. The cyclic voltammograms with potentials of the WE vs. Ag/AgCl and WE vs. PRE were obtained by the measurement system with and without the Ag/AgCl reference, respectively. The potential difference of the Ag/AgCl RE and the PRE was extracted from the solid state

voltammograms with potentials of the WE vs. Ag/AgCl and WE vs. PRE and was found to be small, ~ -0.1 V. This information was used to convert the voltammogram of the WE vs. the pseudo RE (PRE) to that of the WE vs. a standard RE, Ag/AgCl.

The cyclic voltammetry measurements were performed with different voltage sweep ranges at a constant scan rate of 100 mV s^{-1} at room temperature. Voltage sweeps of 0 V to -10 V to 0 V and 0 V to 10 V to 0 V between the WE and CE were performed for more than 10 cycles for each sample. No current peak was observed. During the 10 V to -10 V to 10 V voltage sweep, no obvious current peak was observed initially as well. But, after the sweep was repeated, current peaks appeared. The magnitude of the current peaks then increased and stabilized after more than 10 cycles. The measurements were also performed by choosing three different electrodes as the WE, CE and PRE out of the four electrodes. No obvious distinction was observed in the voltammogram with different WE, CE and PRE arrangements. Figure 6.11 shows a representative cyclic voltammogram with both potentials of the WE vs. CE (black dot plus line) and WE vs. Ag/AgCl RE (green dot plus line); the upper left sketch also shows the arrangement of the electrodes. The plot of the potential between the WE and CE with a constant scan rate allows us to obtain the absorbed specific charge.

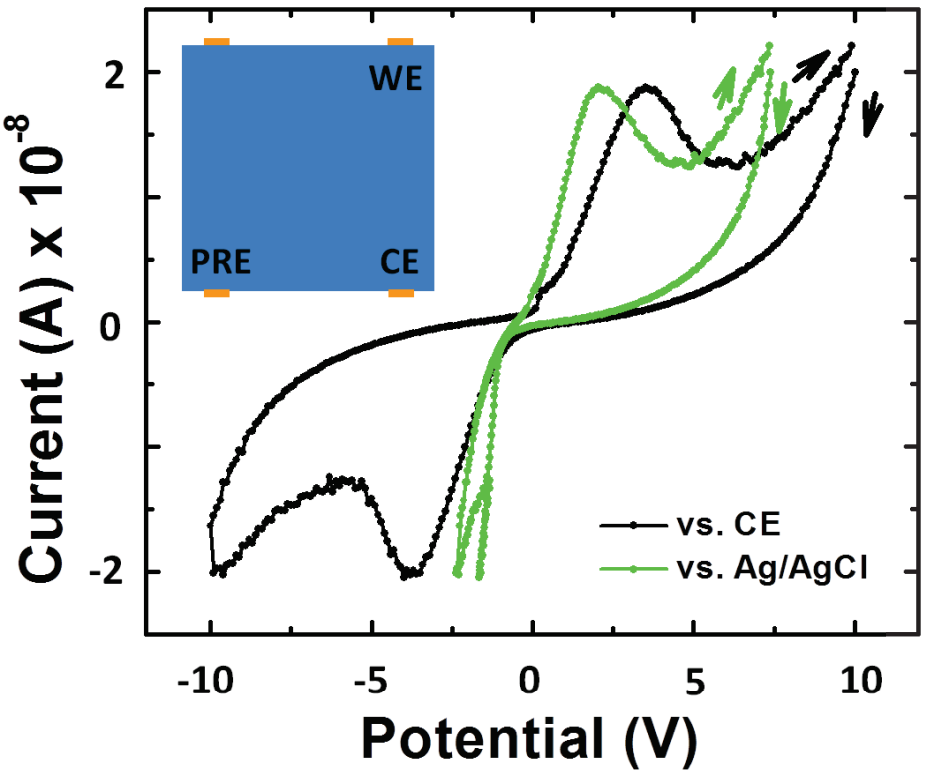

Figure 6.11: Voltammogram of a single crystal of (1a), 15th cycle: potential of the WE vs. CE, which is the potential sweep applied between the WE and CE (black dot plus line), and potential of the WE vs. Ag/AgCl RE, which is the potential measured between the WE and Ag/AgCl RE (green dot plus line). Current is measured between the WE and CE. The sketch on the upper left shows the arrangement of electrodes on the sample. The 15th cycle shown is after the sample was subjected to cyclic sweeps of 10 V to -10 V to 10 V.

Two current peaks are observed in the voltammograms with the potentials of the WE vs. CE and for the WE vs. Ag/AgCl RE, as shown in Fig. 6.11. The two current peaks correspond to the electrochemical reactions that occur between vanadium ions with different oxidation states in the vicinity of the WE and CE, respectively. In the voltammogram with potential of the WE vs. CE,

the two peaks are nearly symmetric. The peak potentials are between -4 V and -3 V for the cathodic peak and between 3 V and 4 V for the anodic peak, with values changing slightly between measurements because the concentration of vanadium ions near the WE and CE varies. In the voltammogram with the potential of the WE vs. Ag/AgCl RE, a narrowing of the cathode peak is observed, which is attributed to the influence of the electrochemical reaction that occurs in the CE. This point will be discussed further via the potential distribution analysis in Section 6.4. The space charges generated near the CE during the electrochemical reaction change the potential distribution between the WE and CE, and then cause the narrowing of the cathodic part of the voltammogram.

As previously mentioned, the magnitude of the current peaks increased and then stabilized after sweeping the sample more than 10 times, 10 V to -10 V to 10 V. This builds up the charge. The sample was placed in the lab at room temperature and ambient pressure for 25 days after the measurement. After 25 days, a single 10 V to -10 V to 10 V voltage sweep was performed, and the two current peaks are shown in Fig. 6.12(a). We now explore the space charge build-up process. The sample's WE was biased at -4 V and at +4 V vs. CE for 30 min, respectively, and in sequence. Cyclic voltammograms were recorded and plotted, in Figs. 6.12(b) and 6.12(c) after the -4 V and the +4 V bias, respectively. While both cathodic and anodic peaks increase after the bias, the cathodic peak increase is larger (Fig. 6.12(c) vs. Fig 6.12(b)). Fick's laws of diffusion are considered to aid the explanation of this phenomenon. If a reaction continually occurs near an electrode surface, the reaction region increases. Both after the voltage sweep and voltage bias, the current peaks increase as the diffusion layer increases [45].

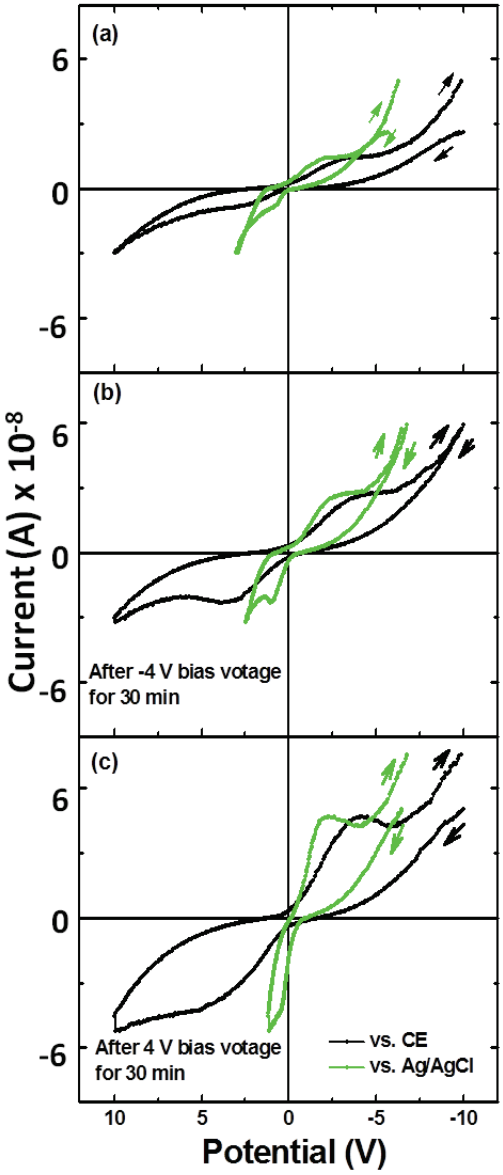

Figure 6.12: Voltammograms of a single crystal of (1a): (a) after 25 days in the lab at room temperature and ambient pressure, 1st sweep, (b) after -4 V bias voltage applied to the WE vs. CE for 30 min, 1st sweep, and (c) after 4 V bias voltage applied to the WE vs. CE for 30 min, 1st sweep. Shown are potential of the WE vs. CE, which is the potential sweep applied between the WE and CE (black dot plus line), and the potential of the WE vs. Ag/AgCl RE which is the potential measured between the WE and Ag/AgCl RE (green dot plus line). Current is measured between the WE and CE.

We also performed room temperature solid state electrochemical measurements on single crystal samples of compounds (1b) and (2). A representative cyclic voltammogram of compound (1b) is shown in Fig. 6.13, which is similar to that of compound (1a), Fig. 6.11. However, the potential difference between the cathodic and anodic peaks for (1b) is smaller than that of compound (1a). This is due to the unlike mixed oxidation states of vanadium in (1a) and (1b) which influence the electrochemical reactions differently.

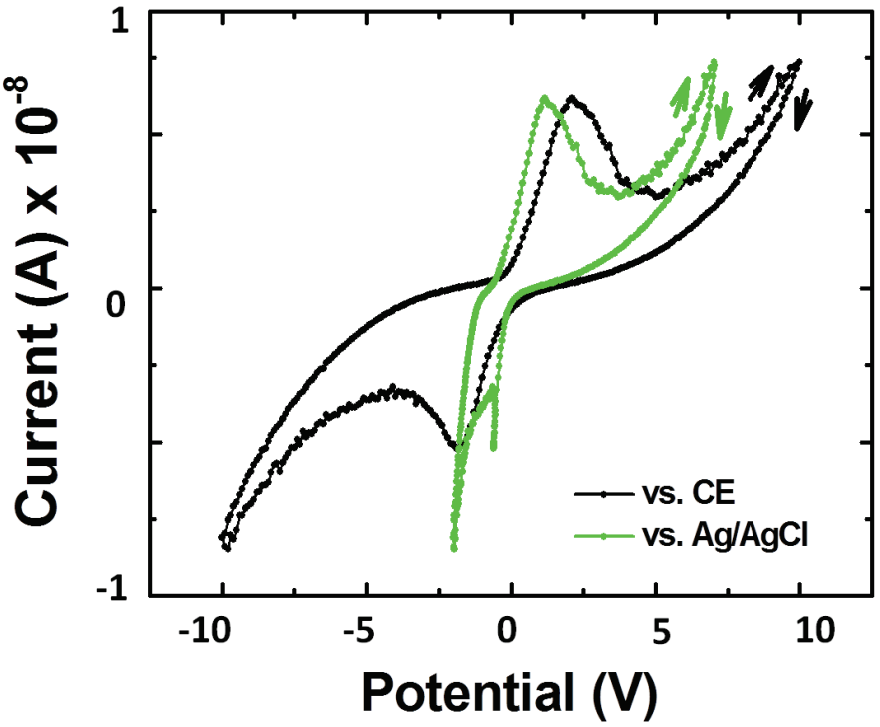

Figure 6.13: Voltammogram of a single crystal of (1b), 15th cycle: potential of the WE vs. CE, which is the potential sweep applied between the WE and CE (black dot plus line), and potential of the WE vs. Ag/AgCl RE, which is the potential measured between the WE and Ag/AgCl RE (green dot plus line). Current is measured between the WE and CE.

For compound (2), the cyclic voltammograms yielded smaller current values than those of the compounds (1a) and (1b), with no noticeable current peaks. We note that the conductivity value of (2) was too low to be reliably measured by DC resistivity measurements, although AC resistivity value may be extrapolated from the impedance data shown in Fig. 6.23. The different electrochemical behavior of compounds (1a), (1b), (1c), and (2) can be understood on the basis of distinct mechanisms of solid-state and solution-state electrochemistry. The electrochemical reaction occurs at the interface between the electrodes and electrolytes. The electrode reaction rate is determined by the mass transfer in the electrolyte, the electron transfer at the electrode surface and the electrochemical reaction at the interface. The current magnitude is limited by the slowest step(s), the rate-determining step(s) [45]. The current is driven by an overpotential η, which is the polarization of the applied potential over the equilibrium potential of the electrochemical cell. If we consider the electrode reaction process as a series of resistances representing the different steps, the overpotential can be represented as the sum of potential drops over these resistances. As shown in Fig. 6.14, η_{mt} and R_{mt} represent the overpotential and resistance of the mass transfer term; η_{ct} and R_{ct} represent the charge transfer term; and η_{er} and R_{er} represent the electrochemical reaction term. The magnitude of the resistance for a fast reaction step is smaller than the one for a slow step. In solution state electrochemistry, mass transfer is relatively fast via the movement of the reactant in the electrolyte by migration, diffusion and convection. On the contrary, mass transfer in a solid-state electrolyte is much slower and becomes the rate-determining step in solid state electrochemistry. Mass transfer in a solid state electrolyte is harder. Therefore, the mass transfer step is the most important rate-determining step in solid state electrochemistry. When the mass transfer rate is very slow, then electrochemical behavior is hard to observe, for example in compound (2). The mass transfer mechanism of compounds (1a), (1b) and (1c), in which the NH_4^+

ions are assumed to play an important role, is still an open question, and with these compounds, electrochemical behavior is observed.

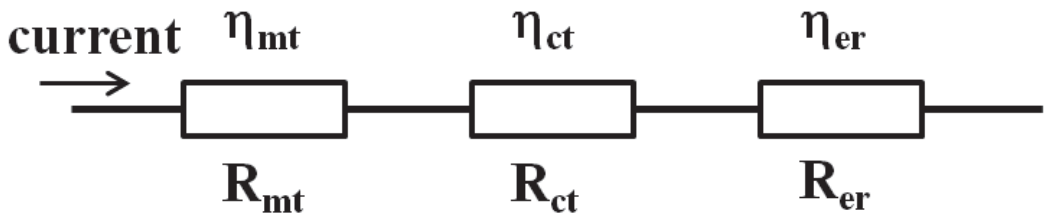

Figure 6.14: The electrode reaction process represented as a series of resistances [45]. R_{mt}, R_{ct} and R_{er} are the resistances, and η_{mt}, η_{ct} and η_{er} are the overpotentials dropped on the resistances, for the mass transfer term (mt), the charge transfer term (ct), and the electrochemical reaction term (er), respectively.

A variable temperature solid state electrochemical study of compound (1a) was performed in the home-built quartz tube variable temperature system, and the sample contacted in a 2-point geometry. We repeated the 10 V to -10 V to 10 V voltage sweep between the WE and CE more than 10 times until the magnitude of the current peaks stabilized at room temperature. Cyclic voltammograms with potential of the WE vs. CE were obtained, with the temperature increment around 5 K and waiting time around 15 min, from room temperature up to 370 K using the Keithley 2400 source meter. As shown in Fig. 6.15(a), the potential difference of the cathodic and anodic peaks decreases as the temperature increases from 298 K to 313 K. The two current peaks decrease in magnitude after 319 K, as shown in Fig. 6.15(b), and nearly disappear after 338 K. After the variable temperature measurement, the sample was slowly cooled down to room

temperature, with time duration over one hour. A cyclic voltammogram was obtained again. The current was too small to be detected indicating an extremely small conductivity. One more measurement was performed after leaving the sample in the lab at room temperature and ambient pressure for 10 days. No recovery of current peaks was observed, indicating an irreversible process had occurred during the high temperature.

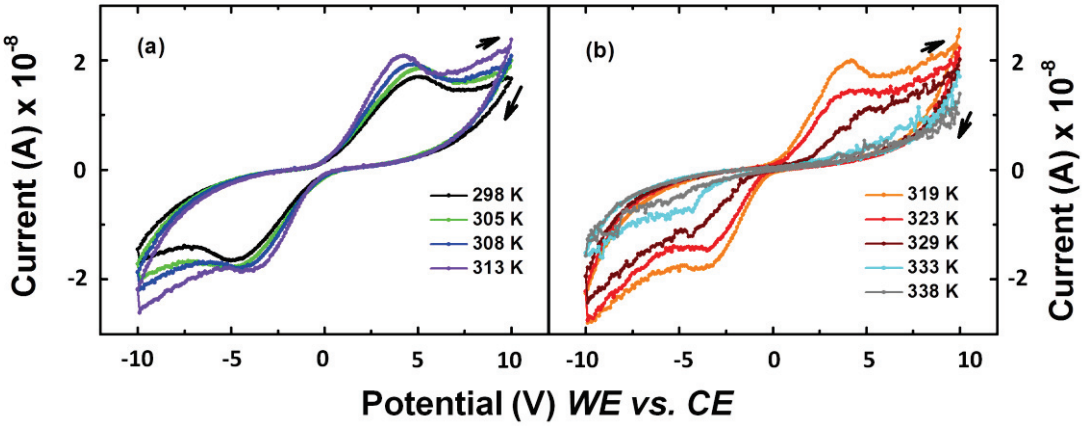

Figure 6.15: Variable temperature voltammograms of a single crystal of (1a): (a) from 298 K to 313 K, and (b) from 319 K to 338 K. Shown is potential of the WE vs. CE, which is the potential sweep applied between the WE and CE. At 298 K, the sample was cycled 10 times until a stable current peak was observed. All subsequent voltammograms at T > 298 K were always the 1st cycle after attaining a specific T.

6.4 Electric potential distribution analysis

A comprehensive analysis of the macroscopic electric potential distribution inside the crystal samples was performed to understand the solid state electrochemical measurements [47, 163]. We performed the electric potential distribution simulation using Wolfram Mathematica 8.0. The function ContourPlot was adopted to generate the equipotential lines. As detailed in section 6.3,

the physical picture has a single crystal contacted with 4 electrodes, 3 of which function as the WE, CE and the PRE, and the crystal itself is the electrolyte. Electrochemical reactions occur in the solid electrolyte with space charges generated at the microscale, while the net charge, and hence net space charge, inside the electrolyte is 0 at the macroscale. So the electric potential inside the electrolyte obeys Laplace's equation:

$$\nabla^2 \Phi = 0 \tag{6.1}$$

where Φ is the electric potential. The electric field $E = -\nabla \Phi$ is of course perpendicular to the equipotential lines everywhere. The electrodes are assumed metallic, while compounds (1a), (1b) and (1c) behave as semiconductors with comparatively low conductivity values. So, during the solid state electrochemical measurement, at the electrode surfaces, the electric current flows into and out of the crystal in the direction normal to the crystal/electrode interface. At any other surfaces, there is no electric current flow normal to the crystal surface. The current density vector is proportional to the electric field vector in our case. This means that the electric field is normal to the electrode surfaces, and tangential to all the other crystal surfaces. So, Laplace's equation is furnished with the following boundary conditions relating to the electric field:

$E_{\parallel} = n_{\parallel} \cdot \nabla \Phi = 0$ at the electrode surfaces (6.2)

$E_{\perp} = n_{\perp} \cdot \nabla \Phi = 0$ at any other surfaces (6.3)

We have developed a model to calculate the potential distribution in a single crystal with the WE, CE and PRE schematically presented as in Fig. 6.16, where we show a cross section of the crystal (white square) with four microscale electrodes. In the measurements, the potential between the

WE and the CE is cycled from 10 V to -10 V to 10 V. Laplace's equation is solved imposing boundary conditions expressed in equations 6.2 and 6.3, using the approach schematically depicted in Fig. 6.16. We start with a crystal (white square) and then the surfaces of the crystal without electrodes are used as mirror symmetry planes and we generate the grey shaded areas (to the right and to the left) that mirror the contours in the crystal (Fig. 6.16). After this operation, the equipotential contours are perpendicular to the surface of the crystal as shown in Fig. 6.16 and satisfy the boundary condition in Equation 6.3. During the potential distribution analyses, only the potential distribution inside the single crystal is considered.

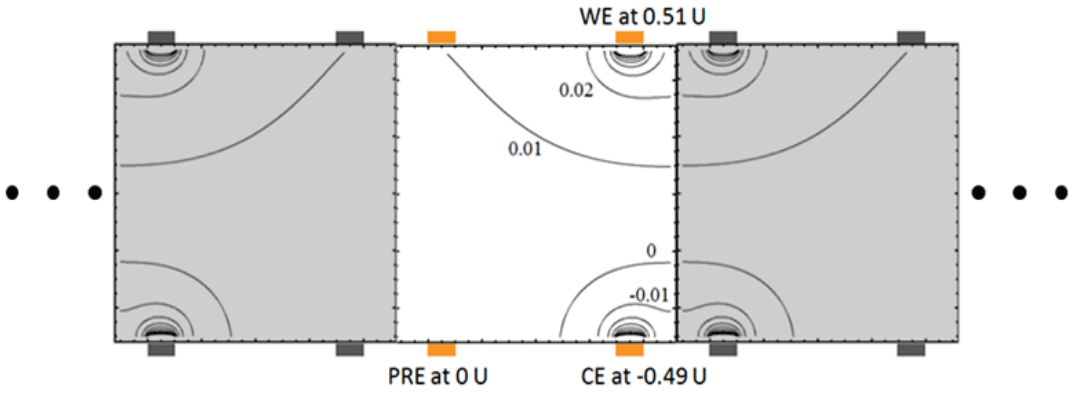

Figure 6.16: Schematic of the model used in the generation of the distribution of equipotential contours. In the middle of the figure, we have a single crystal of e.g. compound (1a). The 3 electrodes used for electrochemistry are denoted, as well as the potential at which these 3 electrodes are held. To the right and left of the crystal, we show mirror images (shaded grey) of the equipotential contours in the crystal, to artificially create boundary conditions that are equivalent to the boundary conditions discussed in the text. In fact, we have many more of these mirror images progressing to the right and left, indicated by dots.

The electric potential is calculated by Poisson's equation:

$$\nabla^2 \Phi = -\rho/\varepsilon \tag{6.4}$$

where ρ is charge density and ε is permittivity (product of vacuum permittivity and dielectric constant). Inside the crystal electrolyte, there is no net charge density and ρ equals 0. Considering the geometry in Fig. 6.16, the function for the electric potential was obtained from the following equation:

$$\iint \frac{1}{4\pi\varepsilon} \frac{\rho}{\sqrt{(xx-x)^2+(yy-y)^2}} \, dx \, dy \tag{6.5}$$

where x and y are the horizontal and vertical coordinates, respectively. The permittivity is unknown for our condition, and therefore a tentative constant was used to represent $\frac{\rho}{4\pi\varepsilon}$. We integrated the equation for all areas in our model with Mathematica to obtain a potential distribution function with xx and yy as variable coordinates. An example simulation result is shown in Fig. 6.17, where a cross section of a crystal and relative arrangement of the WE, CE and PRE electrodes are indicated and are the same as in Fig. 6.16, and in Fig. 6.17(b), equipotential contours for the following situation generated. The potential of the counter electrode (CE) was set to 0 U. By definition, the potential difference between the WE and the CE equals U, which is in our simulations, the unit of potential difference. U can represent any voltage value between 10 V to -10 V, following the actual potential sweeps from 10 V to -10 V back to 10 V. The Mathematica function ContourPlot was used to plot the potential distribution (Fig. 6.17(b)). We note that the potential gradient is greater near the WE and CE due to the small (micro) size of the electrodes compared to the sample dimensions, while the potential gradient is small in the region where the

PRE is located. In this simulation, with the CE at 0 U, the CE is effectively functioning as a reference electrode, and we obtain the potential at the PRE to be 0.49 U. As mentioned earlier, from experimental measurements, we find that our Ag epoxy PRE is at ~ -0.1 V vs. the standard Ag/AgCl RE, and because the difference is small, we assume that the value of the potential at the WE in all our simulations (and also in our experimental data) to be the value versus the standard, Ag/AgCl RE, and we denote as such in all our figures.

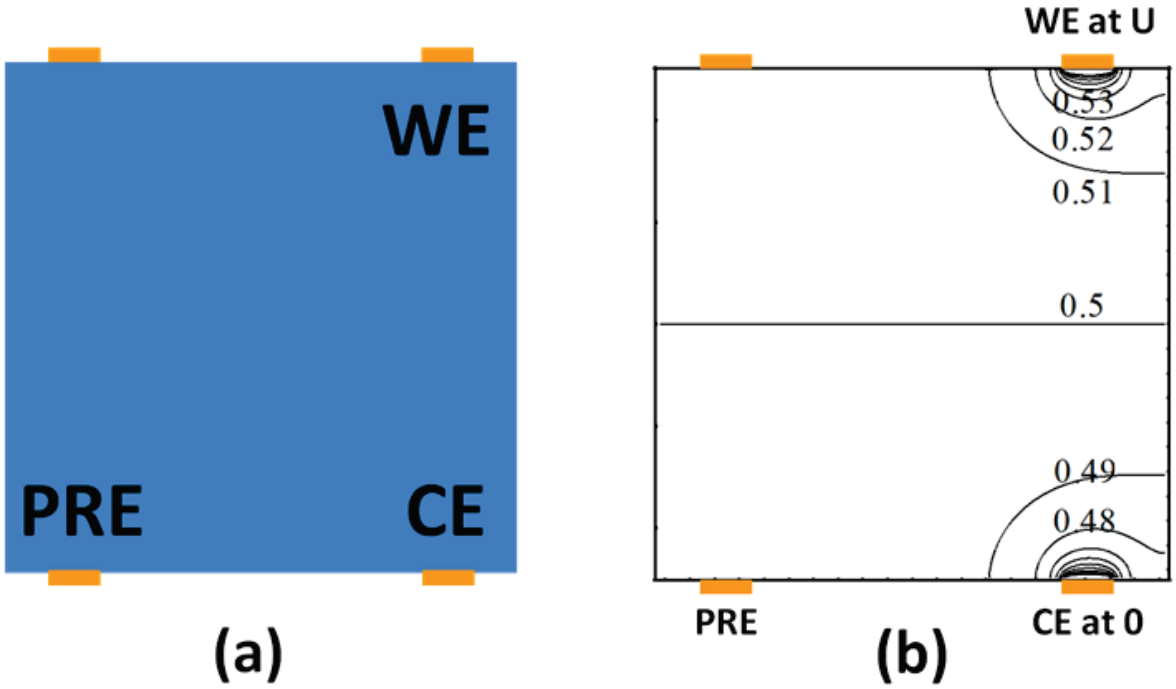

Figure 6.17: (a) The cross section of a single crystal with 4 micro size electrodes and the relative arrangement of the WE, CE and PRE. (b) Potential distribution in the cross section of the single crystal in Fig. 6.17(a) with the potential at CE set to 0 U and that of the WE to U. Shown are the equipotential contours.

We now vary the parameters of the simulation to represent a typical solid state electrochemical data recorded on our sample, for example the voltammogram of Fig. 6.11. As indicated in Fig. 6.11, we simultaneously measure the WE vs. the CE and the WE vs. the Ag/AgCl RE. For the simulation, now we set the potential of the PRE to 0 V (or as indicated in Fig. 6.18(a) to 6.18(c), PRE at 0 U), and force it to function as the reference electrode, and generate equipotential contours of the WE vs. the CE. In all the panels of Fig. 6.18, the actual 0 V equipotential contour, which should end at the PRE, is not shown. Shown is the ~0 V equipotential contour. The experimental potential cycles are swept +10 V to -10 V to +10 V. In Fig. 6.11, when the potential of the WE vs. CE (and also the potential of the WE vs. RE) is small and close to 0 V, e.g. -0.5 V < V < +0.5 V, no electrochemical process is observed. This situation is simulated and the result shown in Fig. 6.18(a), where the potential of the WE and the CE are roughly the same in magnitude, in units of U. When the potential of the WE is larger than +/- 0.5 V, electrochemical processes are observed, Figs. 6.18(b) and 6.18(c). During the voltage sweep between the WE and CE, for positive values of the voltage, the WE is at a higher potential than the CE and the electrochemical reaction occurs at the WE. In our simulations, to mimic the relative positive potential of the WE, we add positive charges to the electrode region, shown as red crosses in Fig. 6.18(b). The potential of the WE is further increased to about +0.75 U, resulting in the potential of the CE to be -0.25 U, and generate the equipotential contours shown in Fig. 6.18(b), for U >> 0. To complete the electrochemical cycle, the potential of the WE vs. CE decreases, and we simulate this situation by adding positive charges to the CE electrode region, shown as red crosses in Fig. 6.18(c). We note that here U << 0, and effectively the CE is now functioning as the WE and the electrochemical reaction takes place at the CE. With the WE at +0.25 U, the CE is at -0.75 U, the equipotential contours are generated as shown in Fig. 6.18(c). The value of the potential of the WE, in Fig. 6.18(c), is smaller than that in Fig. 6.18(a),

and this difference contributes to the narrowing of the cathodic current peaks in the voltammogram of the potential of the WE vs. Ag/AgCl, as shown in Figs. 6.11, 6.12 and 6.13. Our simulations capture the solid state electrochemical processes occurring in our samples, correctly indicate regions of higher potential gradient at different values of the potential of the WE, support the substitution of our Ag paste PRE in place of an Ag/AgCl standard RE, and provide an explanation for the observed narrowing of the cathodic current peak.

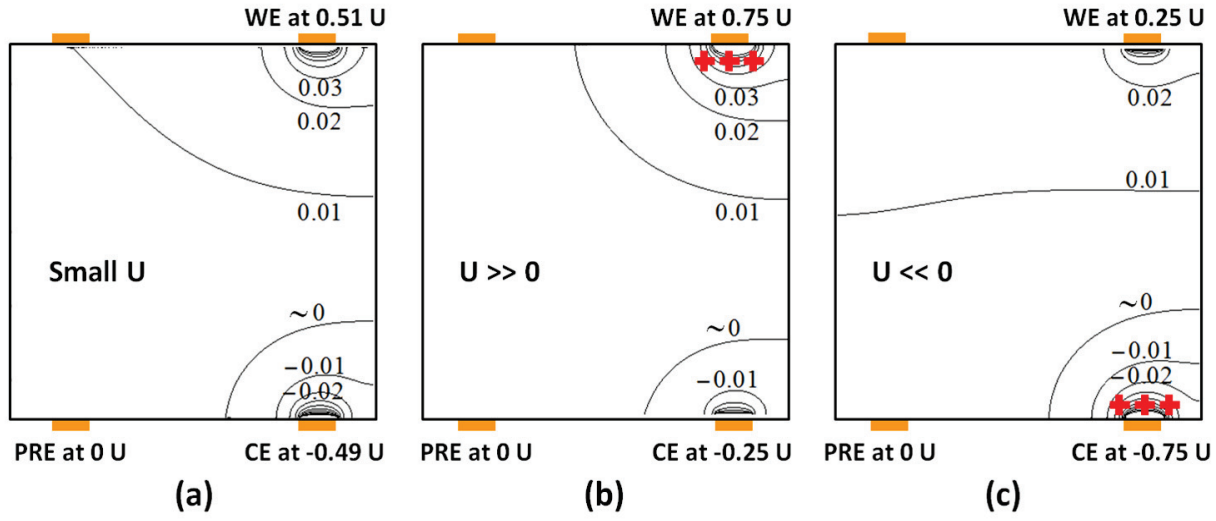

Figure 6.18: Equipotential contours for the following 3 different situations, with the with PRE potential set at 0 U:(a) no electrochemical reaction occurs, (b) electrochemical reaction occurs at the WE when U >> 0, and (c) electrochemical reaction occurs at the CE when U << 0. Positive charges (red crosses) are added to the WE in Fig. 6.18(b), and to the CE in Fig. 6.18(c) to simulate the relative potential difference between the WE and the CE. These simulations mimic the actual cyclic voltammogram sweeps.

6.5 Variable temperature AC electrical characterization

We performed AC studies on single crystals of compounds (1a), (1b), (1c) with ammonium cation, and (2) with sodium cation, where the chosen crystals were roughly the same size as those used in the solid state electrochemistry study. Two electrodes were fabricated on each single crystal sample with EPO-TEK H20E conductive silver epoxy. Variable temperature impedance spectroscopy measurements [46, 95, 96, 164] were performed in the home-built quartz tube variable temperature system with a Perkin–Elmer 7225 DSP lock-in amplifier. Each temperature setting was obtained after a time duration of 30 min, and at each T, the duration of the measurement was 1 hour.

For compound (1a), data was obtained in the temperature range 297-357 K with a temperature increment of ~10 K. The measurement was performed in the frequency range 0.01-50000 Hz sweeping from low frequency to high frequency with a constant voltage of 1 V applied. The representative Cole-Cole plots are plotted in Fig. 6.19, which consist of two contributions, related to the two semi-circles indicated – one at low frequencies, the other one at high frequencies – are observed. The semi-circle at low frequencies is more pronouncedly formed as the temperature increases from 297 K to 318 K, and then vanishes as the temperature increases from 318 K to 357 K. At 357 K, only a semi-circle at high frequencies is obtained. We also observe a deviation, an increase in the complex part of the impedance at low frequencies, which is attributed to contact behavior. An equivalent circuit model, depicted in Fig. 6.20, is used to simulate the Cole-Cole plots of Fig. 6.19. It consists of two blocks, each formed by a capacitor and resistor in parallel, corresponding to the high frequency semi-circle and the low frequency semi-circle, respectively. Two different electrochemical reactions between vanadium ions in different oxidation states (V^{2+}/V^{3+} and V^{3+}/V^{4+}) are responsible for these two blocks. The charge

separation of the space changes created by the two different electrochemical reactions forms the two capacitances (C_1 and C_2), and electrochemical leakage corresponding to the two electrochemical reactions constitutes the two resistances (R_1 and R_2) [109, 164]. The resistance (R_{series}) in series with the two blocks is from the contacts. R_1 and R_2 at each temperature could be extracted as the diameter of the two semi-circles depicted. Both R_1 and R_2 decrease as the temperature increases indicates semiconducting behavior.

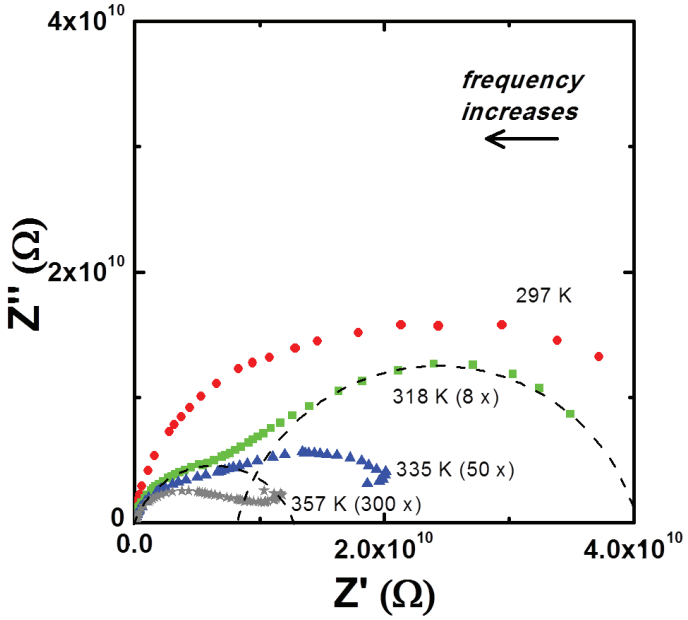

Figure 6.19: Cole-Cole plots of (1a) at various temperatures. For the trace at 318 K, 2 semi-circles (dash line) are drawn through the experimental points to guide the eye. As indicated, the frequency increases from right to left in the figure. To better represent the data, some of the traces are multiplied by an appropriate factor.

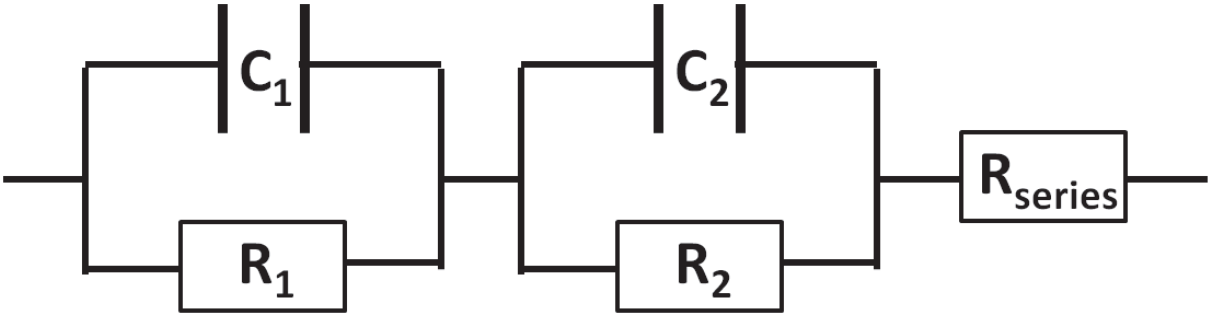

Figure 6.20: The equivalent circuit for a single crystal of compounds (1a), (1b) and (1c) with 2 silver electrodes. C_1 and C_2 are the capacitances formed by electrochemical reaction; R_1 and R_2 are the resistances from electrochemical leakage; R_{series} is the contact resistance in series.

The Cole-Cole plots of compounds (1b) and (1c) were obtained in the temperature range 298-358 K and 298-445 K with a temperature increment of ~10 K, and heating procedure as for compound (1a). The measurements were performed in the frequency range 0.01-50000 Hz for (1b) and 0.1-50000 Hz for (1c). A constant voltage of 1 V is applied for each measurement. We observe similar trend in the Cole-Cole plots for compound (1a), (1b) and (1c), Figs. 6.19, 6.21 and 6.22, respectively. Thus, the AC electrical behaviors of (1b) and (1c) may also be explained by the equivalent circuit in Fig. 6.20. However, as the mixed valence states of vanadium ions are different in compounds (1a), (1b) and (1c), the observed two semi-circles in the Cole-Cole plots are not identical. For (1b), the most pronounced low frequency semi-circle occurs at 336 K, a little bit higher than that observed for (1a) which is at 318 K. For (1c), the Cole-Cole plots are more influenced by the contact resistance than for (1a) and (1b), and we observe deviations at the low frequencies.

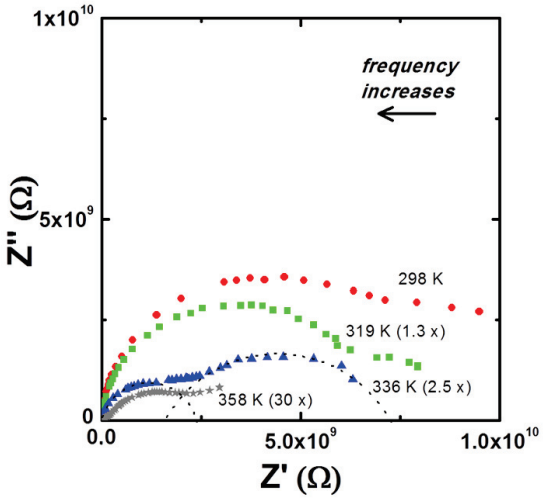

Figure 6.21: Cole-Cole plots of (1b) at various temperatures. For the trace at 336 K, 2 semi-circles (dash line) are drawn through the experimental points to guide the eye. As indicated, the frequency increases from right to left in the figure. To better represent the data, some of the traces are multiplied by an appropriate factor.

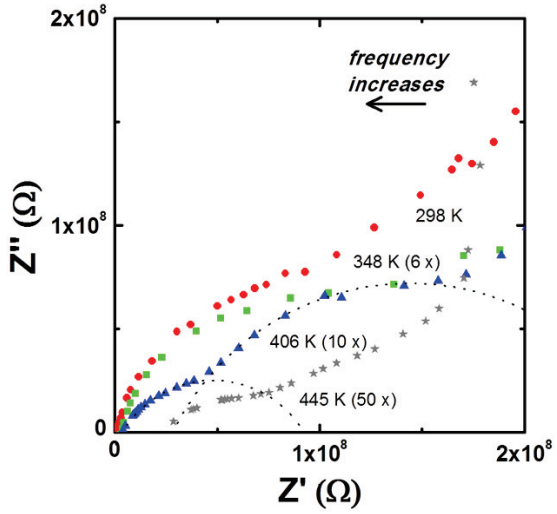

Figure 6.22: Cole-Cole plots of (1c) at various temperatures. For the trace at 406 K, 2 semi-circles (dash line) are drawn through the experimental points to guide the eye. As indicated, the frequency increases from right to left in the figure. To better represent the data, some of the traces are multiplied by an appropriate factor.

Variable temperature impedance spectroscopy measurements were also performed on compound (2) with sodium cations, for comparison. The measurements were performed in the temperature range 297-457 K with a temperature increment of ~10 K, and in the frequency range 0.01-50000 Hz at each temperature. A larger constant voltage, 5 V, than that used in the AC measurements of compounds (1a), (1b) and (1c) was applied to compound (2) to obtain a measurable current, given the high resistance of (2). Representative Cole-Cole plots are shown in Fig. 6.23. Only one semi-circle is observed at all temperatures and as the temperature increases, the semi-circle becomes more pronounced. At temperatures higher than 372 K, a small semi-circle with a negative imaginary part for the impedance is observed at low frequencies. This is an inductive semi-circle caused by the inductance of the contacts [165]. Figure 6.24 shows an equivalent circuit for compound (2), where C is the capacitance formed by the two contacts, R is the resistance of crystal from the electronic conduction, and L is the inductance from the relaxation process of the contacts. No contact resistance is observed, because the magnitude of the resistance of compound (2) is very large and thus dominates the measured values. The resistance is measured from the diameter of the semi-circle at high frequencies, and it decreases as the temperature increases indicating a semiconducting behavior.

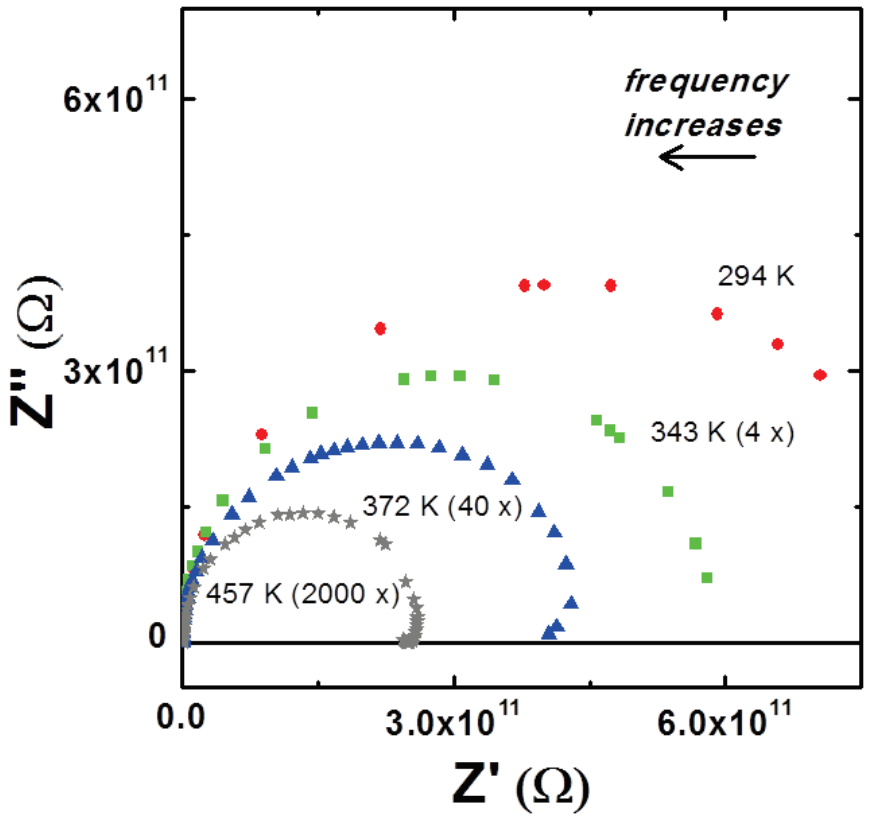

Figure 6.23: Cole-Cole plots of (2) at various temperatures. As indicated, the frequency increases from right to left in the figure. To better represent the data, some of the traces are multiplied by an appropriate factor.

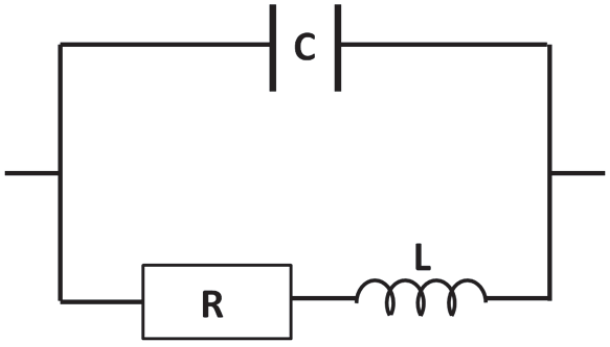

Figure 6.24: The equivalent circuit for a single crystal of compound (2) with 2 silver epoxy electrodes. C is the capacitance formed by the contacts; R is the resistance of the crystal; L is the inductance formed by the contacts.

6.6 Conclusion

We investigate the structural and electrochemical properties of two hydrothermally synthesized cryolite-type compounds, $(NH_4)_3V_xGa_{1-x}F_6$, and Na_3VF_6. The room temperature crystal structures are re-determined by single crystal x-ray diffraction. $(NH_4)_3V_xGa_{1-x}F_6$ crystals with different ratio x have crystallized in the same cubic space group *Fm3m*. The structure of Na_3VF_6 is solved in the monoclinic $P2_1/n$ space group. The higher symmetry structure of $(NH_4)_3V_xGa_{1-x}F_6$ vs. Na_3VF_6 could be explained by the size and the tetragonal geometry of the ammonium ions. The electrochemical behavior of $(NH_4)_3V_xGa_{1-x}F_6$ is observed in both the solid and the solution states. Electrical potential distribution analysis is performed to explain the solid state electrochemical data. The narrowing of the current peak is attributed to the electrical potential distribution change induced by the space charge deposition during the electrochemical reaction. The AC electrical properties of $(NH_4)_3V_xGa_{1-x}F_6$ and Na_3VF_6 are also compared with impedance spectroscopy. The occurrence of electrochemical reactions in $(NH_4)_3V_xGa_{1-x}F_6$ is detected by the observation of two semi-circles in the Cole-Cole plots. In contrast, for Na_3VF_6, we only observe a single circle in the Cole-Cole plot.

Chapter 7 Conclusion

Although the materials under investigation in this dissertation are varied, they share two common features: they are all transition metal compounds, and they have potential usage in electrical energy storage. The demands for the next generation energy storage devices are growing. Finding a promising material plays an important role in the development of new energy storage devices and is a key issue for future energy storage systems. Transition metal compounds with outstanding energy storage capability have received considerable attention due to their electrical and electrochemical properties. This dissertation reports our developments in researching some transition metal compounds related to their potential application of energy storage.

The first material system that is presented in this dissertation is a nanostructured vanadium oxide. This material is hydrothermally synthesized to be a quasi-spherical three-dimensional object with folded nanosheets. Variable temperature DC electrical measurements indicate a semiconducting behavior; the conductivity increases as the temperature increases. With the material functioning as an electrode, we performed a comparative study of the electrochemical behavior in chloride solutions of Li^+, Na^+, K^+ and NH_4^+ ions respectively, aimed at finding an alternative choice of charge carrier other than the commonly used Li^+ ion. Cyclic voltammetry measurements were performed at room temperature and the adsorbed specific charge calculated. Morphological characteristics were studied both before and after cyclic voltammograms were obtained, using scanning electron microscopy. Increased specific charge and minimal morphological degradation were observed as a function of cycle number in the case of Na^+ and NH_4^+ ions, and a favorable specific charge of 180 mAh g^{-1} was obtained for the NH_4^+ ion. The results suggest that the nanostructured vanadium oxide material is a viable electrode material candidate for energy storage

applications coupled with Na^+ and NH_4^+ ions are potential charge carriers in the vanadium reduction/oxidation processes.

The second material system presented discusses the ionic and electronic properties of an oxo-vanadium arsenate $[(As_6V_{15}O_{51})^{-9}]_\infty$ and an oxo-vanadium phosphate $[(P_6V_{15}O_{51})^{-9}]_\infty$. These two compounds are zeolite-like materials with porous structures delineated by their three-dimensional frameworks. The high specific surface areas the porous structures provide may offer large electrical storage capabilities. The comparative study of the electrical properties of these two zeolite-like frameworks was performed as a function of temperature and various extra-framework constituents by both DC and AC methods. Both electronic conduction from the framework and ionic conduction from the extra-framework constituents were observed in the oxo-vanadium arsenate. In the case of the oxo-vanadium phosphate, only ionic conduction was observed. In the former, the electronic conduction influenced the ionic conduction with a slightly stronger than exponential increase of the ionic conductivity as a function of temperature. The mixed electrical conduction of the oxo-vanadium arsenate framework allows its potential utility in energy applications.

The third material system presented involves a hydrothermally synthesized strontium manganese vanadate framework. Manganese vanadate layers connected with strontium sites form a layered structure. A structural change in the temperature range 675 to 775 K is observed both in the TGA and single crystal XRD analysis, which is due to the loss of water from the μ_3-OH_2 and μ_4-OH sites. The crystal structure after a heat treatment higher than 775 K is similar to that of a strontium manganese arsenate framework under investigation. By investigating the conductivity properties as a function of temperature, it is evident that the strontium manganese vanadate framework has

anisotropic protonic conductivity in various crystal directions that vanished after the structural change at high temperature with only a much smaller electronic conductivity detected.

The last material system of this dissertation reports two hydrothermally synthesized cryolite-type compounds, $(NH_4)_3V_xGa_{1-x}F_6$ and Na_3VF_6. The crystal structures are cubic *Fm3m* for the former and monoclinic $P2_1/n$ for the latter at room temperature determined by single crystal x-ray diffraction. The structural difference of the two is attributed to the difference in size between the sodium and ammonium ions, and to the hydrogen bonding capability of the ammonium ion. Previous research on transition metal compounds in the energy storage application largely focused on their properties as electrode materials. Here, we also study specific transition metal compounds as potential solid state electrolyte material. As example, we studied the electrochemical properties of $(NH_4)_3V_xGa_{1-x}F_6$, with different values x, by performing cyclic voltammetry measurements on single crystals, and compared the results with electrochemical data on solutions of the solids dissolved in water. Remarkable electrochemical behaviors were observed on both the solid state and solution state. Electrical potential distribution analyses were performed to aid the understanding of the solid state cyclic voltammograms. Further, results of impedance spectroscopy support electrochemical reaction in the solid state. The results demonstrated suggest the potential of using transition metal fluorides as solid electrolytes, offering new directions for all solid state energy storage systems.

Bibliography

[1] E. A. Parson, and D. W. Keith, "Fossil fuels without CO_2 emissions" *Science* **282**, 1053 (1998).

[2] R. E. Sims, H.-H. Rogner, and K. Gregory, "Carbon emission and mitigation cost comparisons between fossil fuel, nuclear and renewable energy resources for electricity generation" *Energy policy* **31**, 1315 (2003).

[3] N. S. Lewis, and D. G. Nocera, "Powering the planet: Chemical challenges in solar energy utilization" *Proc. Natl. Acad. Sci. U.S.A.* **103**, 15729 (2006).

[4] P. Denholm, G. L. Kulcinski, and T. Holloway, "Emissions and energy efficiency assessment of baseload wind energy systems" *Environ. Sci. Technol.* **39**, 1903 (2005).

[5] D. R. Rolison, and L. F. Nazar, "Electrochemical energy storage to power the 21st century" *MRS Bull.* **36**, 486 (2011).

[6] A. J. Cavallo, "Energy storage technologies for utility scale intermittent renewable energy systems" *J. Sol. Energy Eng.* **123**, 387 (2001).

[7] G. E. Moore, "Cramming more components onto integrated circuits" *Electronics* **38**, 114 (1965).

[8] M. Winter, and R. J. Brodd, "What are batteries, fuel cells, and supercapacitors?" *Chem. Rev.* **104**, 4245 (2004).

[9] A. Burke, "Ultracapacitors: why, how, and where is the technology" *J. Power Sources* **91**, 37 (2000).

[10] H. I. Becker, "Low voltage electrolytic capacitor" *U.S. Patent 2800616*, (1957).

[11] Y. Hou, L. Chen, P. Liu, J. Kang, T. Fujita, and M. Chen, "Nanoporous metal based flexible asymmetric pseudocapacitors" *J. Mater. Chem. A*, (2014).

[12] T. Liu, L. Finn, M. Yu, H. Wang, T. Zhai, X. Lu, Y. Tong, and Y. Li, "Polyaniline and polypyrrole pseudocapacitor electrodes with excellent cycling stability" *Nano Lett.* **14**, 2522 (2014).

[13] R. F. Service, "New 'supercapacitor' promises to pack more electrical punch" *Science* **313**, 902 (2006).

[14] P. Simon, and Y. Gogotsi, "Materials for electrochemical capacitors" *Nat. Mater.* **7**, 845 (2008).

[15] H. D. Yoo, E. Markevich, G. Salitra, D. Sharon, and D. Aurbach, "On the challenge of developing advanced technologies for electrochemical energy storage and conversion" *Mater. Today* **17**, 110 (2014).

[16] B. L. Ellis, K. T. Lee, and L. F. Nazar, "Positive electrode materials for Li-ion and Li batteries†" *Chem. Mater.* **22**, 691 (2010).

[17] F. Sauvage, J. M. Tarascon, and E. Baudrin, "In situ measurements of Li-ion battery electrode material conductivity: Application to Li_xCoO_2 and conversion reactions" *J. Phys. Chem. C* **111**, 9624 (2007).

[18] M. Broussely, F. Perton, P. h. Biensan, J. M. Bodet, J. Labat, A. Lecerf, C. Delmas, A. Rougier, and J. P. Peres, "Li_xNiO_2, a promising cathode for rechargeable lithium batteries"

J. Power Sources **54**, 109 (1995).

[19] C. C. Hu, K. H. Chang, M. C. Lin, and Y. T. Wu, "Design and tailoring of the nanotubular arrayed architecture of hydrous RuO_2 for next generation supercapacitors" *Nano Lett.* **6**, 2690 (2006).

[20] S. Chen, J. Zhu, X. Wu, Q. Han, and X. Wang, "Graphene oxide - MnO_2 nanocomposites for supercapacitors" *ACS nano* **4**, 2822 (2010).

[21] J. W. Lee, T. Ahn, J. H. Kim, J. M. Ko, and J. D. Kim, "Nanosheets based mesoporous NiO microspherical structures via facile and template-free method for high performance supercapacitors" *Electrochim. Acta* **56**, 4849 (2011).

[22] W. Zhang, F. Liu, Q. Li, Q. Shou, J. Cheng, L. Zhang, B. J. Nelson, and X. Zhang, "Transition metal oxide and graphene nanocomposites for high-performance electrochemical capacitors" *Phys. Chem. Chem. Phys.* **14**, 16331 (2012).

[23] W. Deng, X. Ji, Q. Chen, and C. E. Banks, "Electrochemical capacitors utilising transition metal oxides: an update of recent developments" *RSC Advances* **1**, 1171 (2011).

[24] X. Zhao, B. M. Sánchez, P. J. Dobson, and P. S. Grant, "The role of nanomaterials in redox-based supercapacitors for next generation energy storage devices" *Nanoscale* **3**, 839 (2011).

[25] R. Liu, J. Duay, and S. B. Lee, "Heterogeneous nanostructured electrode materials for electrochemical energy storage" *Chem. Commun.* **47**, 1384 (2011).

[26] D. Sun, C. W. Kwon, G. Baure, E. Richman, J. MacLean, B. Dunn, and S. H. Tolbert, "The

relationship between nanoscale structure and electrochemical properties of vanadium oxide nanorolls" *Adv. Funct. Mater.* **14**, 1197 (2004).

[27] V. Soghomonian, and J. J. Heremans, "Characterization of electrical conductivity in a zeolitelike material" *Appl. Phys. Lett.* **95**, 152112 (2009).

[28] Y. Zhou, and H. Qiao, "A novel organic–inorganic hybrid manganese vanadate with helical chains,$[C_3N_2H_{12}][Mn(V_4O_{12})(H_2O)_2]$" *Inorg. Chem. Commun.* **10**, 1318 (2007).

[29] S. L. Suib, "Structure, porosity, and redox in porous manganese oxide octahedral layer and molecular sieve materials" *J. Mater. Chem.* **18**, 1623 (2008).

[30] Y. Le Page, and P. Strobel, "Crystal structure of a new cesium manganese vanadium oxide, $Cs_3Mn_3V_4O_{16}$" *Inorg. Chem.* **21**, 620 (1982).

[31] S. O. Gutschke, M. Molinier, A. K. Powell, and P. T. Wood, "Hydrothermal Synthesis of Microporous Transition Metal Squarates: Preparation and Structure of $[CO_3(\mu_3\text{-}OH)_2(C_4O_4)_2]\cdot 3H_2O$" *Angew. Chem. Int. Ed. Engl.* **36**, 991 (1997).

[32] C. S. Cundy, and P. A. Cox, "The hydrothermal synthesis of zeolites: history and development from the earliest days to the present time" *Chem. Rev.* **103**, 663 (2003).

[33] V. G. Soghomonian, "Synthesis and characterization of oxo vanadium phosphate and phosphonate materials" *Chemistry - Dissertations*, 111 (1995).

[34] P. Shuk, and M. Greenblatt, "Hydrothermal synthesis and properties of mixed conductors based on $Ce_{1-x}Pr_xO_{2-\delta}$ solid solutions" *Solid State Ionics* **116**, 217 (1999).

[35] H. Zhao, and S. Feng, "Hydrothermal Synthesis and Oxygen Ionic Conductivity of

Codoped Nanocrystalline $Ce_{1-x}MxBi_{0.4}O_{2.6-x}$, M= Ca, Sr, and Ba" *Chem. Mater.* **11**, 958 (1999).

[36] C. Zhao, S. Feng, R. Xu, C. Shi, and J. Ni, "Hydrothermal synthesis and lanthanide doping of complex fluorides, $LiYF_4$, KYF_4 and $BaBeF_4$ under mildconditions" *Chem. Commun.*, 945 (1997).

[37] W. Ueda, D. Vitry, and T. Katou, "Crystalline MoVO based complex oxides as selective oxidation catalysts of propane" *Catal. Today* **99**, 43 (2005).

[38] K. Byrappa, and M. Yoshimura, "Handbook of hydrothermal technology" *William Andrew*, (2001).

[39] Agilent Technologies, "CrysAlisPro Software system, v1.171.36.28" *Agilent Technologies UK Ltd, Oxford, UK*, (2013).

[40] G. M. Sheldrick, "A short history of SHELX" *Acta Crystallogr., Sect. A: Found. Crystallogr.* **64**, 112 (2007).

[41] O. V. Dolomanov, L. J. Bourhis, R. J. Gildea, J. A. Howard, and H. Puschmann, "OLEX2: a complete structure solution, refinement and analysis program" *J. Appl. Crystallogr.* **42**, 339 (2009).

[42] A. Coats, and J. Redfern, "Thermogravimetric analysis. A review" *Analyst* **88**, 906 (1963).

[43] H. Kriegsmann, "Encyclopedia of Spectroscopy" *Z. Phys. Chem.* **195**, 282 (1996).

[44] H. C. Montgomery, "Method for measuring electrical resistivity of anisotropic materials" *J. Appl. Phys.* **42**, 2971 (1971).

[45] A. J. Bard, and L. R. Faulkner, "Electrochemical methods: fundamentals and applications " (second ed.) *John Wiley & Sons*, 148-416 (2001).

[46] M. Balkanski, "Microionics-Solid State Integrable Batteries" *North-Holland Publishing Company*, 173-195 (1991).

[47] S. B. Adler, B. T. Henderson, M. A. Wilson, D. M. Taylor, and R. E. Richards, "Reference electrode placement and seals in electrochemical oxygen generators" *Solid State Ionics* **134**, 35 (2000).

[48] S. B. Adler, "Reference electrode placement in thin solid electrolytes" *J. Electrochem. Soc.* **149**, E166 (2002).

[49] G. A. East, and M. A. Del Valle, "Easy-to-make Ag/AgCl reference electrode" *J. Chem. Educ.* **77**, 97 (2000).

[50] M. Armand, and J. M. Tarascon, "Building better batteries" *Nature* **451**, 652 (2008).

[51] J. M. Tarascon, and M. Armand, "Issues and challenges facing rechargeable lithium batteries" *Nature* **414**, 359 (2001).

[52] H. K. Song, K. T. Lee, M. G. Kim, L. F. Nazar, and J. Cho, "Recent progress in nanostructured cathode materials for lithium secondary batteries" *Adv. Funct. Mater.* **20**, 3818 (2010).

[53] S. Tepavcevic, H. Xiong, V. R. Stamenkovic, X. Zuo, M. Balasubramanian, V. B. Prakapenka, C. S. Johnson, and T. Rajh, "Nanostructured bilayered vanadium oxide electrodes for rechargeable sodium-ion batteries" *ACS nano* **6**, 530 (2012).

[54] S. Y. Hong, Y. Kim, Y. Park, A. Choi, N.-S. Choi, and K. T. Lee, "Charge carriers in rechargeable batteries: Na ions vs. Li ions" *Energy Environ. Sci.* **6**, 2067 (2013).

[55] B. L. Ellis, and L. F. Nazar, "Sodium and sodium-ion energy storage batteries" *Curr. Opin. Solid State Mater. Sci.* **16**, 168 (2012).

[56] A. Hayashi, K. Noi, A. Sakuda, and M. Tatsumisago, "Superionic glass-ceramic electrolytes for room-temperature rechargeable sodium batteries" *Nat. Commun.* **3**, 856 (2012).

[57] M. Pasta, C. D. Wessells, R. A. Huggins, and Y. Cui, "A high-rate and long cycle life aqueous electrolyte battery for grid-scale energy storage" *Nat. Commun.* **3**, 1149 (2012).

[58] M. Armand, F. Endres, D. R. MacFarlane, H. Ohno, and B. Scrosati, "Ionic-liquid materials for the electrochemical challenges of the future" *Nat. Mater.* **8**, 621 (2009).

[59] J. M. Pringle, P. C. Howlett, D. R. MacFarlane, and M. Forsyth, "Organic ionic plastic crystals: recent advances" *J. Mater. Chem.* **20**, 2056 (2010).

[60] D. H. C. Wong, J. L. Thelen, Y. Fu, D. Devaux, A. A. Pandya, V. S. Battaglia, N. P. Balsara, and J. M. DeSimone, "Nonflammable perfluoropolyether-based electrolytes for lithium batteries" *Proc. Natl. Acad. Sci. U.S.A.* **111**, 3327 (2014).

[61] D. T. Hallinan, and N. P. Balsara, "Polymer Electrolytes" *Annu. Rev. Mater. Res.* **43**, 503 (2013).

[62] W. Li, J. R. Dahn, and D. S. Wainwright, "Rechargeable lithium batteries with aqueous electrolytes" *Science* **264**, 1115 (1994).

[63] W. Dong, D. R. Rolison, and B. Dunna, "Electrochemical properties of high surface area vanadium oxide aerogels" *Electrochem. Solid-State Lett.* **3**, 457 (2000).

[64] C. Wu, Z. Hu, W. Wang, M. Zhang, J. Yang, and Y. Xie, "Synthetic paramontroseite VO_2 with good aqueous lithium-ion battery performance" *Chem. Commun.*, 3891 (2008).

[65] S. Wang, Z. Lu, D. Wang, C. Li, C. Chen, and Y. Yin, "Porous monodisperse V_2O_5 microspheres as cathode materials for lithium-ion batteries" *J. Mater. Chem.* **21**, 6365 (2011).

[66] C. V. S. Reddy, S. A. Wicker, E. H. Walker, Q. L. Williams, and R. R. Kallurub, "Vanadium oxide nanorods for Li-ion battery applications" *J. Electrochem. Soc.* **155**, A599 (2008).

[67] X. Li, W. Li, H. Ma, and J. Chen, "Electrochemical lithium intercalation/deintercalation of single-crystalline V_2O_5 nanowires" *J. Electrochem. Soc.* **154**, A39 (2007).

[68] Y. Wang, K. Takahashi, K. H. Lee, and G. Z. Cao, "Nanostructured vanadium oxide electrodes for enhanced lithium-ion intercalation" *Adv. Funct. Mater.* **16**, 1133 (2006).

[69] A. Pan, J. Zhang, Z. Nie, G. Cao, B. W. Arey, G. Li, S. Liang, and J. Liu, "Facile synthesized nanorod structured vanadium pentoxide for high-rate lithium batteries" *J. Mater. Chem.* **20**, 9193 (2010).

[70] M. E. Spahr, B. P. Stoschitzki, R. Nesper, O. Haas, and P. Novák, "Vanadium oxide nanotubes. A new nanostructured redox‐active material for the electrochemical insertion of lithium" *J. Electrochem. Soc.* **146**, 2780 (1999).

[71] D. R. Rolison, and B. Dunn, "Electrically conductive oxide aerogels: new materials in

electrochemistry" *J. Mater. Chem.* **11**, 963 (2001).

[72] S. H. Ng, S. Y. Chew, J. Wang, D. Wexler, Y. Tournayre, K. Konstantinov, and H. K. Liu, "Synthesis and electrochemical properties of V_2O_5 nanostructures prepared via a precipitation process for lithium-ion battery cathodes" *J. Power Sources* **174**, 1032 (2007).

[73] K. West, B. Zachau-Christiansen, T. Jacobsen, and S. Skaarup, "Lithium insertion into vanadium pentoxide bronzes" *Solid State Ionics* **76**, 15 (1995).

[74] D. B. Le, S. Passerini, F. Coustier, J. Guo, T. Soderstrom, B. B. Owens, and W. H. Smyrl, "Intercalation of polyvalent cations into V_2O_5 aerogels" *Chem. Mater.* **10**, 682 (1998).

[75] S. Komaba, T. Mikumo, N. Yabuuchi, A. Ogata, H. Yoshida, and Y. Yamada, "Electrochemical insertion of Li and Na ions into nanocrystalline Fe_3O_4 and α-Fe_2O_3 for rechargeable batteries" *J. Electrochem. Soc.* **157**, A60 (2010).

[76] D. A. Tompsett, and M. S. Islam, "Electrochemistry of hollandite α-MnO_2: Li-ion and Na-ion insertion and Li_2O incorporation" *Chem. Mater.* **25**, 2515 (2013).

[77] Q. Yuan, S. Ren, J. Zukowski, M. Pomeroy, and V. Soghomonian, "Comparative ion insertion study into a nanostructured vanadium oxide in aqueous salt solutions" *Appl. Phys. Lett.* **105**, 013904 (2014).

[78] R. P. Johnson, "A Note on the Hole Theory of Diffusion" *Phys. Rev.* **56**, 814 (1939).

[79] H. Liu, H. Zhou, L. Chen, Z. Tang, and W. Yang, "Electrochemical insertion/deinsertion of sodium on NaV_6O_{15} nanorods as cathode material of rechargeable sodium-based batteries" *J. Power Sources* **196**, 814 (2011).

[80] M. E. Davis, "Ordered porous materials for emerging applications" *Nature* **417**, 813 (2002).

[81] Y. Zhang, H. Feng, X. Wu, L. Wang, A. Zhang, T. Xia, H. Dong, X. Li, and L. Zhang, "Progress of electrochemical capacitor electrode materials: A review" *Int. J. Hydrogen Energy* **34**, 4889 (2009).

[82] M. S. Whittingham, "Materials challenges facing electrical energy storage" *MRS Bull.* **33**, 411 (2008).

[83] P. J. Hall, M. Mirzaeian, S. I. Fletcher, F. B. Sillars, A. J. Rennie, G. O. Shitta-Bey, G. Wilson, A. Cruden, and R. Carter, "Energy storage in electrochemical capacitors: designing functional materials to improve performance" *Energy Environ. Sci.* **3**, 1238 (2010).

[84] G. Wang, L. Zhang, and J. Zhang, "A review of electrode materials for electrochemical supercapacitors" *Chem. Soc. Rev.* **41**, 797 (2012).

[85] Y. Ma, W. Tong, H. Zhou, and S. L. Suib, "A review of zeolite-like porous materials" *Microporous Mesoporous Mater.* **37**, 243 (2000).

[86] W. M. Meier, "Zeolites and zeolite-like materials" *Pure Appl. Chem.* **58**, 1323 (1986).

[87] R. C. Haushalter, and L. A. Mundi, "Reduced molybdenum phosphates: octahedral-tetrahedral framework solids with tunnels, cages, and micropores" *Chem. Mater.* **4**, 31 (1992).

[88] G. Maurin, P. Senet, S. Devautour, J. C. Giuntini, and F. Henn, "New trends in intercalation

compounds for energy storage" *Kluwer Academic Publishers*, 421-427 (2002).

[89] D. N. Stamires, "Effect of adsorbed phases on the electrical conductivity of synthetic crystalline zeolites" *J. Chem. Phys.* **36**, 3174 (1962).

[90] D. C. Freeman Jr, and D. N. Stamires, "Electrical conductivity of synthetic crystalline zeolites" *J. Chem. Phys.* **35**, 799 (1961).

[91] U. Simon, and M. Franke, "Electrical properties of nanoscaled host/guest compounds" *Microporous Mesoporous Mater.* **41**, 1 (2000).

[92] Q. Yuan, Y. Zhang, S. Green, E. Gihana, and V. Soghomonian, "Ionic and electronic properties of oxo-vanadium arsenate and phosphate frameworks" *Inorg. Chim. Acta* **389**, 202 (2012).

[93] V. Soghomonian, C. Slebodnick, and E. C. Spencer, "Re-determination of the structure of an anionic oxo-vanadium arsenate framework" *Dalton Trans.* **39**, 8652 (2010).

[94] M. I. Khan, L. M. Meyer, R. C. Haushalter, A. L. Schweitzer, J. Zubieta, and J. L. Dye, "Giant Voids in the Hydrothermally Synthesized Microporous Square Pyramidal-Tetrahedral Framework Vanadium Phosphates $[HN(CH_2CH_2)_3NH]K_{1.35}[V_5O_9(PO_4)_2]\times xH_2O$ and $Cs_3[V_5O_9(PO_4)_2]\times xH_2O$" *Chem. Mater.* **8**, 43 (1996).

[95] D. D. Macdonald, "Reflections on the history of electrochemical impedance spectroscopy" *Electrochim. Acta* **51**, 1376 (2006).

[96] S. M. Park, and J. S. Yoo, "Peer reviewed: electrochemical impedance spectroscopy for

better electrochemical measurements" *Anal. Chem.* **75**, 455 A (2003).

[97] S. Elliott, "The Physics and Chemistry of Solids" *John Wiley & Sons, Chichester*, (1998).

[98] H. Bottger, and V. V. Bryksin, "Hopping Conduction in Solids" *VCH Publishers, Florida* (1985).

[99] J. M. Ziman, "Models of Disorder, the Theoretical Physics of Homogeneously Disordered Systems" *Cambridge University Press, Cambridge*, (1982).

[100] S. M. Sze, "Physics of Semiconductor Devices" *Wiley-Interscience, New York*, (1981).

[101] D. W. Breck, "Zeolite Molecular Sieves, Structure, Chemistry and Use" *Wiley-Interscience, New York*, (1974).

[102] I. M. Kalogeras, and A. B. Vassilikou-Dova, "Electrical properties of zeolitic catalysts" *Defect and Diffusion Forum* **164**, 1 (1998).

[103] S. Chandra, "Superionic Solids, Principles and Applications" *North-Holland Publishing Company, Amsterdam*, (1981).

[104] W. J. Pardee, and G. D. Mahan, "Disorder and ionic polarons in solid electrolytes" *J. Solid State Chem.* **15**, 310 (1975).

[105] O. Schäf, H. Ghobarkar, F. Adolf, and P. Knauth, "Influence of ions and molecules on single crystal zeolite conductivity under in situ conditions" *Solid State Ionics* **143**, 433 (2001).

[106] G. Kelemen, and G. Schön, "Ionic conductivity in dehydrated zeolites" *J. Mat. Sci.* **27**, 6036

(1992).

[107] J. Giuntini, G. Maurin, S. Devautour, F. Henn, and J. Zanchetta, "Experimental evidence of polarization effects on exchangeable cations trapped in zeolites" *J. Chem. Phys.* **113**, 4498 (2000).

[108] A. Haouzi, M. Kharroubi, H. Belarbi, S. Devautour-Vinot, F. Henn, and J. Giuntini, "Activation energy for DC conductivity in dehydrated alkali metal-exchanged montmorillonites: experimental results and model" *Appl. Clay Sci.* **27**, 67 (2004).

[109] G. M. Christie, and F. P. F. Van Berkel, "Microstructure-ionic conductivity relationships in ceria-gadolinia electrolytes" *Solid State Ionics* **83**, 17 (1996).

[110] P. A. Cox, "Transition metal oxides: an introduction to their electronic structure and properties" *Oxford University Press*, (2010).

[111] C. N. R. Rao, and B. Raveau, "Transition metal oxides" *World Scientific*, (1995).

[112] A. Munoz-Paez, "Transition Metal Oxides: Geometric and Electronic Structures: Introducing Solid State Topics in Inorganic Chemistry Courses" *J. Chem. Educ.* **71**, 381 (1994).

[113] X. Lang, A. Hirata, T. Fujita, and M. Chen, "Nanoporous metal/oxide hybrid electrodes for electrochemical supercapacitors" *Nat. Nanotechnol.* **6**, 232 (2011).

[114] P.-C. Chen, G. Shen, Y. Shi, H. Chen, and C. Zhou, "Preparation and characterization of flexible asymmetric supercapacitors based on transition-metal-oxide nanowire/single-walled carbon nanotube hybrid thin-film electrodes" *ACS nano* **4**, 4403

(2010).

[115] T. Cottineau, M. Toupin, T. Delahaye, T. Brousse, and D. Belanger, "Nanostructured transition metal oxides for aqueous hybrid electrochemical supercapacitors" *Appl. Phys. A* **82**, 599 (2006).

[116] T. Ohzuku, and A. Ueda, "Why transition metal (di) oxides are the most attractive materials for batteries" *Solid State Ionics* **69**, 201 (1994).

[117] M. Aydinol, A. Kohan, and G. Ceder, "Ab initio calculation of the intercalation voltage of lithium-transition-metal oxide electrodes for rechargeable batteries" *J. Power Sources* **68**, 664 (1997).

[118] F. Zhang, P. Zavalij, and M. S. Whittingham, "Synthesis and Characterization of Manganese Vanadium Oxides as Cathodes in Lithium Batteries" *MRS Proceedings* **581**, 497 (1999).

[119] D. M. D'Alessandro, and F. R. Keene, "Current trends and future challenges in the experimental, theoretical and computational analysis of intervalence charge transfer (IVCT) transitions" *Chem. Soc. Rev.* **35**, 424 (2006).

[120] K. Ragavendran, D. Vasudevan, A. Veluchamy, and B. Emmanuel, "Computation of madelung energies for ionic crystals of variable stoichiometries and mixed valencies and their application in lithium-ion battery voltage modeling" *J. Phys. Chem. B* **108**, 16899 (2004).

[121] N. Henry, L. Burylo-Dhuime, F. Abraham, and O. Mentre, "$Pb_3Mn_5V_2O_{16}$: a new lead

manganese vanadate with double MnII/MnIV valence" *Solid State Sci.* **4**, 1023 (2002).

[122] J. Rodriguez-Carvajal, G. Rousse, C. Masquelier, and M. Hervieu, "Electronic crystallization in a lithium battery material: columnar ordering of electrons and holes in the spinel $LiMn_2O_4$" *Phys. Rev. Lett.* **81**, 4660 (1998).

[123] R. Freitag, and J. Conradie, "Understanding the Jahn–Teller Effect in Octahedral Transition-Metal Complexes: A Molecular Orbital View of the Mn (β-diketonato) 3 Complex" *J. Chem. Educ.* **90**, 1692 (2013).

[124] I. D. Brown, "Recent developments in the methods and applications of the bond valence model" *Chem. Rev.* **109**, 6858 (2009).

[125] K. D. Kreuer, "Proton conductivity: materials and applications" *Chem. Mater.* **8**, 610 (1996).

[126] F. Lichtenberg, A. Herrnberger, K. Wiedenmann, and J. Mannhart, "Synthesis of perovskite-related layered $A_nB_nO_{3n+2}$=ABO_X type niobates and titanates and study of their structural, electric and magnetic properties" *Prog. Solid State Chem.* **29**, 1 (2001).

[127] M. Hanias, A. Anagnostopoulos, K. Kambas, and J. Spyridelis, "Electrical and optical properties of as-grown $TlInS_2$, $TlGaSe_2$ and $TlGaS_2$ single crystals" *Mater. Res. Bull.* **27**, 25 (1992).

[128] H. Peng, C. Xie, D. T. Schoen, and Y. Cui, "Large anisotropy of electrical properties in layer-structured In_2Se_3 nanowires" *Nano Lett.* **8**, 1511 (2008).

[129] X. Wang, T. Wu, G. Wu, H. Chen, Y. Xie, J. Ying, Y. Yan, R. Liu, and X. Chen, "Anisotropy

in the electrical resistivity and susceptibility of superconducting $BaFe_2As_2$ single crystals" *Phys. Rev. Lett.* **102**, 117005 (2009).

[130] N. Mott, "Conduction in glasses containing transition metal ions" *J. Non-Cryst. Solids* **1**, 1 (1968).

[131] N. F. Mott, and E. A. Davis, "Electronic processes in non-crystalline materials" *Oxford University Press*, (2012).

[132] N. F. Mott, "Conduction in non-crystalline materials: III. Localized states in a pseudogap and near extremities of conduction and valence bands" *Philos. Mag.* **19**, 835 (1969).

[133] A. Ghosh, S. Bhattacharya, D. Bhattacharya, and A. Ghosh, "Hopping conduction in zinc vanadate semiconducting glasses" *J. Appl. Phys.* **103**, 083703 (2008).

[134] W. Croft, and M. Kestigian, "The crystallography of Na_3FeF_6" *Mater. Res. Bull.* **3**, 571 (1968).

[135] J. Reau, K. Aliouane, M. Hamadène, A. Guehria, M. El Omari, J. Grannec, and J. Ravez, "Phase transitions and ionic transport in K_3InF_6" *Solid State Ionics* **127**, 301 (2000).

[136] E. Steward, and H. Rooksby, "Transitions in crystal structure of cryolite and related fluorides" *Acta Crystallogr.* **6**, 49 (1953).

[137] J. H. Burns, A. C. Tennissen, and G. D. Brunton, "The crystal structure of a-Li_3AlF_6" *Acta Crystallogr., Sect. B: Struct. Sci* **24**, 225 (1968).

[138] K. Moriya, T. Matsuo, H. Suga, and S. Seki, "On the phase transition of ammonium hexafluoroferrate (III)" *Bull. Chem. Soc. Jpn.* **50**, 1920 (1977).

[139] K. Moriya, T. Matsuo, H. Suga, and S. Seki, "On the phase transitions in ammonium hexafluoroaluminate (III)" *Bull. Chem. Soc. Jpn.* **52**, 3152 (1979).

[140] A. Wolberg, "Crystal structure of $Cs_2LiCo(CN)_6$" *Acta Crystallogr., Sect. B: Struct. Sci* **25**, 161 (1969).

[141] I. D. Brown, "The crystal structure of K_2TeBr_6" *Can. J. Chem.* **42**, 2758 (1964).

[142] I. Flerov, M. Gorev, K. Aleksandrov, A. Tressaud, J. Grannec, and M. Couzi, "Phase transitions in elpasolites (ordered perovskites)" *Mater. Sci. Eng., R* **24**, 81 (1998).

[143] I. N. Flerov, M. V. Gorev, J. Grannec, and A. Tressaud, "Role of metal fluoride octahedra in the mechanism of phase transitions in A_2BMF_6 elpasolites" *J. Fluorine Chem.* **116**, 9 (2002).

[144] M. Ahrens, K. Schuschke, S. Redmer, and E. Kemnitz, "Transparent ceramics from sol–gel derived elpasolites by cold pressing" *Solid State Sci.* **9**, 833 (2007).

[145] D. Dolejš, and D. R. Baker, "Phase transitions and volumetric properties of cryolite, Na_3AlF_6: Differential thermal analysis to 100 MPa" *Am. Mineral.* **91**, 97 (2006).

[146] L. He, H. Yuan, K. Huang, C. Yan, G. Li, Q. He, Y. Yu, and S. Feng, "Hydrothermal syntheses, structures, and magnetic properties of $(NH_4)_2NaVF_6$ and Na_3VF_6" *J. Solid State Chem.* **182**, 2208 (2009).

[147] L. He, D. Zhang, S.-h. Feng, G. Chen, and B. Zou, "Hydrothermal synthesis, structure characterization and magnetic studies of perovskite-type fluorides K_2NaVF_6 and $(NH_4)_3VF_6$" *Chem. Res. Chin. Univ.* **28**, 371 (2012).

[148] S. Jahn, J. Ollivier, and F. Demmel, "Fast ionic mobility in cryolite studied by quasielastic neutron scattering" *Solid State Ionics* **179**, 1957 (2008).

[149] L. Foy, and P. A. Madden, "Ionic motion in crystalline cryolite" *J. Phys. Chem. B.* **110**, 15302 (2006).

[150] P. Poizot, S. Laruelle, S. Grugeon, L. Dupont, and J. Tarascon, "Nano-sized transition-metal oxides as negative-electrode materials for lithium-ion batteries" *Nature* **407**, 496 (2000).

[151] L. Passerini, and R. Pirani, "Struttura dei sali complessi contenenti atomi o gruppi coordinati di specie diversa.- II. Complessi a numero di coordinazione 6.I sali. $(NH_4)_3(VF_6)$, $Tl_2(VF_5(H_2O))$" *Gazz. Chim. Ital.* **62**, 282 (1932).

[152] D. R. Lide, and H. P. R. Frederikse, "CRC handbook of chemistry and physics, student edition" (77^{th} ed.) *CRC Press*, 4-39 (1996).

[153] S. Schwarzmann, "Ueber die kristallstruktur von ammonium gallium hexafluorid" *Z. Kristallogr.* **120**, 286 (1964).

[154] T. Hahn, "International tables for crystallography, volume A: space-group symmetry" (Fifth ed.) *Springer*, 688-691 (2005).

[155] T. Krahl, M. Ahrens, G. Scholz, D. Heidemann, and E. Kemnitz, "Structure of $(NH_4)_3GaF_6$ investigated by multinuclear magic-angle spinning NMR spectroscopy in comparison with Rietveld refinement" *Inorg. Chem.* **47**, 663 (2008).

[156] A. A. Udovenko, N. M. Laptash, and I. G. Maslennikova, "Orientation disorder in

ammonium elpasolites: Crystal structures of $(NH_4)_3AlF_6$, $(NH_4)_3TiOF_5$ and $(NH_4)_3FeF_6$" *J. Fluorine Chem.* **124**, 5 (2003).

[157] A. Meden, J. Siftar, and L. Golic, "Hydrazinium (1^+) hexafluorogallate (III) and hydrazinium (2^+) aquapentafluorogallate (III)" *Acta Crystallogr., Sect. C: Cryst. Struct. Commun.* **52**, 493 (1996).

[158] E. Alter, and R. Hoppe, "Über Hexafluorovanadate(III). Cs_2MVF_6 und Rb_2MVF_6 (M=Tl, K und Na); mit einer Bemerkung über Na_3VF_6" *Z. Anorg. Allg. Chem.* **412**, 110 (1975).

[159] A. A. Hampshire, "A colorful oxidation reduction demonstration" *Proc. S. D. Acad. Sci.* **43**, 116 (1964).

[160] S. Orecchio, V. Romano, and R. Zingales, "Redox potentials of vanadium-containing couples. Part 2. The determination of the formal vanadium(IV)/vanadium(III) potential at 25 °C in aqueous 1 M chloride solution" *J. Chem. Res.*, 335 (1989).

[161] M. Fiore, S. Orecchio, V. Romano, and R. Zingales, "Redox potentials of vanadium-containing couples. Part 3. The formal redox potential of the V^{3+}–V^{2+} couple" *J. Chem. Soc., Dalton Trans.*, 799 (1993).

[162] S. Orecchio, V. Romano, and R. Zingales, "Redox potentials of vanadium-containing couples. Part 1. An electrolytic, optical, potentiometric method for the determination of the formal vanadium(V)/vanadium(IV) potential in aqueous sodium-chloride" *J. Chem. Res.*, 14 (1989).

[163] J. Fleig, and J. Maier, "Microcontact impedance measurements of individual highly

conductive grain boundaries: general aspects and application to AgCl" *Phys. Chem. Chem. Phys.* **1**, 3315 (1999).

[164] J. T. Irvine, D. C. Sinclair, and A. R. West, "Electroceramics: characterization by impedance spectroscopy" *Adv. Mater.* **2**, 132 (1990).

[165] F. B. Ravari, and A. Dadgareenezhad, "Synergistic influence of propargyl alcohol and zinc sulfate on inhibition of corrosion of aluminum in 0.5 M H_2SO_4" *J. Chil. Chem. Soc.* **58**, 1853 (2013).